DESIGN PRINCIPLES OF STRETCHABLE AND COMPLIANT ELECTROMECHANICAL DEVICES FOR BIOMEDICAL APPLICATIONS

by

Min Ku Kim

A Dissertation

Submitted to the Faculty of Purdue University

In Partial Fulfillment of the Requirements for the degree of

Doctor of Philosophy

Weldon School of Biomedical Engineering

West Lafayette, Indiana

May 2021

THE PURDUE UNIVERSITY GRADUATE SCHOOL
STATEMENT OF COMMITTEE APPROVAL

Dr. Chi Hwan Lee, Chair

Weldon School of Biomedical Engineering

Dr. Hyowon Lee

Weldon School of Biomedical Engineering

Dr. Krishna Jayant

Weldon School of Biomedical Engineering

Dr. Wenzhuo Wu

School of Industrial Engineering

Approved by:

Dr. Andrew O. Brightman

Dedicated to my parents for the invaluable gift of education and to my sister.

ACKNOWLEDGMENTS

First and foremost, I express my sincere gratitude to Prof. Chi Hwan Lee for the great opportunity to be a part of this great vision. His guidance and mentorship have been important in my growth as a scientist, an academic and as a person. I also would like to thank the committee members, Prof. Hyowon Lee, Prof. Krishna Jayant, and Prof. Wenzhuo Wu for their incredible support.

I would also like to thank all the graduate students and postdocs from Prof. Chi Hwan Lee's group whom I had the chance to meet, worked with and received help which was critical in my professional development. I would like to thank Mr. Asem Aboelzahab for his mentorship and patience, especially his guidance and support during my teaching assistant positions.

I would also like to thank all of my external collaborators on various projects. Prof. Byung-Cheol Min and Dr. Ramviyas Nattanmai Parasuraman at Purdue Polytechnique University and Prof. Nanshu Lu and Mr. Liu Wang at University of Texas at Austin for our work on the prosthetic electronic glove. Prof. Dong Rip Kim and Dr. Hanmin Jang at Hanyang University for our work on the ultrabouyant cell monitoring scaffold. Prof. Muhammad A. Alam, Prof. Shreyas Sen, and Dr. Ratul Kumar Baruah along with many clinicians in the Department of Speech, Language, and Hearing Sciences at Purdue University for our work on the submental sensor patch. Prof. Hyunjoon Kong and Dr. Byung Soo Kim at the University of Illinois at Urbana-Champaign for our work on soft hydrogel manipulator.

I would also like to thank the BME department staffs, Sandy May, Tammy Siemers, Carla Brady, Pamela Lamb, Linda Doyle, and Benjamin Overly for their hard work and effort.

Finally, I want to thank my parents and my sister whom I would not be here without you.

TABLE OF CONTENTS

LIST OF TABLES

LIST OF FIGURES

ABSTRACT

The development of wearable devices to monitor biosignals and collect real-time data from biological systems at all scales from cellular to organ level has played a significant role in the field of medical engineering. The current coronavirus disease 2019 (COVID-19) pandemic has further increased the demand for remote monitoring and smart healthcare where patient data can be also be accessed from a remote distance. Recent efforts to integrate wearable devices with artificial intelligence and machine learning have transformed conventional healthcare into smart healthcare, which requires reliable and robust recording data. The biomedical devices that are mechanically stretchable and compliant have provided the capability to form a seamless interface with the curvilinear, soft surface of tissues and body, enabling accurate, continuous acquisition of physical and electrophysiological signals. This dissertation presents a comprehensive set of functional materials, design principles, and fabrication strategies to develop mechanically stretchable and compliant biomedical devices tailored for various applications, including (1) a stretchable sensor patch enabling the continuous monitoring of swallowing function from the submental/facial area for the telerehabilitation of patients with dysphagia, (2) a human hand-like sensory glove for advanced control of prosthetic hands, (3) a mechanically compliant manipulator for the non-invasive handling of delicate biomaterials and bioelectronics, and (4) a stretchable sensors embedded inside a tissue scaffold enabling the continuous monitoring of cellular electrophysiological behavior with high spatiotemporal resolution.

1. INTRODUCTION

Wearable devices are the gateway to obtaining information within the body. However, widespread commercially available wearables devices are still based on rigid formfactor with limited, non-specific sensing modalities (breath rate, heart rate, galvanic skin response, etc.) while many of the state-of-the-art wearable devices are not yet fully developed for everyday use due to long-term reliability and usability issues. General public's desire for health awareness is continually increasing. In addition, growing aging population and increased prevalence of chronic diseases is placing a strain on the healthcare systems. As a result, there is an increased the demand for the development of biomedical systems and personal healthcare devices which allows noninvasive diagnosis and monitoring of health and provide point-of-care services outside the clinic[1-4]. Modern healthcare systems have recognized the benefit of data driven decision making and data analysis by adopting smart technologies like big data, machine learning and artificial intelligence (AI). With the new wave of technology in medicine, which has been expedited by recent surge of Internet of things (IoT), smartphone, and COVID-19 pandemic outbreak, the traditional medicine and healthcare researches are under transformation. However, the adoption of smart machine learning and AI system are built on copious amount of reliable and high-quality data which are collected by the sensors.

Recently, flexible and stretchable electronics have received increasing attention from academic and scientific communities due to their potential for new class of applications in wearable applications which is also evidenced by the increased number of publications in the field[5]. Wearable biomedical devices typically contain multitude of sensors, actuators, data acquisition systems, powering and data communication that allows for accurate measurement of physical, electrophysiological, and biosignal from the human body[6]. However, there still is a gap on sensing modalities to measure more specific events such as identifying a dangerous seizure event from physical exercise, or track eating events to form a food intake timeline for diabetic patients. Wearable systems still hold much benefit due to its noninvasive location, which is conveniently mounted on the body to gather information. The biggest obstacle for the sensors to overcome is also the skin, which act as a barrier for information that are generated within the body. Mechanical mismatch between the skin and the device is one of the main challenges which can lead to

degradation in sensor performance. Recent advances in soft functional materials and fabrication techniques enabled the development of mechanically deformable and stretchable devices that can be directly mounted onto the epidermis in an imperceptive manner that does not hinder the motion of the wearer[7,8]. The excellent deformability and conformability is what allows the devices to seamlessly integrate with the skin, and even the soft cell sheets which is fundamental in achieving accurate, reliable and high-fidelity data acquisition of biological signals in many biomedical applications[9].

Overall theme of this dissertation is to propose materials, fabrication methods, and design strategies to fabricate devices to facilitate and improve collection of high-quality data in healthcare and biomedical application by improving device reliability, ease of use and manufacturability. This can be achieved through understanding and studying the electrical and mechanical interaction between the device and biological system from human size physiology and down to the cellular level. Chapter 2 will look into the design strategies to utilize rapid prototyping methods to design and fabricate a sensor patch that can conform to physically challenging curvilinear surfaces of the body such as the submental area and how it can be used to reliably acquire electrophysiological signals for the telerehabilitation of swallow disorder. Chapter 3 will deal with designs and strategies to effectively integrate an array of multimodal sensors on a physically demanding and dynamic area such as the glove by combining transfer-printing and screen-printing method. Chapter 4 will deal with thermally controlled, mechanically compliant hydrogel which is capable of non-invasively handle delicate materials like cell sheets and thin film bioelectronic devices from and to spatially challenging areas of the body/organ in wet or dry conditions. Chapter 5 will deal with design strategies for a 3D scaffold cellular sensor with an ultra-buoyant sponge like PDMS structure to isolate the electronic sensors away from the cell media to ensure long-term stable data recording of cellular behavior.

2. SKIN PATCH SENSOR FOR THE NECK AND FACE AREA

2.1 Introduction

Successful realization of a complete swallow requires the accurate coordination of more than forty pairs of muscles within the head and neck area, six pairs of cranial nerves, multitude of circuitry in the brain stem, and several cranial areas[10-12]. Any interruption in such signal pathways can result in oropharyngeal swallowing disorders (also known as oropharyngeal dysphagia). It is reported that, each year in the United States, around 9.44 million of adults and 500,000 children experience swallow disorder[13,14]. The cause of swallow disorder can result from a variety of neurological conditions (e.g., Parkinson's disease, dementia, stroke, and cerebral palsy), cancer of the head and neck and its treatment, side effects, and genetic conditions[15,16]. Swallow disorder negatively affects with the daily life. Lack of appropriate treatment can lead to severe consequences such as malnutrition, dehydration, damage of the respiratory track by accidental aspiration of food/liquid, or even death[17,18]. Current rehabilitative treatment for swallow disorder have been demonstrated its effectiveness but requires frequent practices exercises of the head and neck which mainly rely on cumbersome and expensive biofeedback devices (e.g., oral manometers, electromyographic devices, and endoscopy)[19-22]. The treatment exercise requires patients to make multiple clinical visits per day or week for treatment sessions, in most situations not feasible or economically feasible for many elderly patients, especially for those who are physically limited in terms of mobility or situated in rural areas that are often lacking medical professionals and resources. As a result, previous studies have shown that the average adherence for the treatment of swallow disorder were between 22 and 52%[23], which can lead to nonideal treatment results.

A possible solution involves the utilization of portable devices to obtain biofeedback signals which can be used during treatment exercises and swallowing maneuvers. The portable devices would allow real-time data collection and upload the collected data to a cloud storage for the clinician to review and perform additional data processing[24-27]. However, many of the devices currently available are based on a rigid or semiflexible formfactor which are not well suited to be attached to the curvilinear surface of the submental area. The movement of head/neck often results in signal degradation during data acquisition and discomfort to patients. Recent advances in mechanically flexible and stretchable device platform could solve this issue by utilizing ultrathin substrate to further improve conformable contact of devices to the submental area[28,29]. In order to bridge the gap, further improvements are required for the translation of such technology into practice. Factors such as continuous wireless data transmission, signal fidelity and mechanical durability for repeated uses (reducing cost) on a frequent daily or weekly basis, ease-of-use, and the usability across all age groups are all essential.

Such circumstance was consistent with the findings of a recent preliminary assessment of device requirement (table 2.1), where 30 individuals (20 clinicians and 10 patients) were interviewed. It was identified by the clinician and the patients that lack of patient treatment compliance/adherence was the number one obstacle to the rehabilitation of swallow disorder. More importantly, the cause of noncompliance was mainly due to high expense, difficult-to-use devices, limited functionality of the monitoring system, and unable to access treatment. The clinicians/therapist feedback identified signal accuracy and fidelity as the most important factors to address the current challenges. The participants feedback reported ease-of-use as the important criteria. Therefore, there is a high demand to develop and validate an accurate and cost-effective monitoring system for the tele-rehabilitation of swallow disorder that is easy-to-use by any age group.

Table 2.1. Initial needs assessment survey.

	Common Themes	Frequency of specific responses
Rehabilitation Challenges	Poor Patient Compliance/Adherence	Expense of Equipment (50%), Availability of Equipment (30%), "Boring" Exercises (20%)*, Patient Travel (30%)
	Poor Patient Understanding	Lack of Evidence (30%), Complexity of Tools/Exercises (40%), Poor Feedback Quality (20%), Limited Time (20%)
Implications of Challenges	Poor Health Outcomes	Financial Costs (Patients/Clinics) (70%), Readmissions/Bounce Backs (40%)
	Psychological Outcomes	Frustration (Patient/Clinicians) (40%), Depression (20%)*, Social Isolation (20%)
Important Design Considerations	Ease-of-use (100%), Accuracy (80%), Frequency of use (50%), Ease of Attachment to the Body (40%), Quality of Feedback and Reward (40%), Time Efficiency (20%)	

**All respondents of this response were patients.*

To address such need, a mechanically compliant skin sensor patch was developed that is capable of noninvasively interface with the submental area in that can be easily removed for reusability without causing skin irritation. The patch can provide high-fidelity recording of both surface electromyography (sEMG) signals (i.e., muscular activity from submental muscles) and mechanical movement of the laryngeal/thyroid notch (via integrated bending strain sensor) during swallowing. The patch is connected to a custom-built wireless data acquisition circuit to wirelessly transmit the collected data to a nearby device for additional data processing or sent to the clinician to track patient progress. The sensor patch packaging scheme is precisely designed, combined with a honeycomb mesh configuration as the substrate, provides both elasticity and durability required for repeated use as one of the major cost-saving factors. Experimental, computational simulation, and theoretical results reveal the underlying physical characteristics of such design features. Pilot testing on healthy human participants, in addition to demonstration with Parkinson's disease patient with swallow disorder, provide comparable results with those collected using standard clinical swallow study measurement setup.

2.2 Materials and Methods

2.2.1 Fabrication of compliant sensor patch

The entire fabrication process relied on the use of cost-effective rapid prototyping methods, including photolithographic patterning and laser cutting. The fabrication began by mounting the base substrate of a commercial double-sided Cu clad (Pyralux AP7413R, DuPont USA) composed of a 13 mm thick PI on a glass slide. The overall outline of the device configurations was patterned using a laser cutter (PLS6MW, Universal Laser Systems), followed by laminating a negative type dry film photoresist (Riston MM540, DuPont) with a laminator (AL13P, Apache). The prepared Cu film was then processed under a standard photolithographic patterning that involved an ultraviolet (UV) exposure (0.3 mW/cm^2, Model 18, Jelight Company) for 165 seconds (50 mJ/cm^2 in total) and soaking in a solution of sodium carbonate (Na_2CO_3) for ~2 min. The UV-exposed Cu film was chemically etched in a solution of ferric chloride ($FeCl_3$) to form the two channels of differential sEMG electrodes and the interconnector traces on the surface. The remaining photoresist was removed by soaking the entire structure in a solution of sodium hydroxide (NaOH) for ~2min. A precut piece piezoresistive strip (2 mm × 25 mm, sheet resistivity: <30 $k\Omega/cm^2$; Velostat, 3M) was bonded at the predetermined location using a conductive epoxy adhesive (#8331, MG Chemicals), followed by annealing at 70 °C for 30 min in a convection oven. The resulting structure was spin casted with bilayers of silicone elastomers, such as Silbione (HC2 2022, Bluestar Chemical) and Ecoflex (Smooth-On), while the surface of the sEMG recording electrodes was temporarily masked. Curing the elastomers at room temperature overnight, followed by removal of the masking films completed the entire process.

2.2.2 Fabrication of the remote-control unit

The portable unit for remote data transmission and powering consisted of two-layer-stacked printed circuit boards (PCBs) with commercially available circuit components. The first layer contained the analog front end on one side and the microcontroller for digital acquisition on the other side. The second layer contained the Bluetooth module and the antenna. The usability (size and battery life) along with the quality of the acquired sEMG signals were the primary constraints considered while designing the PCB. The battery life of the device was ~16 hours while

transmitting data over the Bluetooth link, which was approximately twice longer than that when using a commercial wireless unit (BioRadioTM). The size of the portable unit was 5.6 cm × 3.8 cm × 1.8 cm, which is almost three times smaller than that of the commercial unit (10 cm × 6 cm × 2 cm). The data acquisition frontend was programmed in terms of sampling rate and resolution to optimize the condition between the acquisition quality and battery life. The assembled unit was packaged in a 3D-printed housing.

2.2.3 Remote data acquisition

The remote data acquisition was performed by exploiting a zero-insertion force connector placed on the board. Both the sEMG signals and strain waveforms were captured during swallowing by a differential input 24-bit resolution analog-to-digital converter (ADS1294, Texas Instrument) at the sampling rates of 1 kHz (sEMG channels) and 100 Hz (strain gauge), respectively. The collected data were then remotely transmitted via a Bluetooth module (HC-06, Guangzhou HC Information Technologies) to an external data acquisition system (commercial smart tablets or phones). The data were then digitally processed with a finite impulse response filter with a fourth-order Butterworth bandpass filter with the cutoff frequency of 20 to 500 Hz and 0.1 to 20Hz for the recordings of sEMG signals and strain waveforms, respectively.

2.2.4 Finite element analysis

The study to understand the underlying mechanics of the honeycomb featured structure under mechanical deformations was conducted by using the Abaqus/standard package. The deformation of the structure was modeled by linear elastic behavior with the mechanical modulus (E) of 2.5 GPa and Poisson's ratio of 0.34. The PI substrate was modeled by four-node shell elements (S4R). The refined meshes were used in the numerical calculation to improve accuracy. Displacement boundary conditions were applied to both edges of the structure to produce uniaxial tension for the strains of 4, 8, and 12%. To determine the maximum strain at different angles of honeycomb mesh, the empirically obtained data associated with the deformation where the first crack occurs were used.

2.2.5 Theoretical analysis of the stress-strain relationship

Since the stress-strain relationship occurred in the 2D plane until the honeycomb lattices were buckled out of the plane, a MATLAB toolbox (Partial Differential Equation Toolbox, version R2018b) was used to accurately describe the position-resolved anisotropic stress in the system. With the application of a force in various loading directions of the honeycomb mesh, the stress-strain relation of a material for isotropic and isothermal conditions can be written as the following

$$\begin{pmatrix} \sigma_x \\ \sigma_y \\ \tau_{xy} \end{pmatrix} = \frac{E}{1-\nu^2} \begin{pmatrix} 1 & \nu & 0 \\ \nu & 1 & 0 \\ 0 & 0 & \frac{1-\nu}{2} \end{pmatrix} \begin{pmatrix} \varepsilon_x \\ \varepsilon_y \\ \gamma_{xy} \end{pmatrix}$$

where σ_x and σ_y are the normal stresses in the x and y are the directions, τ_{xy} is the shear stress, E is the Young's modulus, and ν is the Poisson's ratio. The deformations along the x and y directions are defined as u and v, respectively. These displacements allowed the calculation of the strain, i.e., $\varepsilon_x = \partial u/\partial x$, $\varepsilon_y = \partial v/\partial y$, $\gamma_{xy} = \partial u/\partial y + \partial u/\partial x$. The force ($k$) in the x and y directions satisfies the equations $-\frac{\partial \sigma_x}{\partial x} - \frac{\partial \tau_{xy}}{\partial y} = k_x$, $-\frac{\partial \tau_{xy}}{\partial x} - \frac{\partial \sigma_y}{\partial y} = k_y$. The displacement equations can be represented in a general form as $-\nabla . (c \otimes \nabla u) = k$, where c is a rank 4 tensor, which can be written as four 2 × 2 matrices namely, c_{11}, c_{12}, c_{21}, and c_{22} as

$$c_{11} = \begin{pmatrix} 2G+\mu & 0 \\ 0 & G \end{pmatrix}, c_{12} = \begin{pmatrix} 0 & \mu \\ G & 0 \end{pmatrix}, c_{21} = \begin{pmatrix} 0 & G \\ \mu & 0 \end{pmatrix}, c_{22} = \begin{pmatrix} G & 0 \\ 0 & 2G+\mu \end{pmatrix}$$

where $G = E/2(1 + \nu)$ is the shear modulus and related to μ as $\mu = 2G\nu/(1 - \nu)$. The partial differential equations with the MATLAB toolbox can be solved subject to three types of boundary conditions: (i) Dirichlet—at the edges, the solution u satisfies the equation $hu = r$, which represents a matrix h multiplying the solution vector u, and equaling the vector r. Both h and r can be functions of space (x and y), the solution u, and time. (ii) Neumann boundary conditions on the edge, the solution u satisfies the equation n. $(c \nabla u) + qu = g$, where n, q, and g (g has the same dimension as k) are the outward unit normal, spring constant, and surface traction respectively.

Both q and g can be functions of *x*, *y*, the solution *u*, and, for parabolic and hyperbolic equations, time. Last, (iii) mixed boundary condition involves a combination of Dirichlet and Neumann boundary conditions.

In the FEA simulation, the boundary conditions $h_{11} = 1$, $h_{12} = 0$, and $r = 0$ were used as the Dirichlet boundary conditions to fix a hexagon wall in the x direction, and the $q_{11} = 0$ and $q_{12} = 0$ conditions were used as the Neumann boundary conditions (which allows the hexagonal wall to have displacement locally/globally or both). Appropriate force per unit length to have maximum strain was applied to a hexagonal cell wall in a particular load direction through *g* as Neumann boundary condition.

2.2.6 Theoretical analysis of the maximum strain

The remarkable parametric sensitivity observed by experiment of honeycomb mesh and predicted by the FEA simulation can be explained by a simple analytical theory as well. Considering that the maximum mechanical strain (ε_{max}) is given by

$$\varepsilon_{max} = \frac{\sigma_{max}}{E}$$

where σ_{max} is the maximum stress that can be sustained by the honeycomb lattice before it breaks, and *E* is the effective Young's modulus. To recalculate σ_{max}, the honeycomb structure collapses plastically when the bending moment in a unit hexagonal cell wall reached its plastic moment (characterized by a plateau of the stress strain curve). Therefore, σ_{max} was calculated by[30]

$$\sigma_{plastic} = \sigma_{ys}\left(\frac{w}{l}\right)^2 \frac{1}{2(h/l + sin\theta)sin\theta}$$

where σ_{ys} is the yield strength of the PI material. Similarly, the anisotropic Young's modulus of the hexagonal PI (*E*) was calculated as

$$E = E_{poly}\left(\frac{w}{l}\right)^3 \frac{cos\theta}{(h/l + sin\theta)sin^2\theta}$$

where E_{poly} is the Young's modulus of the PI, and h, l, and w are the height, length, and width of the hexagon wall. To interpret the experimental results, four regular honeycomb lattices (w = 1 mm, $h = l$ = 2, 2.5, 3, and 4.5 mm) loaded in three different directions (q = 0°, 45°, and 90°). The largest section of the honeycomb lattice having the l of 70 mm and the w of 20 mm was simulated to eliminate any edge effect. The force with which a hexagonal wall is pulled normally in the outward direction is F_n. Therefore, when the lattice is pulled in the positive x direction (q = 90°), each right vertical wall of the honeycomb is pulled by a force F_n, and each outside sidewall contributes a force of $F_n \cos(60°)$ (=0.5 F_n), and the total force acting on the honeycomb walls of the lattice (F_x) is the sum of the individual forces on the nonoverlapping hexagon walls residing in the extreme right side of the x direction in a width of 20 mm of the lattice. However, when a force is applied in the vertical direction (q =0°), each hexagon cell has two side walls in the force direction each contributing a force of $F_n \cos(30°)$ in the q = 0° loading direction. Therefore, each hexagon contributes a force of $2F_n \cos(30°)$ (=1.73 F_n) along the q = 0° loading direction. As the length of the lattice is 70 mm, the number of hexagon walls contributing to total force in the q = 0° direction (F_y) is more than q = 90° loading direction (>2 times depending on the hexagon wall length and width dimension). As the total area and the Young's modulus (E, for a fixed value of l) of the PI substrate remain same, with an increased value of applied force, the strain is more for the q = 0° load direction compared with the strain in the q = 90° load direction. As the maximum strain is directly proportional to the maximum force applied to the lattice, loading the lattice in the q = 0° axis has the maximum strain than loading along any other direction. Similarly, the force components along the q = 45° load direction was calculated and the corresponds with the maximum strain as well.

2.2.7 Theoretical analysis of adhesion force

Since the FEA results were captured by the analytical theory, the adhesion was calculated using the analytical theory. Considering the adhesion properties of a honeycomb lattice affixed onto a substrate, the adhesion force between a 10 mm thick layer of Silbione (HC2 2022) and a 13 mm thick PI was calculated by placing the Silbione layer on a 500 mm thick Si wafer and then slowly pulling the PI film in the outward direction. The length and width of PI substrate are 65 mm and 38 mm, respectively. The effective Young's modulus (E_{eff}) of the Si_{wafer} and the Silbione was calculated as[31]

$$E_{eff} = V_1E_1 + V_2E_2 + \frac{V_1V_2E_1E_2(\nu_1 - \nu_2)^2}{V_1E_1(1-\nu_2{}^2) + V_2E_2(1-\nu_1{}^2)}$$

where V_1 and V_2 are the volume fractions, E_1 and E_2 are the Young's moduli, and ν_1 and ν_2 are the Poisson's ratios of the Si wafer and the Silbione, respectively. The adhesion force per width between the Silbione and the PI was computed using the Timoshenko model as[32]

$$F_{adhesion} = \frac{-\varepsilon_m}{1/E_{eff}t_1 + 1/E_{poly}t_2 + \frac{3(t_1+t_2)^2}{E_{eff}t_1{}^3 + E_{poly}t_2{}^3}}$$

where t_1 and t_2 are thicknesses of the Silbione and PI, respectively. $\varepsilon_m = \varepsilon_f - \varepsilon_s$, ε_f and ε_s are the strains induced by lattice mismatch in the Silbione and PI, respectively. ε_m is the mismatch strain defined as $\varepsilon_m = (a_s - a_f)/a_f$, where a_f and as are the lattice parameters of the Silbione and PI, respectively. The following material constants were used in the computation: E_{Si} = 179 GPa (Si <100>, single crystal, undoped), $E_{Silbione}$ = 5 kPa (HC2 2022, Bluestar Chemical), E_{PI} = 4.826 GPa (Pyralux AP7413R, DuPont USA), ν_{Si} = 0.265, and $\nu_{Silbione}$ = 0.48. The adhesion force was calculated for PI having a hexagon cell wall length (l) of 4.5 mm and a width (w) of 1 to 6 mm. The theoretical predictions provided a good agreement with the experimental results.

2.2.8 Computational analysis of adhesion force

For the computational modeling of adhesion force, the sensor patch was contacted to the skin with a clinically accepted adhesive material (~10 mm thick, E = ~5 kPa; Silbione HC2 2022, Bluestar Chemical). The parameters for the thickness, E, and Poisson ratio of the skin are 0.2 mm, 10 MPa, and 0.49, respectively. The lattice mismatch constant (ε_m) at the interface was obtained from a previous experimental study for adhesion force between the skin and Silbione[33]. For the 3D FEM analysis (using the commercial software COMSOL), a series of open honeycomb lattices with l = 4.5 mm and w = 1-6 mm were considered. For each unit cell, a peeling force was applied at the edge of the honeycomb lattice while the maximum strain developed at the interface was recorded. The corresponding stress-strain curve was obtained to determine the stress at which the

maximum strain reached a critical value. The results showed that the sensor patch adhered well to the skin in which the adhesion strength increases with *w*. The asymptotic limit of the adhesion force (F_{adhesion}) between the sensor patch and the skin for the bulk structure (without the honeycomb networks) was obtained when the honeycomb meshes were closed at $w \rightarrow \sqrt{3} \cdot l$, and its value is approximately 0.27 N/cm. These results were comparable to those obtained on the basis of the recent analytical expression for the *E* of honeycomb networks as[34]

$$E = E_{poly}\left(\frac{w}{l}\right)^3 \frac{sin\theta}{\frac{h}{l}(1+cos\theta)(sin^2\theta\left(\frac{w}{l}\right)^2 + cos^2\theta}$$

2.2.9 VFSS recording

The VFSS images were acquired using a videofluoroscopic C-arm system (OEC 9800 Plus Digital Mobile 12" GE) at the full resolution (30 pulses/s) and recorded at 30 frames/s on an MDRdigital video recorder (PACSgear). The patient was seated in an upright position in lateral view to allow visualization of the lips, oral and nasal cavities, cervical vertebrae, and the upper esophagus. The following swallowing trials were performed (two times each): 5 ml of Varibar thin liquid barium (catalog no. 105, E-ZEM Canada Inc.), 10 ml of Varibar thin liquid, and 5 cc of Varibar barium pudding (catalog no.125, E-Z-EM Canada Inc.). In addition, the patient was asked to perform additional swallows of 5 ml of Varibar thin liquid barium or 5 cc of Varibar barium pudding using the following commonly prescribed swallowing maneuvers/exercises that are often trained with the use of sEMG: effortful swallow (or “swallow hard”) and Mendelsohn maneuver (or “swallow longer”). Barium was used as the contrast agent because of its visibility in videofluoroscopy.

2.2.10 Analysis of sEMG signals and strain waveforms

The sEMG recordings were analyzed using a custom-built MATLAB code (MATLAB Inc., Natick, MA). The sEMG signals were calibrated, and the raw signals were demeaned, rectified, and smoothed. The measurements obtained from each trial were (i) amplitude (area under the curve) and (ii) burst duration of the smoothed sEMG signals for the left and right channels. After

preprocessing, the onsets and offsets of each trial were selected to calculate the sEMG amplitude and burst duration. Identification of swallow events was semiautomatic. The analyzer identified the trial of interest and the relative onset and offset of the swallow. Within the user-selected window, an algorithm was applied to determine the onset and offset of EMG activity (defined as a change in sEMG amplitude that was >2 SDs of the pretrial sEMG baseline activity) and within 0.5 s of the user-defined window. In addition, because sEMG amplitudes vary between tasks and subjects (e.g., as a function of electrode impedance), sEMG amplitude in microvolts was normalized relative to the amplitude recorded during the maximal voluntary contraction. Specifically, the patient who participated in this pilot study produced three trials of maximum lingual press using the Iowa Oral Performance Instrument, and the task-related sEMG amplitudes were expressed as percentages of the mean amplitude of this criterion gesture.

2.3 Results

2.3.1 Compliant skin sensor patch system with remote monitoring controls

Figure 2.1a shows a schematic illustration (left) and a photograph (right) of the system. Here, the sensor patch is mounted to the submental area so that the embedded sEMG electrodes remain in contact with the skin aligned parallel to underlying muscular fibers. The measurement of submental sEMG signals occurs by exploiting double-differential recording using two pairs of recording electrodes (Fig. 2.1b) with relatively small diameter (5 mm) and interelectrode distance (12 mm) to reduce detection volume and consequently minimize the effect of cross-talk[35]. In addition, the sensor patch incorporates a bending sensor (Fig. 2.1c) to provide piezoresistive responses against relative laryngeal movement during swallowing. The sensor patch is connected to a custom-built, portable unit (56 mm × 37 mm × 20 mm, ~55 g) clipped on the wearer's clothing via a flexible anisotropic conductive film wire, allowing for remote data transmission and powering. Figure 2d shows the unpackaged integrated circuit chip of this portable unit that consists of a Bluetooth module (38 mm × 17 mm × 4 mm; HC-06, Guangzhou HC Information Technologies Co. Ltd., China) for remote data transmission, a four-channel 24-bit analog-to-digital converter (12 mm × 12 mm × 1 mm; ADS1294, Texas Instruments, USA), a rechargeable battery (50 mm × 34 mm × 6 mm, 1000 mAh; PRT-13813, SparkFun Electronics, USA) for on-board

power supply, and a three-dimensional (3D)–printed plastic case made of acrylonitrile butadiene styrene for housing.

Comprehensive characterizations for the key components of this sensor patch system indicate the following: (i) the sensor patch provides slightly lower electrode-skin contact impedances than those of commercial recording electrodes (40 mm × 34 mm × 3 mm, Ag/AgCl electrode; Red Dot, 3M), mainly due to the soft, conformal contact along the curvature of the submental area (Fig. 2.1e); (ii) the strain gauge responds to bending radii of 0.5 to 4 cm (Fig. 2.1f), and thus remains sensitive to laryngeal/thyroid notch movement during swallowing; (iii) the portable unit allows remote data acquisition across multiple channels at programmable resolution (up to 24 bits) and sampling rate (up to 32 ksps) where the front-end circuit gain is controllable to vary the resolution of the input signal (Fig. 2.1g).

The fabrication of the sensor patch begins with a thin (13 μm), sheet of polyimide (PI) laminated with a Cu film (9 μm) on both sides. A laser cutting system (PLS6MW, Universal Laser Systems) was used to pattern the open honeycomb networks and outline of the device. A subsequent photolithographic patterning, followed by wet etching with a Cu etchant (CE-100, Transene), defines the recording electrodes and interconnectors for two pairs of sEMG channels and a strain gauge on each side of the PI sheet. A piezoresistive strip (Velostat, 3M, Gauge Factor ≈ 2.61[36]) is then transfer printed with a conductive adhesive epoxy (#8331, MG Chemicals) to serve as the strain sensing element. The next step involves encapsulating the entire structure with soft elastomers in a core/shell layout that includes (i) an ultralow-modulus elastomer core [Silbione HC2 2022, Bluestar Chemical, ~10 μm thick, Young's modulus (E) = ~5 kPa] to provide physical isolation from the surroundings and (ii) a thin enclosure shell composed of a different elastomer with a modified formulation (Ecoflex, Smooth-On, ~5 μm thick, E = 60 kPa) to provide a mechanically robust, tough interface for handling and lamination. Here, the overall quality of the core/shell layout is determined by controlling the thickness, mechanical modulus, and surface textures of each elastomer layer[37]. The surface of the recording electrodes remains exposed after the encapsulation where a thin Au film (~500 nm) is electroplated to promote the biocompatibility[38]. Details of the fabrication process appear in Materials and Methods. These characteristics of the soft core/shell layout allow the sensor patch to remain gently contacted to the

submental skin for a range of age groups—between the ages of 26, 35, 45, and 64 years—who have different physical properties of the skin (Fig. 2.2)[39,40]. The contact quality on the submental skin at different age groups—the subject ages of 26 and 79 years—undergoes negligible changes even with head/neck motions and position adjustments of the wearer, and with repetitive placement and removal of the sensor patch, without generating any skin irritation (fig. 2.3a). The recorded sEMG data during swallowing from these multiple trials (subject age: 26) appear in fig. 2.3b.

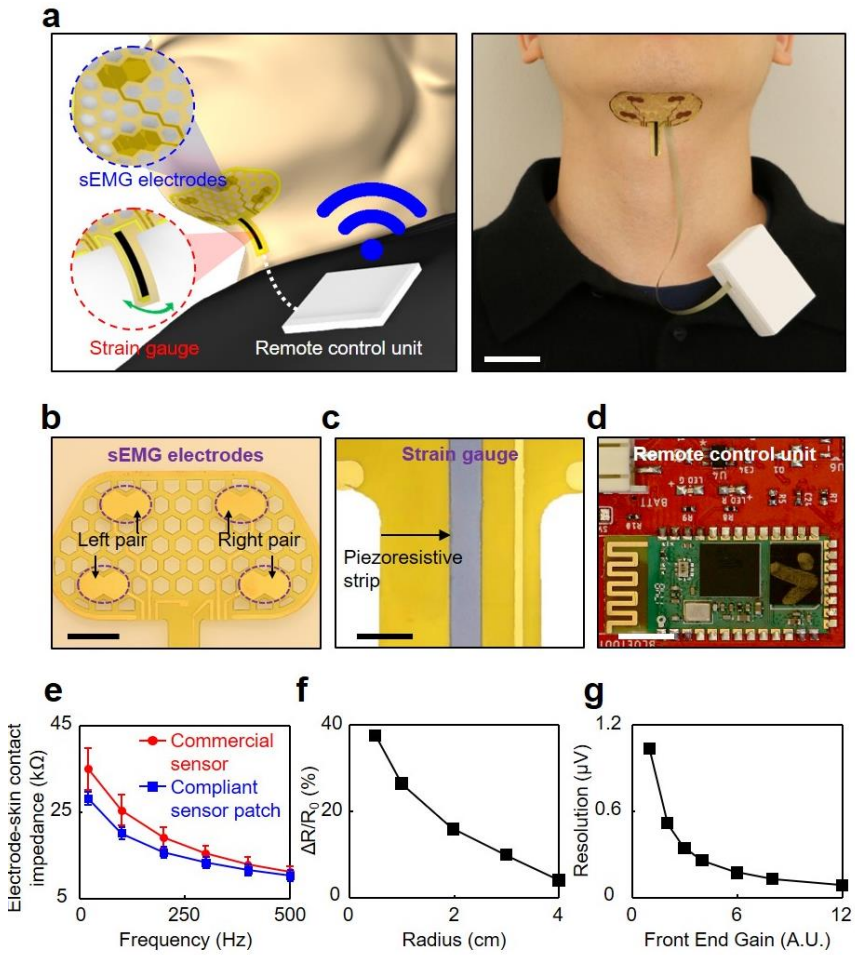

Figure 2.1. (**a**) Schematic illustration (left) and photo (right) of the sensor patch connected with a portable unit clipped on the wearer's clothing for remote data transmission and powering. Scale bar, 2.5 cm. (**b**) Enlarged photo of the sEMG recording electrodes. Scale bar, 1 cm. (**c**) Enlarged photo of the piezoeresistive strip in the strain gauge. Scale bar, 3 mm. (**d**) Photo of the unpackaged integrated circuit chip of the portable unit. Scale bar, 5 mm. (**e**) Measured electrode-skin contact impedances of the compliant recording electrodes (blue plot) by comparison with commercial recording electrodes (red plot). (**f**) Basic characterization of the strain gauge at various bending radii. (**g**) Basic characterization of the remote data transmission unit resolution at various gain settings. A.U., arbitrary units.

The construction of the sensor patch system occurs by exploiting cost-effective, affordable materials and fabrication methods. Table 2.2 outlines the estimated costs associated with the constituent electronic components, encapsulation and substrate materials, and processing fees at a laboratory scale, indicating that the total costs for the sensor patch and the portable remote-control unit are ~$13.92 and ~$52, respectively. Additional cost savings are expected by reusing the sensor patch multiple times for the same individual through sterilization with 70% ethanol, while the portable remote-control unit can be used across multiple patients until the end of its lifetime (years). Here, the sensor patch typically can be reused up to 5 to 10 times without any damage or defect, while the adhesion of the sensor patch to the skin becomes progressively less strong due to dust, sweat, facial hair, or other possible contaminants.

Figure 2.2. Sensor patch adhered to the submental area of subjects of different ages. Photos of the sensor patch placed on human subjects of different ages (26~64).

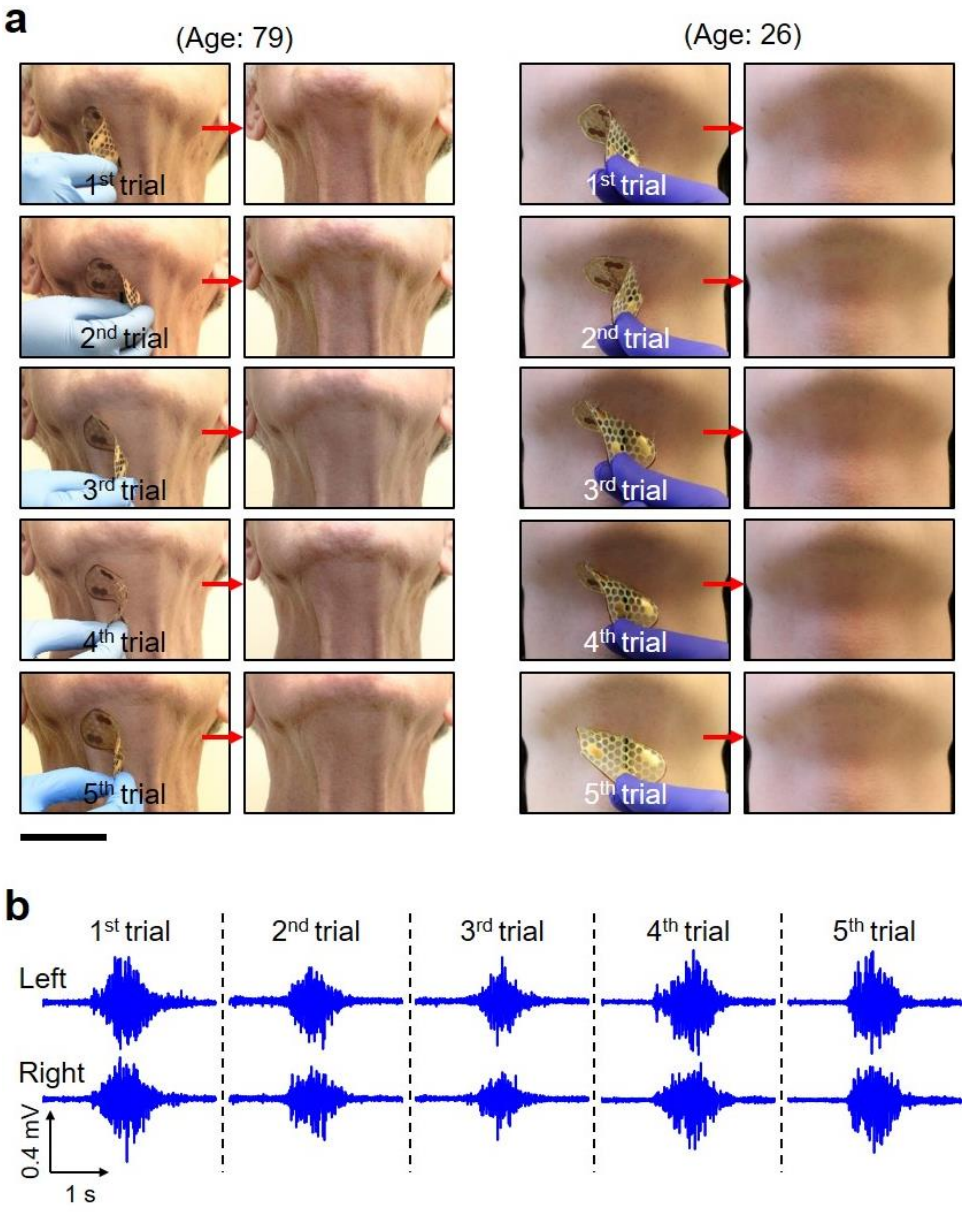

Figure 2.3. Repeated use of the submental sensor patch. (**a**) Photos of the sensor patch repeatedly attached and detached to/from the submental skin of human subjects of different ages – 26 and 79 years. The scale bar is 5 cm. (**b**) The corresponding sEMG obtained from these multiple trials (subject age: 26).

Table 2.2. Cost estimation of the submental sensor patch system. Outline of the estimated cost associated with the electronic components, encapsulation and substrate materials and processing fees at a lab scale for the sensor patch system.

	Name	Cost per device
Electronic components	Pyralux (PI/Copper clad)	$0.50
	Piezoresistive (Velostat)	$0.01
	ACF cable	$0.71
Packaging materials	PDMS	$0.05
	Silbione	$0.05
Processing materials	Photoresist Film	$0.10
	Process chemicals	$2
	Conductive adhesive	$1
Labor	$60/hr	$10
Sensor patch unit		$13.92
Wireless modules	PCB	$10
	Bluetooth module	$10
	ADC	$22
	Additional components	$10
Remote control unit		$52

2.3.2 Evaluation of design features in open honeycomb networks

The use of the sensor patch involves its direct attachment onto a curvilinear, dynamic, and anatomically complex body part, i.e., the submental area. For this to be accomplished, the requirements include design features that can provide comfort, resilience, and durability for at least the duration of a swallowing treatment session (typically 45 to 60 min). To realize these physical attributes, the overall structural layout of the sensor patch takes a form of open honeycomb networks[41-44], providing (i) oxygen permeability through wide-open mesh spaces for skin breathability and comfort, (ii) ability to deform in flexure for intimate contact with the curved surface of the submental area, (iii) density-specific elasticity that can accommodate external loads caused by head/neck movement, and (iv) damage tolerance for which the entire structure can retain its strength and function after minor damages or cuts. Several examples of the sensor patch configured in this way appear in fig. 2.4, where the characteristic honeycomb lattice length (l) is from 2 to 4.5 mm and width (w) is from 1 to 6 mm.

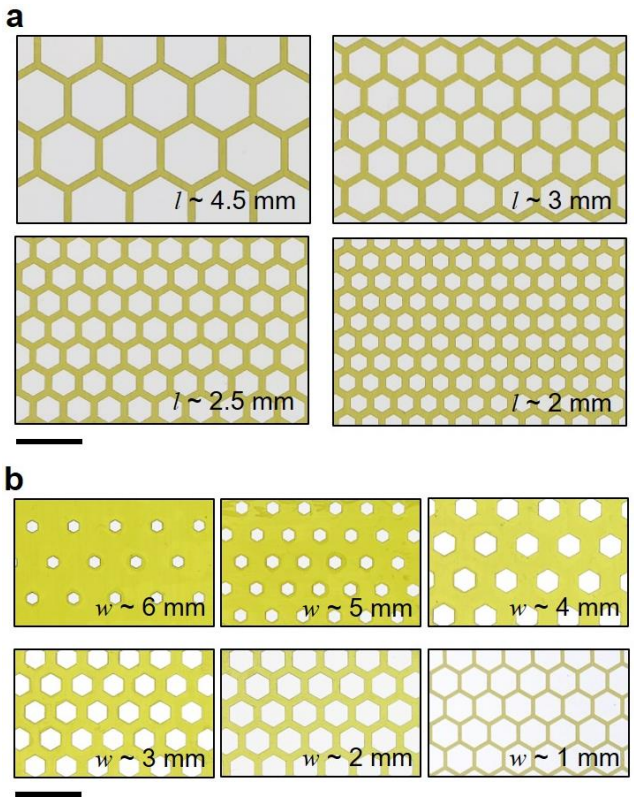

Figure 2.4. Hexagonal test bed geometrical variation. Photos of several testbed structures with (**a)** varies l = 2-4.5 mm and (**b)** w = 1-6 mm. The scale bars are 8 mm and 16 mm, respectively.

Figure 2.5 presents experimental observation (top) and the corresponding finite element analysis (FEA) results (bottom) obtained with a test bed structure (l = 4.5 mm, w = 1 mm) placed on an artificial skin substrate (Dragon Skin 30, Smooth-On Inc., 1:1 ratio by weight of parts A and B) under stretching at different loading angles of θ = 0° (left), 45° (middle), and 90° (right) by up to the maximum strain ($\mathcal{E}_{max}$) of ~10, ~4, and ~4% at the initial delamination of the test bed structure from the substrate. The results consistently confirm that the $\mathcal{E}_{max}$ concentrated at the hexagon edges remains below the limits for plastic deformation of ~16, ~6, and ~8% at θ = 0°, 45°, and 90°, respectively (Fig. 2.5). Under stretching beyond the $\mathcal{E}_{max}$, the honeycomb lattices become twisted out of plane to accommodate excessive strains and thereby substantially reduce the contact area (Fig. 2.5), allowing the wearer to more easily remove the sensor patch from the skin. This feature is especially important for the reusability of the sensor patch because it reduces the risk for skin irritation or damage to the sensor patch. Further enhancement of the stretchability is possible by incorporating state-of-the-art stretchable design layouts, such as filamentary serpentines[45], horseshoes[40], and self-similar fractals[46], into the sensor patch.

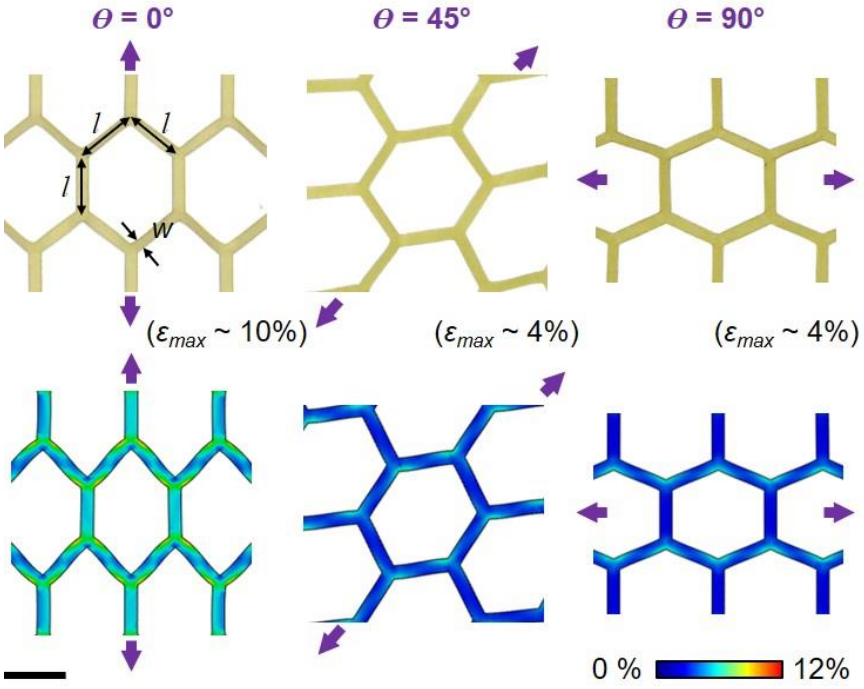

Figure 2.5. Experimental and computational (FEA) results for a test bed structure under stretching at θ = 0°, 45°, and 90° from the left. Scale bar, 4 mm.

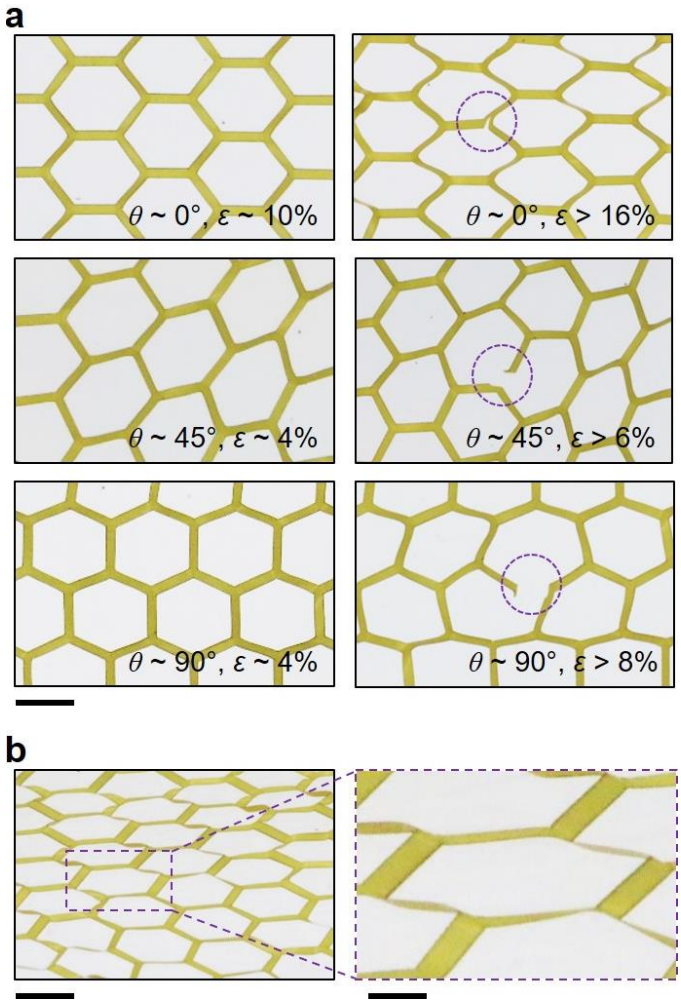

Figure 2.6. Hexagonal test bed under mechanical loads. (**a**) Photos of the testbed structures under stretched up to the limits (left) and beyond (right) plastic deformation (left) at θ = 0°, 45°, and 90°. The scale bar is 6 mm. (**b**) Photos of the testbed structure under excessive load, stretched and twisted out-of-plane. The scale bars are 6.5 mm (left) and 2 mm (right), respectively.

Figure 2.7a presents experimental, computational (FEA), and theoretical results that reveal the effect of θ on $\mathcal{E}_{max}$ before the first crack. At θ = 0°, the $\mathcal{E}_{max}$ remains roughly a factor of two times larger than others at θ = 45° and 90°, yielding consistent results with different values of l = 2 to 4.5 mm. For this reason, the honeycomb lattices are designed to be aligned along the vertical chin surface (θ = 0°) to efficiently accommodate head/neck movement that typically occurs in a vertical rather than horizontal direction during the use and removal of the sensor patch. Comprehensive computational (FEA) results that reveal the underlying mechanics of the honeycomb lattices under these conditions are summarized in Fig. 2.8. Notably, these characteristics are maintained even after several cuts (up to four cuts) of the honeycomb lattices, wherein the electrical conductance is

retained through the remaining conduction paths, even under 100 cycles of stretching at the maximum strain of ~16% (fig. 2.9, a and b).

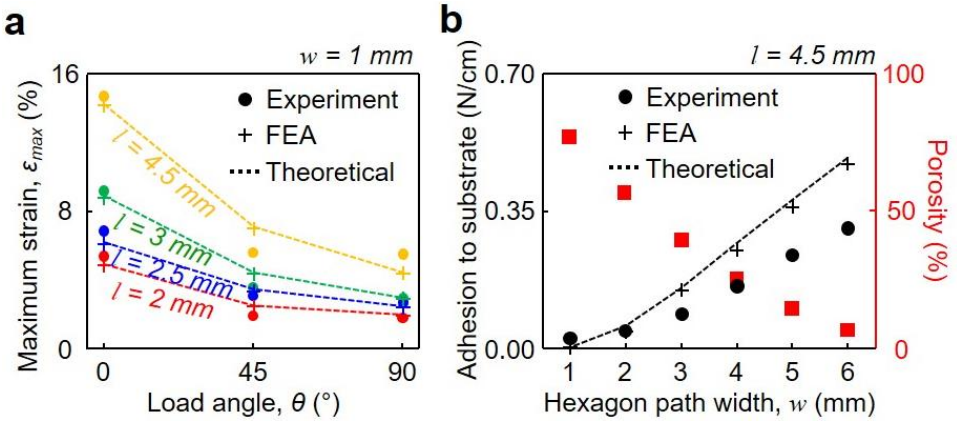

Figure 2.7. (**a**) Experimental, FEA, and theoretical results of the effect of θ on $\mathcal{E}_{max}$ with varied l = 2 to 4.5 mm. (**b**) Experimental, FEA, and theoretical results of the adhesive strength of the test bed structure with varied w = 1 to 6 mm.

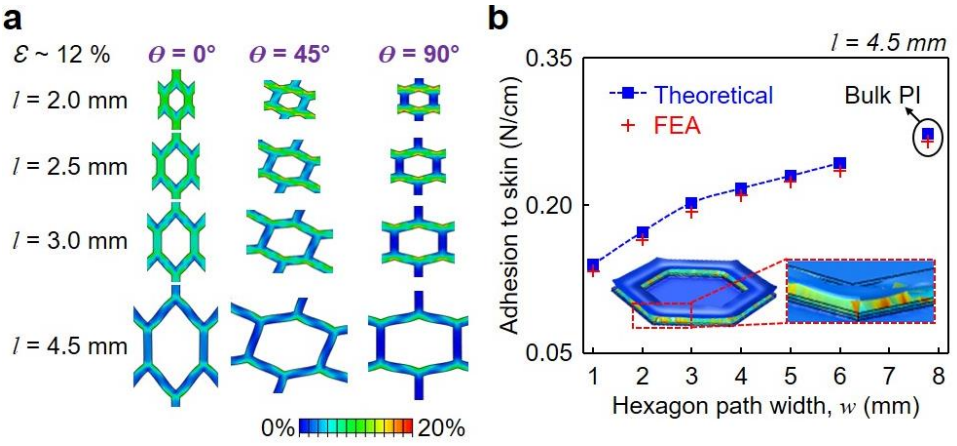

Figure 2.8. Mechanical simulation of test bed structures under mechanical loads. (**a**) The corresponding FEA results of the testbed structure under stretched at 12% with varies l = 2.0, 2.5, 3.0 and 4.0 mm at θ = 0°, 45° and 90°. (**b**) Computational (FEA) and theoretical results of adhesive strength of the testbed structure to the skin with varied w = 1-6 mm.

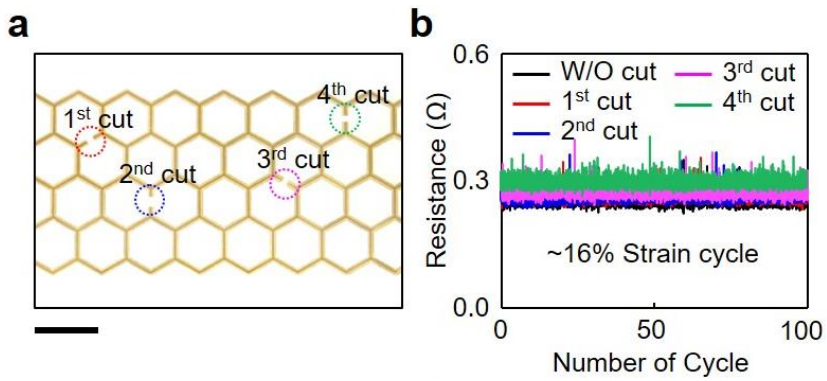

Figure 2.9. Electrical reliability and performance comparison. (**a**) Photo of the testbed structure with intentional cuts. The scale bar is 1.2 cm. (**b**) Measured resistance of the testbed structure under 100 cycles of stretching at the maximum strain of ~16%.

Intimate physical contact of the sensor patch to the submental skin is particularly important to provide a consistent electrode-skin interface and thereby ensure the attenuated noise from motion artifact[35]. The adhesive strength of the sensor patch is controlled by modulating the value of w (in turn, porosity), as it changes the effective surface contact area per given unit. Figure 2.7b provides experimental, computational (FEA), and theoretical results for the adhesive strength of a test bed structure (5.5 cm × 3.3 cm) as a function of w with fixed l = 4.5 mm and θ = 0°, obtained with a mechanical T-peeling tester (resolution, ±5 mN; Mark-10, Copiague, NY) that produces vertical peeling forces at constant rate of 4 mm/min. The increase in w results in monotonous enhancement of the adhesion strength, but at the same time yields reduced total area of open mesh spaces and thereby diminished skin breathability. Representative results of the computational and theoretical analysis for critical stresses (i.e., adhesion strength) at the interface between the skin and the sensor patch with l = 4.5 mm and w = 1 to 6 mm appear in fig. 2.8b. The results indicate that the sensor patch adheres to the skin wherein the adhesion strength increases as the w increases until the asymptotic limit of approximately 0.27 N/cm for the bulk structure (without the honeycomb networks). These findings provide guidelines for a tailored design of the open honeycomb networks, so that specific requirements and needs (e.g., skin breathability, deformability, and adhesive strength to the skin) for individual patients are met.

2.3.3 Remote monitoring of submental muscle activity and laryngeal movement

Simultaneous remote collection of both submental sEMG signals and strain waveforms (representing laryngeal movement) during swallowing and swallowing maneuvers is important in enabling accurate monitoring of swallowing events during the rehabilitation of dysphagia[47,48]. To demonstrate this, a pilot experiment was completed on a healthy young subject (23-year-old female). Specifically, sensor patch was attached onto the submental skin (after cleaning the surface with a rubbing alcohol wipe and applying a conducting gel to increase electrode-to-skin adherence) and ensured that the recording electrodes were aligned with the submental muscle fibers. The sEMG signals were then collected from the left and right submental muscles during swallows of 5 ml of Varibar thin liquid barium (catalog no. 105, E-Z-EM Canada Inc.) at the sampling rate of 1 kHz with 24-bit resolution and a reference (ground) electrode placed on the mastoid process (behind the ear). The remotely collected sEMG data were comparable to that obtained using a commercial (control) wireless unit (BioRadio, GLNeuroTech Inc.), providing the correlation of >0.95 at the sampling rate of >1 ksps (Nyquist rate) and the analog-to-digital resolution of 12 bit (fig. 2.10a,b). Postprocessing of the data was conducted to condition the sEMG signals with a finite impulse response bandpass Butterworth filter at the bandwidth of 20 to 500 Hz. The laryngeal movement during each swallow was simultaneously captured at the superior thyroid notch level (laryngeal prominence) where the strain gauge is located. The information associated with the laryngeal movement allowed us to identify the initiation, relative duration, and completion of a swallow event, which is useful in helping us differentiate the sEMG signals of interest from cross-talk sources originating from surrounding muscles.

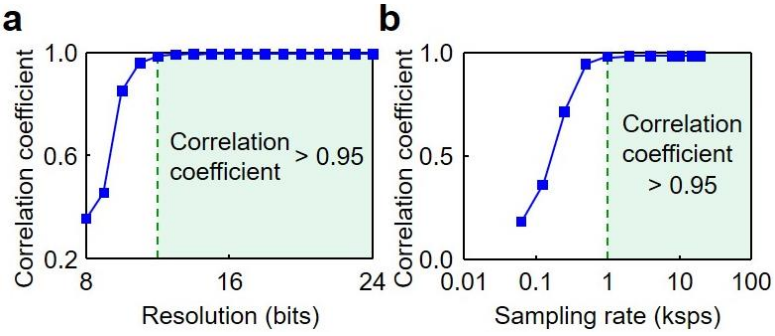

Figure 2.10. (**a**,**b**) The correlation of the sEMG signals obtained by comparing custom unit and a commercial unit (BioRadio) with varies signal acquisition resolution (**a**) and sampling rate (**b**).

Figure 2.11a (blue) presents the simultaneously recorded submental sEMG signals (top plots) and strain waveforms (bottom plot) during two swallows, recorded remotely via Bluetooth, with comparisons against the control measurements (red, Fig.2.11b). These graphs indicate the amplitude (force generation), duration, and relative onset and offset times of submental muscle activity. The sEMG signals collected via the sensor patch are comparable to those obtained with commercial sEMG recording patches (Red Dot, 3M). The results also show that the "W"-shaped strain waveforms consistently appear during the swallows and represent a rapid upward shift of the thyroid notch and the hyoid bone at the onset of swallowing (T1), followed by an anterior and superior movement to reach the most superior-anterior position (T2), and lastly, return to the original position upon completion of a swallow (T3). Based on the pilot study with a healthy subject, the strain sensor recorded strain range of <3% during various swallow maneuvers. Notably, these strain waveforms are effectively distinguishable at lower noise levels than those obtained using a standard nasal airflow cannula to detect swallow apnea (i.e., nasal airflow cessation during swallowing) as a control measurement. Figure 2.11c presents a series of screen-captured images from a simultaneous videofluoroscopic swallowing study (VFSS) recording at the characteristic time point of T1, T2, and T3, confirming the sequential correlations between the obtained strain waveforms and the thyroid notch and hyoid bone movement.

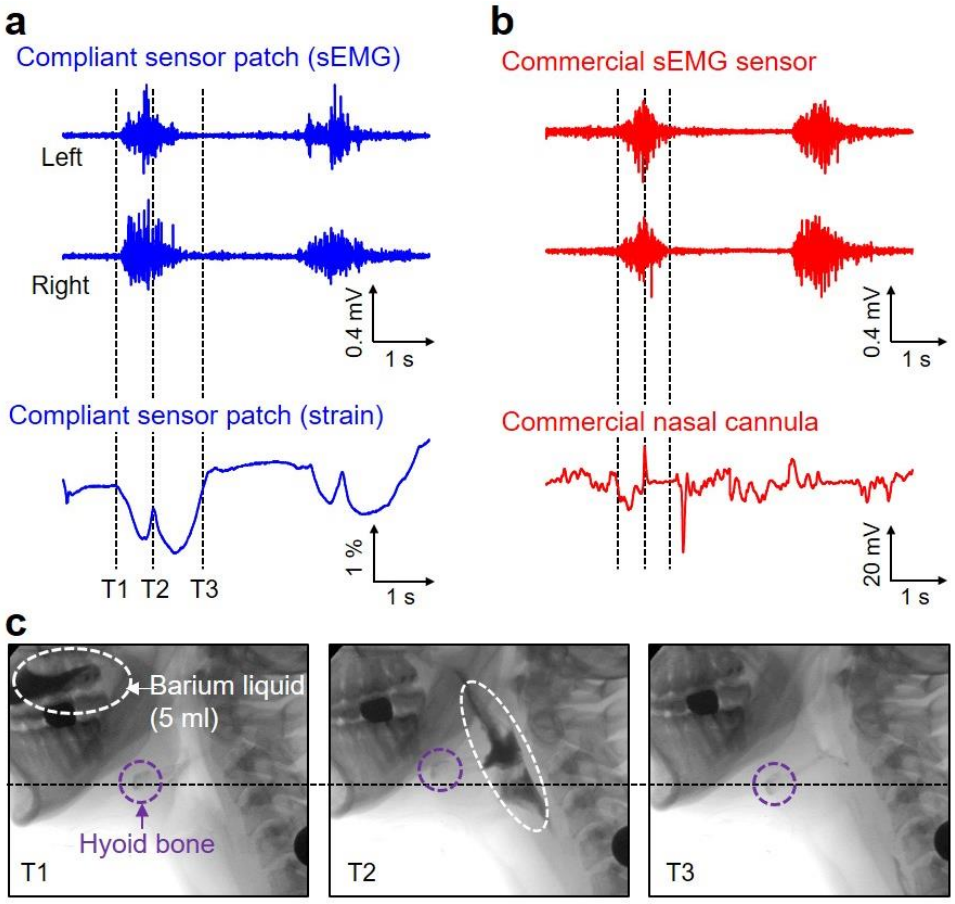

Figure 2.11. (**a**) Simultaneously recorded submental sEMG (top two plots) and strain waveforms (bottom plot) during swallows of 5 ml of barium liquid using the compliant sensor patch. (**b**) Simultaneously recorded submental sEMG (top two plots) and strain waveforms (bottom plot) during swallows of 5 ml of barium liquid using conventional commercial recording electrodes and a commercial nasal cannula, respectively. (**c**) A series of screen-captured images from the simultaneous VFSS recording at T1 (left), T2 (middle), and T3 (right). Scale bar, 5.5 cm.

2.3.4 Pilot application of the sensor patch system on a patient with dysphagia

To demonstrate feasibility and preliminary clinical validation, a pilot evaluation of the sensor patch system was conducted on a patient with dysphagia. The participant (70-year-old female) was diagnosed with Parkinson's disease (in 2017) and oropharyngeal dysphagia (in 2018). Her dysphagia was primarily characterized by inadequate pharyngeal constriction and reduced lingual strength, resulting in moderate amounts of pharyngeal residue with most consistencies and severe globus sensation (i.e., feeling of food getting stuck in the throat). At the time of her participation

in this study, the patient had received 8 weeks of intensive treatment for her swallowing difficulties[22]. The participant presented with normal cognition. The study took place in a university dysphagia clinic equipped with a videofluoroscopy C-arm system (OEC 9800 Plus Digital Mobile 12″ GE). A certified speech-language pathologist conducted the examination in the presence of a radiation technologist. The participant was seated in an upright position and in view of a laptop that was connected to a BioAmp system (GLNeuroTech Inc.). The researchers attached the sensor patch on the submental skin of the participant, and then the participant was asked to perform two swallows of each of a 5 ml Varibar thin liquid barium (catalog no. 105, E-Z-EM Canada Inc.), 10 ml Varibar thin liquid, and 5 cc Varibar barium pudding (catalog no. 125, E-Z-EM Canada Inc.). The participant was asked to perform additional swallows of 5 ml of Varibar thin liquid barium or 5 cc of Varibar barium pudding during the performance of two well-known swallowing maneuvers. These were the effortful swallows (used to improve pharyngeal constriction and bolus clearance) and the Mendelsohn maneuver (used to improve anterior and superior hyolaryngeal complex movement and upper esophageal sphincter opening)[49,50]. In general, rehabilitation protocols for dysphagia involve performing swallowing exercises to either strengthen the lingual, pharyngeal, and supralaryngeal muscles[22], or improve the planning, coordination, and timing of motor aspects of the swallow (i.e., skill-based training approaches)[51]. During these swallows and swallow maneuvers, submental sEMG signals were captured at the sampling rate of 1 kHz per channel, while the corresponding strain waveforms were simultaneously monitored to identify the relative timing of each swallow event. The swallowing process was further confirmed through simultaneous VFSS recording at full resolution (30 pulses/s) and speed (30 frames/s), along with the use of both a nasal airflow cannula and an observer's button pressing to further confirm the onset of the swallow events.

Figure 2.12 presents graphical displays of the measured data (black) obtained from the following swallows: 5 ml of liquid using an effortful swallow (Fig. 2.12a), 5 cc of pudding using an effortful swallow (Fig. 2.12b), 10 ml of liquid (regular swallow) (Fig. 2.12c), and 5 ml of liquid using the Mendelsohn maneuver (Fig. 2.12d), in comparisons with regular (control) swallows of 5 ml of liquid (blue) or 5 cc of pudding (red). The upper and lower hemispheres of each circular graph indicate values of mean normalized amplitude and burst duration of the sEMG signals, respectively. Compared with the corresponding raw data set (fig. 2.13), this graphical display

provides a user-friendly visualization of the amplitude and duration of submental muscle activity, making it easier for patients and clinicians to interpret and visualize the data and obtain biofeedback.

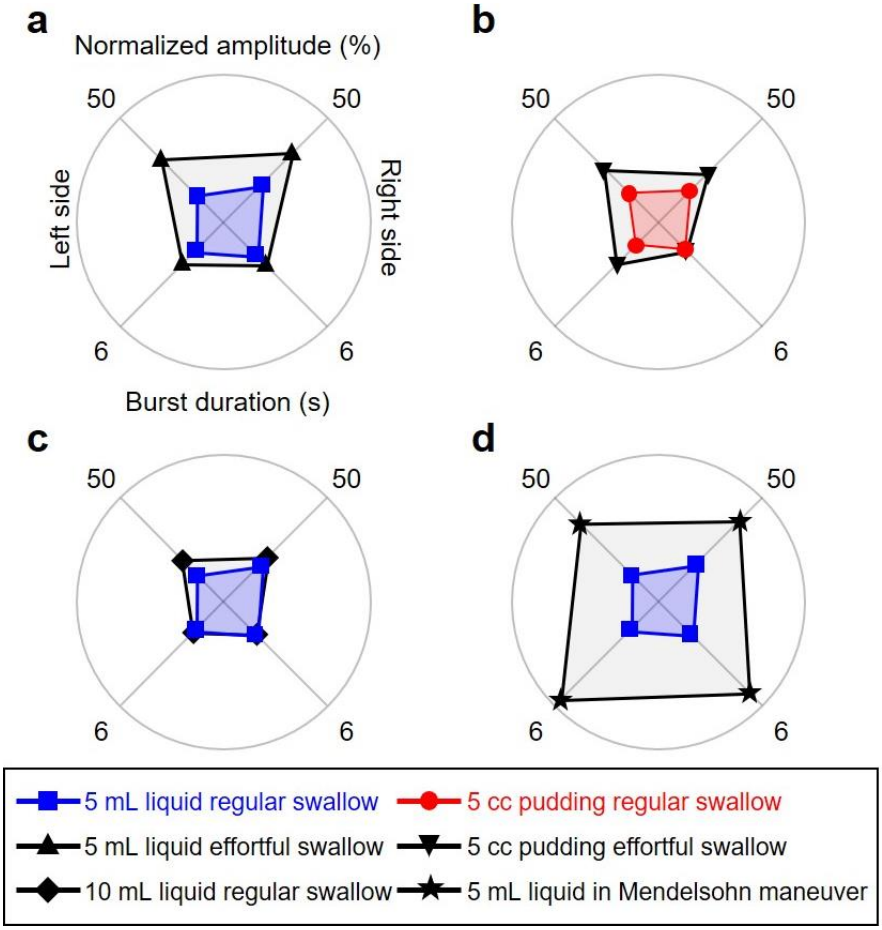

Figure 2.12. Pilot study on a patient diagnosed with Parkinson's disease and dysphagia (70-year-old female). Graphical displays (black color) of the measured data obtained from the following swallows: (**a**) 5 ml of liquid using an effortful swallow, (**b**) 5 cc of pudding using an effortful swallow, (**c**) 10 ml of liquid (regular swallow), and (**d**) 5 ml of liquid using the Mendelsohn maneuver, in comparison with regular (control) swallows of 5 ml of liquid (blue color) or 5 cc of pudding (red color).

These results confirm that the effortful swallows elicited higher submental muscle activity bilaterally (>20% of the patient's maximum) than the regular swallows (<20% of the patient's maximum) for both bolus types, although the effortful liquid swallows required higher amplitude than the pudding trials. The Mendelsohn maneuver elicited both increased amplitude and burst

duration of activity compared with the activity elicited by the regular swallows. Amplitude was increased by up to >200% and duration by >270%. The quantitative analysis summary of time-synchronized data of the submental sEMG signals and the VFSS recording from these trials these results appears in fig. 2.14. The data obtained from these measurements can provide clinically useful information in terms of identifying neuromuscular impairments[52], abnormalities in swallowing muscle activity and duration[53], and, more importantly, in providing feedback during swallowing rehabilitation regimens.

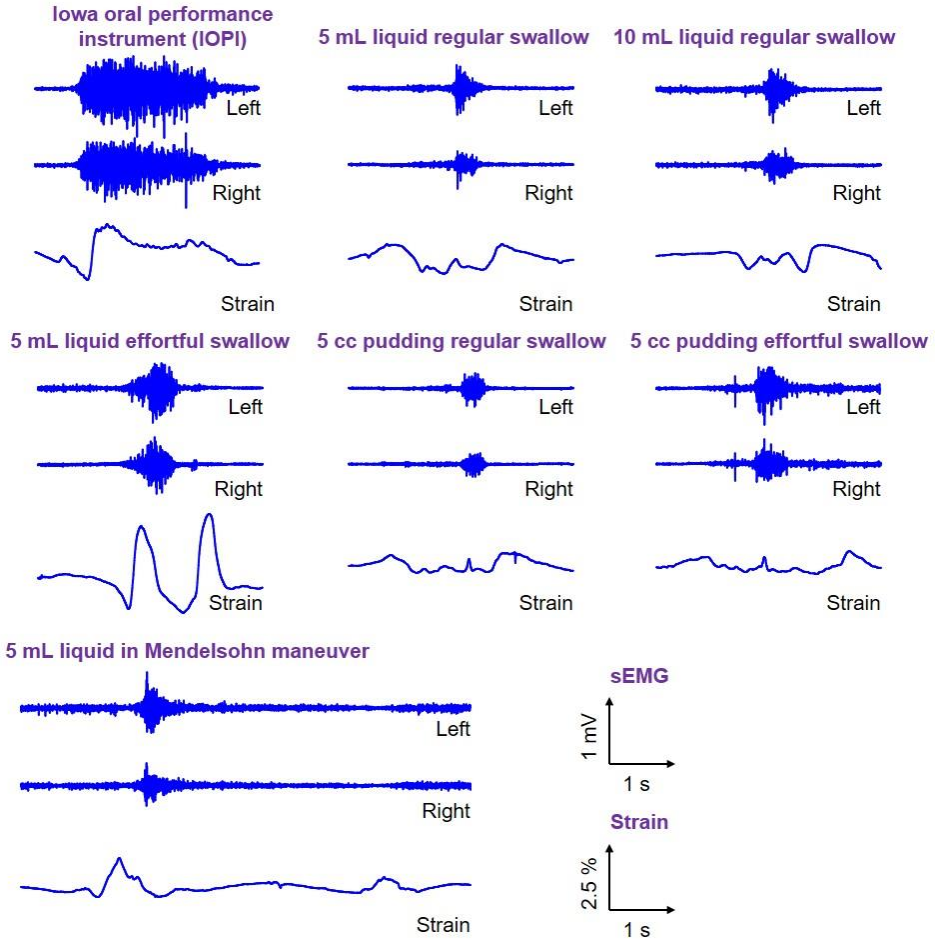

Figure 2.13. Swallowing treatment session results. The raw data of the measured sEMG signals and strain waveforms, resulting in the summary depicted in Fig. 2.12

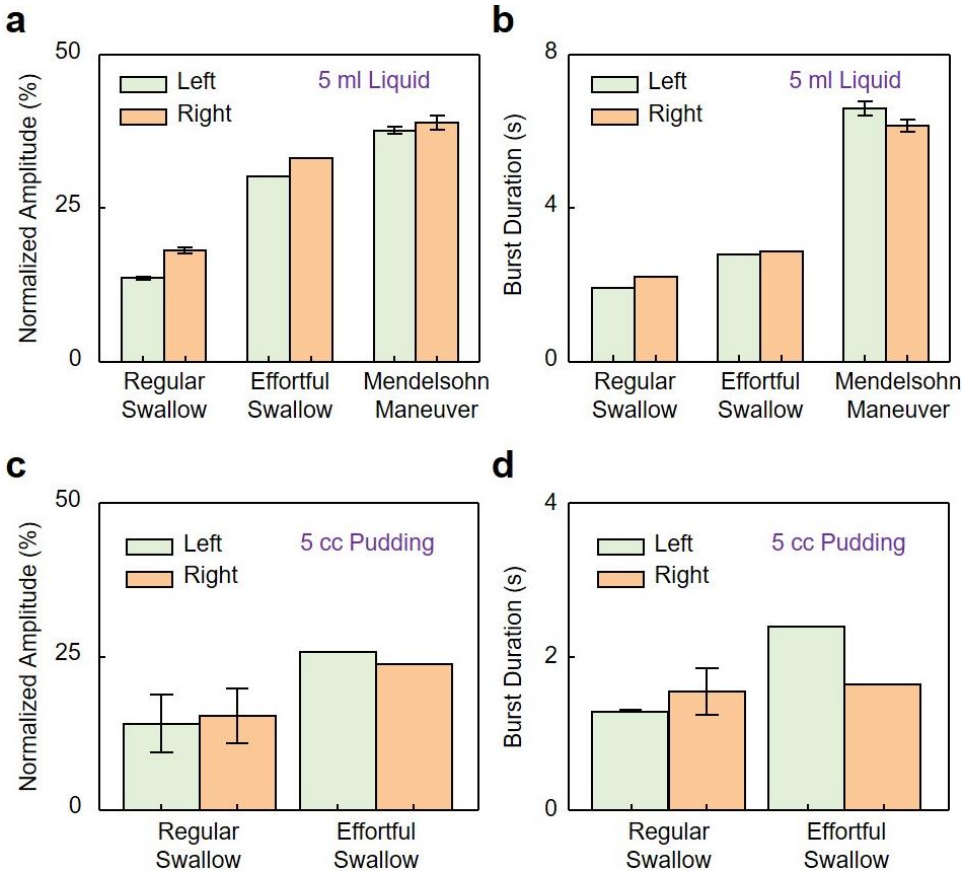

Figure 2.14. Swallowing treatment session data analysis. Summary of quantitative analysis in bar graphs for Fig. 2.12. (**a**) Normalized amplitude and (**b**) burst duration of 5 ml barium liquid swallows. (**c**) Normalized amplitude and (**d**) burst duration of 5 cc barium pudding swallows.

2.4 Discussion

The results reported here represent preliminary testing and validation of a user-friendly "bandage-like" skin sensor patch platform that is specifically designed for the submental area, and assess both muscle activity and laryngeal/thyroid notch movement during swallowing and swallowing maneuvers. Upon further validation and testing, the flexibly adherent profile and remote monitoring control feature of this platform will allow patients with dysphagia to easily practice their swallowing rehabilitative exercises at home while the data are remotely viewed and assessed in real time by a clinician in the clinic[54,55]. This can potentially minimize the need for repeat clinical visits and allow for optimal telerehabilitation protocols for dysphagia to be developed. The established materials, structures, and configurations of the sensor patch system provide a foundation that can be adjusted and upscaled for extended applications such as the

treatment of voice, speech, and other orofacial disorders[56], suggesting directions for future research. Extensive clinical evaluations on a large number of patients with dysphagia, which are ongoing, are needed to confirm the use of the sensor patch system across a wide range of age groups and patient diagnoses.

2.5 Acknowledgements

The figures, results and manuscript in this chapter is reprinted/adapted with permission from "Flexible submental sensor patch with remote monitoring controls for management of oropharyngeal swallowing disorder" *Science Advances*, 5, 12 eaay3210. Copyright 2020 American Association for the Advancement of Science. I express sincere gratitude to all of the coauthors on this journal publication, Dr. Cagla Kantarcigil (Purdue University), Bongjoong Kim (Purdue University), Dr. Ratul Kumar Baruah (Purdue University), Shovan Maity (Purdue University), Yeonsoo Park (Purdue University), Kyunghun Kim (Purdue University), Seungjun Lee (Purdue University), Jamie Bauer Malandraki (Purdue University), Shitij Avlani (Purdue University), Prof. Anne Smith (Purdue University), Prof. Shreyas Sen (Purdue University), Prof. Muhammad A. Alam (Purdue University), Prof. Georgia Malandraki (Purdue University), and Prof. Chi Hwan Lee (Purdue University).

3. GLOVE TYPE SENSOR FOR THE HAND AND FINGER AREA

3.1 Introduction

The human hand is one of the foremost parts of the body and serves as a versatile physical instrument for daily and social activities. Any disfigurement of this powerful physical instrument can affect a person's quality of life due to reduced manual dexterity and sensory reception and an unnatural appearance[57,58]. As a result, nearly 50% of all people with hand amputations require psychological intervention for isolation accompanied by depression, fatigue, anxiety, or even suicidal ideation[58,59]. Current evidence-based treatments rely on the use of the prosthetic hand(s) to restore vital mobility that is important in many daily and social interactions, such as gripping, handshakes, gentle stroking, and petting[60,61]. The recent development of flexible and stretchable materials and electronics provides both mechanical softness and sensory perception to detect changes in external stimuli including pressure, temperature, and hydration [9,62-66]. However, the seamless integration of these materials around prosthetic hands is still challenging due to geometric complexity, resulting in continued disfigurement and poor physical coupling. The ability to directly assemble flexible and stretchable electronic circuit materials and devices on a commercial stretchable glove could provide an easy-to-wear seamless platform suitable for arbitrary prosthetic hands[67-69].

Herein, a set of advanced materials, design layouts, and fabrication schemes are presented for the realization of an electronic sensory glove (e-glove) system that is directly built on a commercial stretchable nitrile glove, allowing seamless fit on arbitrary prosthetic hands through the intrinsic ergonomic design of the glove for any hand shapes and sizes within the regular range of adult hand sizes. The e-glove system is configured with flexible and stretchable forms of multimodal sensors to collect various types of information, such as pressure, temperature, and moisture while simultaneously offering realistic human hand-like appearance, softness, and warmth. The capabilities of the real-time display of the sensory data measured on a control wristwatch unit and

remote transmission to an external reader for data postprocessing provide benefits and convenience to the user. The fabrication of the e-glove system involves a cost-effective hybrid printing technology that combines screen-printing and transfer-printing methods and is tailored to laminate multiple layers of electronic circuit materials on a commercial stretchable glove. Both the experimental and computational investigations reveal key features of the underlying materials and structures and the mechanics aspects of the design variables. The results demonstrate the utility of the e-glove system during the interactions and control of a prosthetic hand with objects and humans in many daily and social settings.

3.2 Materials and methods

3.2.1 Finite element analysis (FEA)

The commercial software ABAQUS (standard 6.13) was used to study the mechanical behavior of the prototype devices under stretching, bending and folding. A multilayered model was built, i.e., an encapsulated (h_{encap} = 500 μm)-PDMS/Ag (h_{PDMS} = 80 μm, h_{Ag} = 45 μm)-epoxy adhesive (h_{epoxy} = 70 μm)-nitrile glove (h_{PDMS} = 150 μm) composite. Since a serpentine-shaped Ag trace was embedded in the PDMS, a partition of exactly the same shape as the serpentine layout was created with effective mechanical properties, e.g., Young's modulus:

$$E_{eff} = E_{Ag}\left(\frac{h_{Ag}}{h_{PDMS} + h_{Ag}}\right) + E_{PDMS}\left(\frac{h_{PDMS}}{h_{PDMS} + h_{Ag}}\right)$$

where $E_{Ag} \approx 0.2$ MPa (obtained from the vendor) and $E_{PDMS} \approx 2.5$ MPa. For the epoxy adhesive layer and glove, $E_{epoxy} \approx 3.38$ MPa (urethane based), and $E_{glove} \approx 21$ MPa (from the product sheet). Because the thickness of each layer (~mm) was substantially smaller than the lateral dimensions of the device (~cm), the device was modeled as a composite shell with element S4R. Incompressible neo-Hookean constitutive behavior was assigned to all the layers.

3.2.2 Thermal analysis

COMSOL 5.3 electric currents and heat transfer modules were used for the time-dependent joule-heating simulation. The heat was generated when an electric current of 0.24 A was applied

to the serpentine-shaped Ag traces. The heating time was 2 min. The thermal properties of the materials were obtained from the vendor product sheets and https://thermtest.com/materials-database.

3.2.3 Fabrication of the e-glove system

The fabrication began with a commercial stretchable nitrile glove (Kimberly-Clark, Irving, TX, USA) by gluing an epoxy (Loctite 4902, Henkel, Rocky Hill, CT, USA) over the surface to provide adhesive support, followed by curing in an oven at 70 °C for 10 min. A conductive Ag ink (125–19FS, Creative Materials, Ayer, MA, USA) was screen-printed on the surface of the glove to define the electrical interconnectors through a mesh screen (Ryonet, Vancouver, WA, USA) featured with photolithographic-patterned filamentary serpentine traces. Active sensing elements were then delivered from the donor substrate to the desired locations of the glove in a spatially distributed manner by using sequential transfer printing operations. Subsequently, the glove was annealed in an oven at 70 °C for 2 h to secure the bonding between the sensing elements and the conductive Ag ink. The entire structure was dip-coated in an uncured silicone elastomer (EcoflexTM, Smooth-On, Macungie, PA, USA) to form a thin sealing layer on the surface, followed by complete curing at 70 °C for 30 min. The steps of transfer printing and dip-coating were iterated to stack multiple layers consisting of different types of sensors. A subsequent dip-coating of the entire structure with a silicone elastomer (Dragon Skin Series, Smooth-On) to form the outermost skin layer completed the fabrication.

3.2.4 Incorporation of human hand-line appearance into the skin layer

The process began by gently pouring a solution of silicone elastomer (Body Double^{TM}, Smooth-On) on a volunteer's hand to generate a custom-fitted mold. An agent, a 1:4 mixture of petroleum jelly and mineral spirits, was applied to the interior surface of the mold for an easy and clean release. A mixture of silicone elastomer (Dragon Skin Series, Smooth-On, USA) and skin-tone colorant (Slig-Pig^{TM}, Smooth-On, USA) was thinly applied to the interior surface of the mold. The aforementioned as-prepared e-glove was placed inside the mold and then annealed at room temperature for 1 hour. The release of the cured structure from the mold completed the process.

3.2.5 Fabrication of custom control wristwatch unit

The fabrication began by printing a wristwatch case and buttons by using 3D printing equipment (Fortus 400mc, Stratasys, Eden Prairie, MN, USA) with a fused deposition of ABS (Acrylonitrile butadiene styrene) plastics. The internal printed circuit board (PCB) was fabricated on a Cu/PI film (12 μm/12 μm thick, Pyralux AP121200EM, DuPont, Durham, NC USA). A dry film photoresist (Riston MM540, DuPont, USA) was applied to the Cu/PI film by using a hot roller laminator (AL13P, Apache Laminator, USA), followed by photolithographic patterning and a wet etching process (CE-100, Transene Company, Danvers, MA, USA) to form the solder pads and traces. The resulting metal patterns were electroplated with a layer of tin (Sn) (Bright Electroless Tin, Transene, USA) for oxidation protection. Other necessary electronic components such as a microcontroller unit, multiplexer, and switches were soldered on the PCB and assembled inside the 3D printed wristwatch case along with an organic light-emitting diode (OLED) display (1673, Adafruit Industries, New York, NY, USA). The rigid housing case was thoroughly sealed with insulating tape (Kapton) to reduce the risk of potential short circuits. A summary of the electronic components used in this unit appears in Table 3.1. Finally, the entire structure was mounted on a commercial wristband by using an epoxy adhesive.

3.2.6 Fabrication of artificial hand

The fabrication began with fused deposition of ABS plastics using 3D printing equipment (Fortus 400mc, Stratasys, USA) to print 15 components consisting of both the finger and palm sections. They were assembled using cyanoacrylate adhesive and neoprene rubber sheets (2 mm thick) to form the basic structural frame of a hand. Each joint of the artificial hand was connected with fishing lines (Sufix 832, Rapala VMC, Minnetonka, MN, USA), allowing movement of the fingers and thumb by external adjustment of the line tension.

Table 3.1. Summary of the electronic components used in the custom wristwatch unit.

Components	Manufacturer	Part Number
ADC	TI	ADS1115
Arduino Pro Mini	Sparkfun	Dev-11114
Battery	Adafruit	2750
BJT (PNP)	ON semiconductor	MMBT2906SL
Capacitance-to-digital converter	Ti	FDC1004
Capacitor	Murata Electronics	1uF
Capacitor	Murata Electronics	10uF
Capacitor	Murata Electronics	0.1uF
Ferrite Beads	TDK	MMZ2012Y152B
Inductor	Murata Electronics	4.7uH
Instrumentation Amp	Ti	INA333
Mux (16ch)	Analog devices	ADG1606
Mux (32ch)	Analog Devices	ADG732
NMOS	Vishay	IRF630
Oled display	Adafruit	1673
Opamp	Ti	TLV333
PIN Diode	Rohm Semiconductor	RN142ZS
Power Regulator	Ti	TPS61097
Resistor	Panasonic electronic components	10kΩ
Resistor	Panasonic electronic components	4.99kΩ
Resistor	Panasonic electronic components	5kΩ
Resistor	Panasonic electronic components	25kΩ
Switch	C&K	KXT 331LHS
Voltage Reference	Ti	REF3330
Wireless Unit/uC	Simblee	RFD77101

3.2.7 Recording of pressure and temperature

The arrays of pressure and temperature sensors were configured in the same way. Custom-miniaturized constant current preamplifier circuits consisting of op-amp (TLV333, Texas Instruments, Dallas, TX, USA) and bipolar junction transistors (BJT, MMBT3906SL, ON Semiconductor, Phoenix, AZ, USA) were used to supply a constant current of 100 μA to the sensors. Multiplexers with 32 channels (ADG726, Analog Devices, Norwood, MA, USA) controlled by a microcontroller unit (RFD77101, RF Digital, Hermosa Beach, CA, USA) were used to switch between the sensors while the voltage drop was measured across the sensing elements during recording. The changes in the voltage corresponding to external stimuli of pressure and temperature were measured by a 16-bit resolution analog-to-digital converter. The data measured were displayed on the control wristwatch unit and simultaneously transmitted to an external reader such as a commercial smartphone or tablet via Bluetooth communication.

3.2.8 Recording of hydration

A capacitive hydration sensor with interdigitated microelectrode arrays was assembled on the index fingertip of the e-glove. To facilitate the direct contact of the embedded hydration sensor with environmental moisture, a 3 × 3 array of small openings (~1 mm each in diameter) were punched through the outermost skin layer on the fingertip. A capacitance-to-digital converter (FDC1004, Texas Instruments, USA) was used in conjunction with a microcontroller unit (RFD77101, RF digital, USA) to measure the capacitance during recording. The data were processed by the microcontroller unit and then displayed on the control wristwatch unit and remotely transmitted to an external reader such as a commercial smartphone or tablet.

3.2.9 Fabrication of networked Ag nanowire mesh

The fabrication began by synthesizing Ag nanowires with a mixture of 50 mL of ethylene glycol (EG, 9300–03, J.T.Baker, Radnor, PA, USA), 400 μL of copper (II) chloride (CuCl2, 4 mM, 487847, Sigma-Aldrich, St. Louis, MO, USA), and 15 mL of polyvinylpyrrolidone (PVP, 0.147 M, 856568, Sigma-Aldrich, USA) in a preheated oil bath (CG-1100, Chemglass, Vineland, NJ, USA) at 150 °C for 1 hours[70]. Approximately 15 mL of Ag nitrate (AgNO3, 0.094 M) was injected at a rate of 0.5 mL/min by using a syringe pump (AL-4000, World Precision Instruments, Sarasota, FL, USA) until the color of the solution changed from ivory to grey. This step was repeated 3~5 times while adding 10 mL of the mixed precursor solution in each step. The resulting solution was cooled to room temperature, followed the addition of 450 mL of acetone. The mixture was then centrifuged to extract the Ag nanowires from the mixture. The as-prepared Ag nanowires were filtered through a Teflon filter (0.2 μm pore size, Sterlitech, Kent, WA, USA) by using a vacuum-assisted Buchner funnel (1960–054, Whatman, UK) to form a sheet of highly networked Ag nanowire-mesh.

3.2.10 Fabrication of electrophysiological recording electrodes

The previously mentioned as-prepared networked Ag nanowire-mesh was placed on a Si wafer coated with bilayers of poly(methyl methacrylate) (PMMA, 1 μm) and PI (1 μm) on the surface, followed with standard photolithography and reactive-ion-etching (RIE) etching to define the necessary patterns in filamentary serpentine traces for the electrophysiological (EP) electrodes. The resulting structure was immersed in a solution of acetone for ~1 h to dissolve the PMMA layer, allowing the EP electrodes to release from the Si wafer to subsequently be installed in the e-glove.

3.2.11 Recording of EP signals

The EP recording electrodes were installed around the tip of the thumb of the e-glove. Then, the EP electrodes were attached to the skin of the chest and forearm of a volunteer (age: 30) during the recording of electrocardiogram (ECG) and electromyogram (EMG) signals, respectively. The signals measured were remotely sent to an external computing system by using a portable wireless unit (BioRadioTM, Great Lakes NeuroTechnologies, Cleveland, OH, USA) that was connected to the e-glove. Commercial software (BioCapture, Great Lakes NeuroTechnologies, USA) was used with filtering at 60 Hz and bandpass at 0.5~100 Hz (ECG) and 10~500 Hz (EMG). The filtered data were remotely exported to MATLAB for data postprocessing.

3.2.12 Studies on human subjects

All the studies on human subjects were approved by the Purdue Institutional Review Board (protocol #: 1711019949) and conducted in compliance with the applicable regulations.

3.3 Results

3.3.1 Basic layouts and configurations of the e-glove system

Figure 3.1a shows a series of optical images of a representative e-glove platform that contains multiple stacked arrays of sensor elements (insets), including (1) a total of 20 pressure sensors (6.5 mm × 4.6 mm each) evenly distributed over the entire area, (2) a capacitive-based moisture

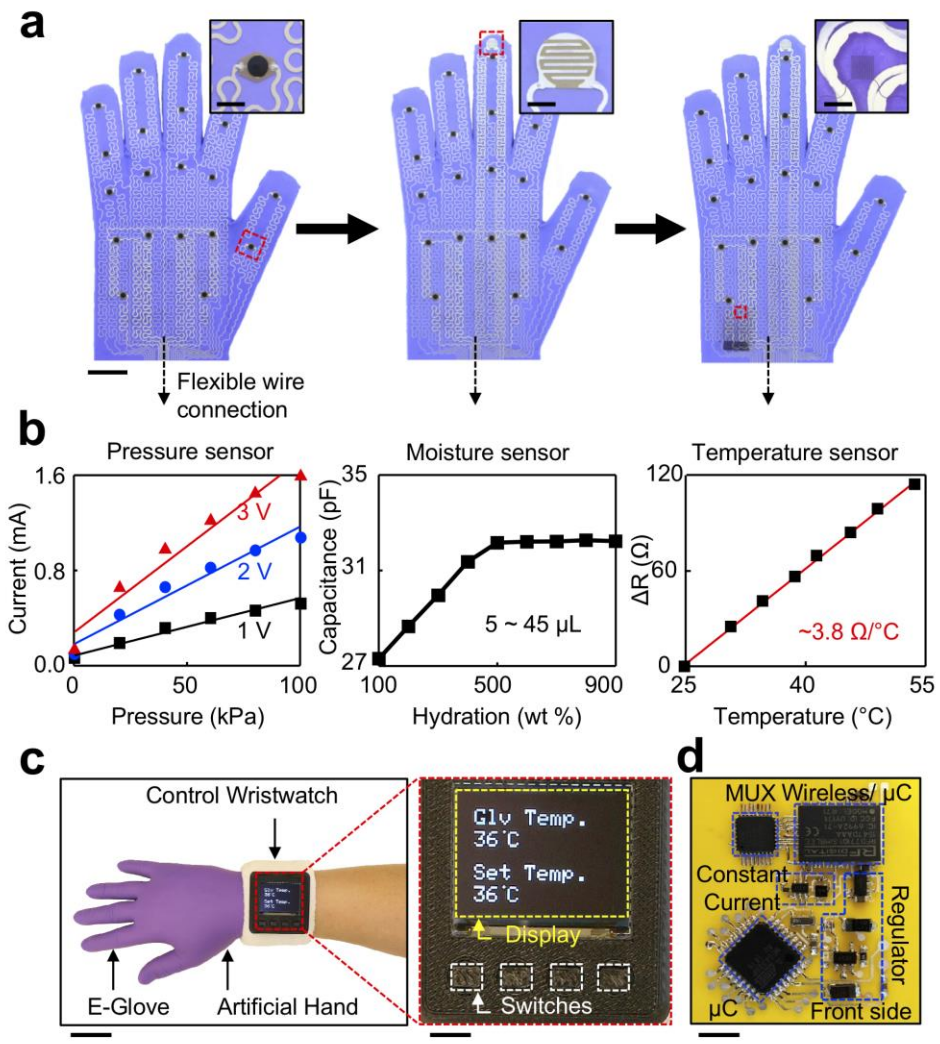

Figure 3.1. Basic layouts and configurations of the e-glove system. (**a**) A series of optical images for a representative e-glove platform that contains multiple stacked arrays of sensor elements including pressure (left), moisture (middle), and temperature (right) sensors. Scale bar is 25 mm. The inset images show an enlarged view of the embedded sensor elements. Scale bars are 4 mm (left), 3 mm (middle) and 1 mm (right), respectively. (**b**) Representative electrical characteristics of the embedded sensor elements as a function of externally applied stimuli. (**c**) Optical images of a custom-built wristwatch unit connected to the e-glove system. Scale bars are 6 cm (left) and 1 cm (right), respectively. (**d**) Optical image of the embedded internal circuitry in the wristwatch unit. Scale bar is 5 mm.

sensor (7 mm × 6.3 mm) on the index fingertip, and (3) 16 resistive-based temperature sensors (1 mm × 1 mm each) at the center of the palm. The representative electrical characteristics of the embedded sensor elements as a function of the externally applied stimuli are summarized in Fig. 3.1b. The results indicate that the sensitivities of the pressure, temperature and moisture sensors

are ~10 μA/kPa, ~1 pF/20 μL moisture level, and ~0.6 mV/°C within the ranges of the applied pressure of 0~200 kPa, moisture of 0~100%, and temperature of 20~50 °C, respectively, without suffering any degradation in performance. The fabrication begins by gluing a thin layer of a flexible epoxy (Loctite 4902, Henkel, USA) on the surface of a commercial stretchable nitrile glove (Kimberly-Clark, USA) to serve as an adhesive. Subsequent screen-printing of a flexible Ag paste (125–19FS, Creative Materials, USA, ~0.05 Ω/sq/mil) configured with a fractal serpentine layout (inset image) defines a stretchable form of conducting interconnectors. The employment of a pick-and-place transfer printing method results in the delivery of active sensor elements to predefined locations in an array layout that meets the spatial resolution requirements[71-73]. Dip-coating of the entire structure in an uncured silicone elastomer (EcoflexTM, Smooth-On, USA), followed by complete curing at 70 °C for ~30 min, leads to a thin sealing layer (~300 μm thick) over the surface to serve as electrical insulation for the subsequent layer. These steps can be iterated to provide stacked layers of sensor arrays for multimodal sensing capabilities. Finally, lamination of another thin sealing layer (~300 μm thick) with a silicone elastomer (Dragon Skin Series, Smooth-On, USA) forms the outermost skin layer not only to provide human skin-like mechanical softness and resilience but also to ensure the mechanical integrity and reduce any potential risk of interfacial delamination[74]. The details of the assembly procedures appear in the materials and methods section of this chapter.

The abilities to provide a real-time display of the sensory data measured and to remotely transmit the data to an external reader (e.g., commercial smartphone or tablet) for data postprocessing can improve the workflow between the e-glove system and the user, thereby offering operational efficiency and convenience. Figure 3.1c shows a custom-built control wristwatch unit that is wired to the e-glove system via a flexible anisotropic conductive film (ACF) cable (HST-9805–210, Elform, Fallon, NV, USA). The enlarged image highlights the organic light-emitting diode (OLED) display for the display of information, user interface navigation, and operational switches for function setting and control. The internal circuitry (Fig. 3.1d) of the control wristwatch unit includes (1) a 32-bit ARM Cortex M0 processor-based microcontroller (RFD77101, RF Digital, USA, 10 × 7 × 2.5 mm) for data collection and wireless transmission via BluetoothTM, (2) a rechargeable lithium polymer battery (3.6 × 2.0 × 0.56 cm, 350 mAh) for a power source, (3) a differential amplifier (INA333, Texas Instruments, USA) for front end

detection and amplification of electrical signals, and (4) a 3D-printed package made of ABS plastics for housing. The schematic diagram of the embedded circuits appears in Fig. 3.2, the fabrication details are described in the materials and methods section. The whole system is powered by a rechargeable lithium polymer batter and the voltage is regulated to 3.3 V using a voltage regulator (TPS61097, Texas Instruments). Also, a voltage reference module (REF3330, Texas Instruments) is used to provide analog reference level to the microcontroller and to the analog-to-digital converter. Pressure and temperature sensor array are configured as a common anode configuration where a constant current source was preconfigured to deliver a set amount of current based on the sensor type and expected resistance range. Multi-channel analog multiplexer is used to switch through the sensor array grounding the cathode one sensor at a time with the refresh rate of 60 Hz. The multiplexer only allows preset current to flow through a single sensor element at a time as it switches through the array. The switching of multiplexer is controlled by the onboard microcontroller, which also measures the applied voltage at the sensor anode with an analog-to-digital converter after each switch to calculate the sensor resistance in turn, its pressure or temperature value based on the characterization curve (Figure 3.1b). The use of the wristwatch allows the provision of immediate feedback to the prosthetic user through visual cues, which can provide two-dimensional data perception/visualization customizable to individual needs.

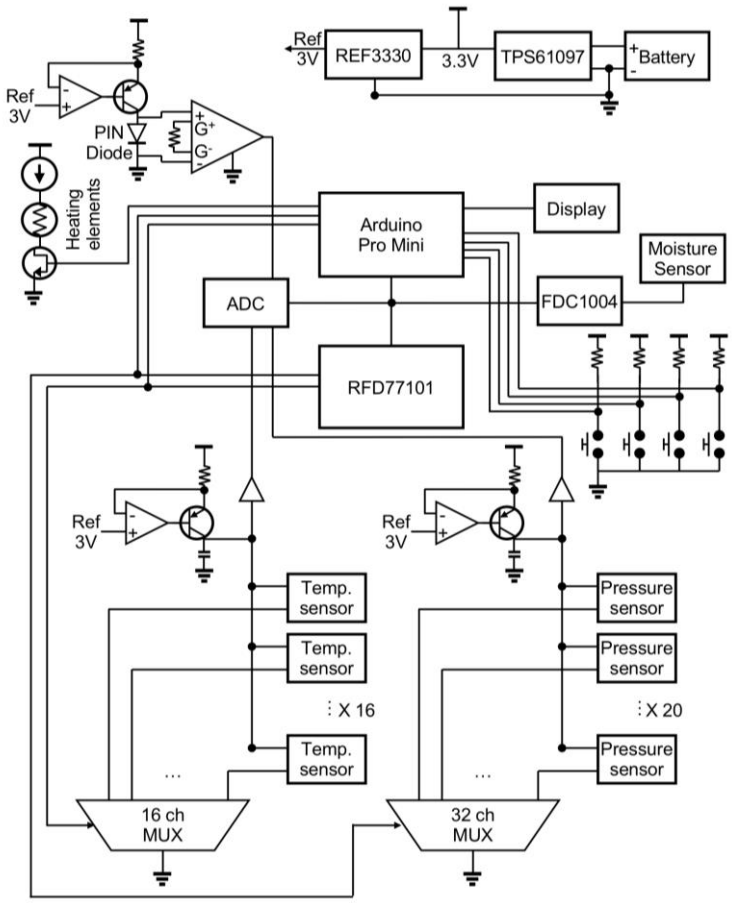

Figure 3.2. The overall workflow diagram of the embedded circuits in the wristwatch unit.

3.3.2 Demonstration of human hand-like multimodal perception

Prosthetic hands encounter many complex operations in daily and social activities including shaking a hand, tapping or punching an object, and holding hot/cold and dry/wet surfaces [60]. Given these circumstances, the real-time detection of pressure, temperature, and hydration from a prosthetic hand can provide useful information to the user. To illustrate this possibility, representative uses of the e-glove system in several daily circumstances envisioned are demonstrated by using a 3D-printed artificial hand as a surrogate for a prosthetic hand (Fig. 3.3). Figure 3.4a shows an optical image of the e-glove grasping a baseball; the monitoring of the pressure exerted across the whole palm area is carried out by an array of 20 pressure sensors. The inset image shows an embedded single sensor element that includes a pressure-sensitive polymer (Velostat™, 3 M, Maplewood, MN USA). Figure 3.4b presents the results of postprocessed data,

revealing detailed visual information about how hard/easy the prosthetic hand holds the baseball in a spatially resolved manner. Representative results of the electrical characteristics of the embedded sensor element appear in Fig. 3.4c, exhibiting a sensitivity of ~4 μS/kPa. The results indicate that the e-glove system is capable of distinguishing delicate changes in pressure that a human hand might experience in daily activity with a dynamic range (linear response) up to ~100 kPa.

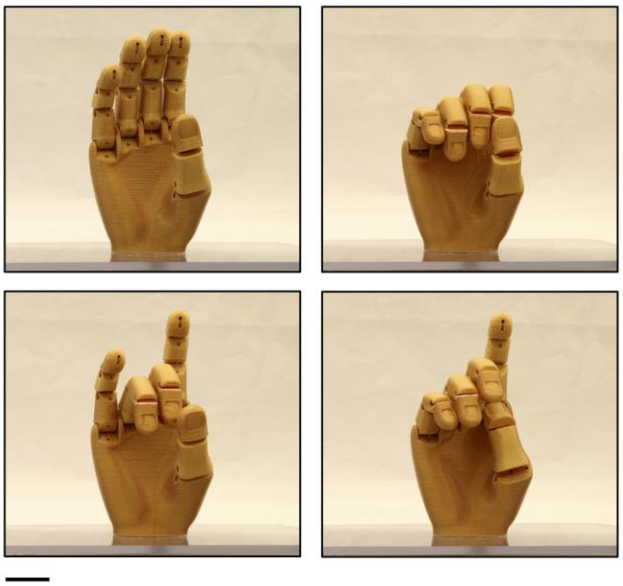

Figure 3.3. Optical images of a 3D printed prosthetic hand articulating various gestures, controlled by strings attached to each finger. Scale bar is 3 cm.

The effects of different skin layer thickness (100~500 μm) and changes in environmental temperature (30~50 °C) on the pressure sensor performance appear in Fig. 3.4d and e. The varying thickness of insulation does not have an effect on the pressure sensor performance since the load was applied vertically. The changing temperature did not cause notable changes in the piezoresistive sensing elements within the expected operating temperature. The experimental results characterizing the repeatability and reliability of the sensor under cyclic loading at different levels of applied pressure are summarized in Fig. 3.4f showing that the sensing element demonstrates high repeatability.

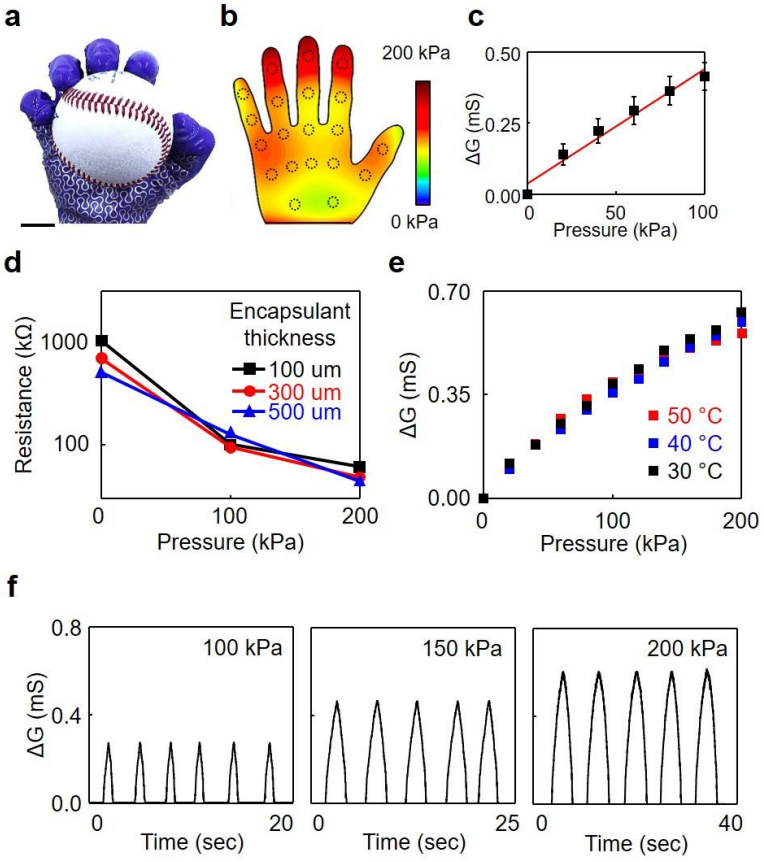

Figure 3.4. Demonstration of human hand-like pressure perception. (**a**) Optical image of the e-glove system grasping a baseball. Scale bar is 25 mm. (**b**) Results of the recording of pressure. (**c**) Change of conductance as a function of pressure applied for the embedded single sensor element. (**d**) The effects of different thickness of the skin layer, (**e**) The effects of varied environmental temperatures on the embedded pressure sensor, (**f**) Experimental results for the repeatability and reliability of the pressure sensor under cyclic loading at different levels of applied pressure.

Another important sensory function for replicating human hand-like perception is the ability to detect moisture and temperature[62]. Figure 3.5a provides an example for the use of the e-glove system to identify the dampness of a wet diaper by using an embedded capacitive hydration sensor positioned around the fingertip. Representative measurement results appear in Fig. 3.5b, indicating that an abrupt increase of the capacitance occurs when the e-glove touches a wet area of the diaper. A separate control measurement using a commercial moisture sensor (SEN-13322, SparkFun Electronics, Niwot, CO, USA) provides consistent results (Fig. 3.5c). The change in the capacitance over time for different levels of moisture appears in Fig. 3.6.

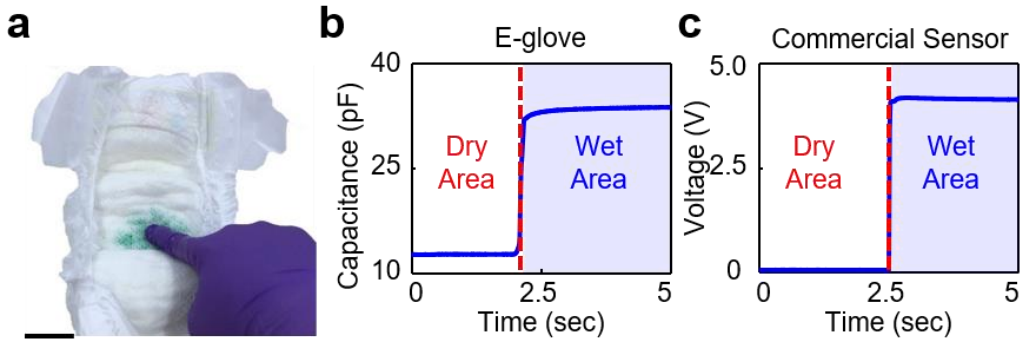

Figure 3.5. Demonstration of human hand-like moisture perception (**a**) Optical image of the e-glove system touching a wet diaper. Scale bar is 5 cm. (**b**) Results of the recording of hydration. (**c**) Results of control measurements by using a commercial hydration sensor.

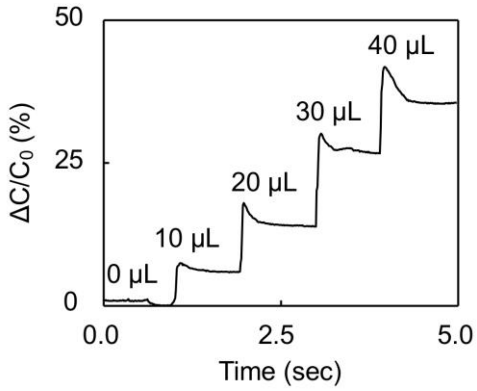

Figure 3.6. The graph showing the changes in capacitance of the moisture sensor over time for different levels of moisture.

The use of the e-glove system to detect the temperature on the surface of a cup containing hot water (~80 °C) appears in Fig. 3.7a. The embedded sensor positioned on the palm area contains a 4×4 array of temperature sensors made of Au (100 nm thick) and filamentary serpentine interconnectors (Au, 300 nm thick). Figure 3.7b presents the measurement results of the spatial temperature distribution when the e-glove system remains in contact with the cup. For a control comparison, real-time, simultaneous monitoring of the temperature occurs by using a commercial infrared (IR) camera (FLIR SC645, sensitivity: 0.05 °C) to confirm the surface temperature (Fig. 3.7c). In these demonstrations, the data measured are displayed on the screen of a control wristwatch unit (single point monitoring) and wirelessly transferred to an external reader such as a smartphone (multiple array monitoring), as appearing in Fig. 3.8. The corresponding power consumption and estimated operation time for these sensor elements are summarized in Table 3.2.

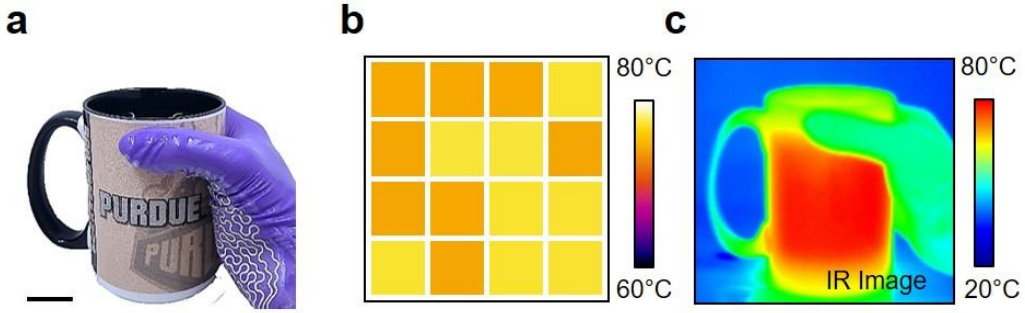

Figure 3.7. (**a**) Optical image of the e-glove system holding a cup of hot water. Scale bar is 5 cm. (**b**) Results of the recording of temperature. (**c**) An image of temperature measurement by using a commercial infrared (IR) thermal camera.

Another interesting aspect arises from the versatility of the e-glove system to provide extended capabilities beyond human sensory perception; i.e., to identify heart rates for on-demand access to health care and to monitor muscle fatigue during/after sport and exercise[75]. Fig. 3.9a shows an experimental demonstration that involves the use of the e-glove system for recording the electrical activities of the heart and muscles, such as ECGs and eEMGs, via the human skin. A separate prototype device consisting of an EP sensor on the outermost surface of the tip of the thumb is demonstrated by a using highly networked Ag nanowire-mesh (inset) patterned in a standard two-electrode configuration to serve as the EP electrodes. The use of a networked Ag nanowire-mesh offers useful features that enable high-fidelity coupling between the EP electrodes and the human

skin against various loading conditions such as stretching and scratching[76]. The measurement results in Fig. 3.9b demonstrate the high-level recording of ECGs (top) and EMGs (bottom) while the EP electrodes remain in direct contact on the chest and the forearm, respectively (Fig. 3.10). The ECGs and EMGs measured demonstrate clear detection of the P, Q, R, S, and T waves and electrical currents generated in the muscles during contraction (neuromuscular activities), respectively. These recordings are qualitatively comparable with those obtained using commercial EP recording electrodes (RedDotTM, 3 M, USA) (Fig. 3.9c). The details of the EP measurements appear in the materials and methods section of this chapter.

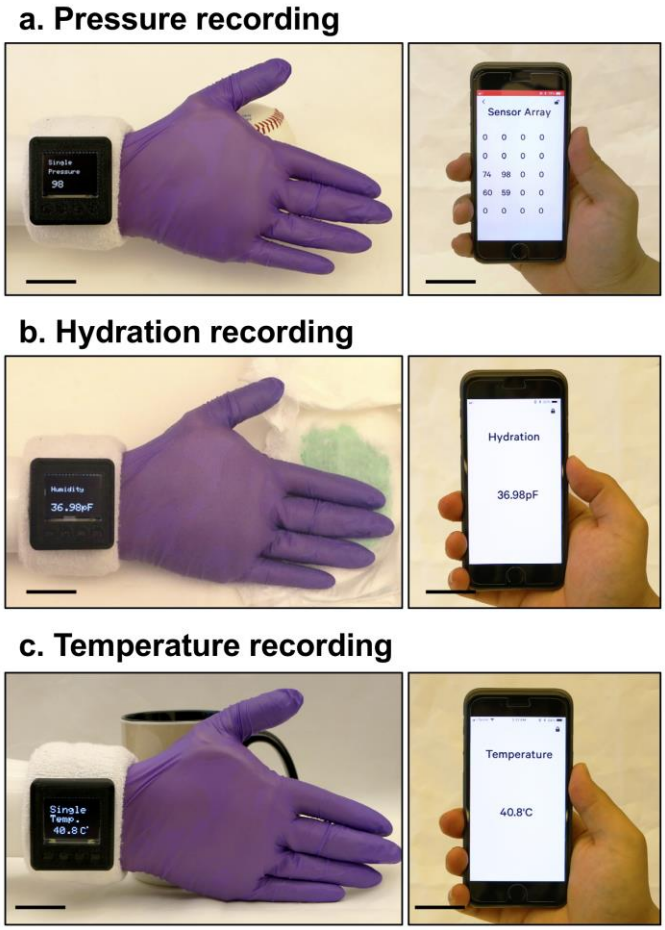

Figure 3.8. Optical images of the e-glove system demonstrating various functions with real-time measurements of pressure (**a**), moisture (**b**), and temperature (**c**). The measured data is displayed on the control wristwatch unit (left column) and wirelessly transmitted to a smartphone (right column). Scale bar is 3 cm.

Table 3.2. Summary of the power consumption and estimated operation time for the demonstrative sensors.

	Power consumption	Operating time with a battery (350 mAh)
Continuous displaying	75.2 mW	~15 hrs
On-demand displaying	15.76 mW	~71 hrs

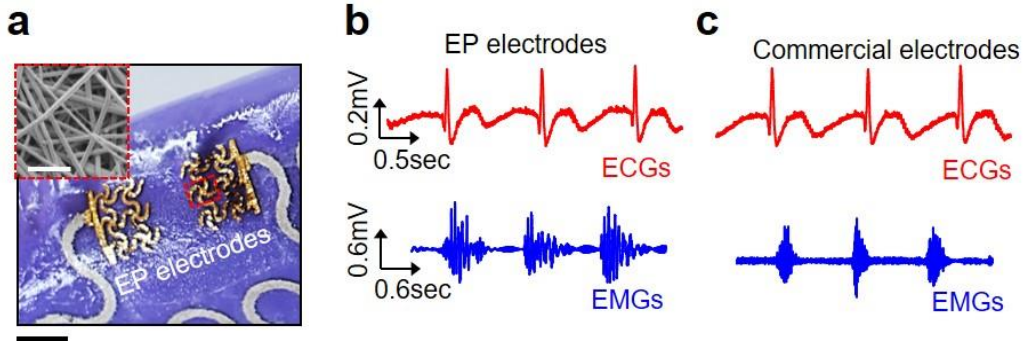

Figure 3.9. (**a**) Optical image of electrophysiological (EP) electrodes installed around the thumb of the e-glove system. The inset SEM image highlights the embedded networked Ag nanowire-mesh. Scale bars are 4 mm and 600 nm (inset), respectively. (**b**) ECG (top) and EMG (bottom) results measured from the human skin. (**c**) Control measurement results from commercial EP recording electrodes.

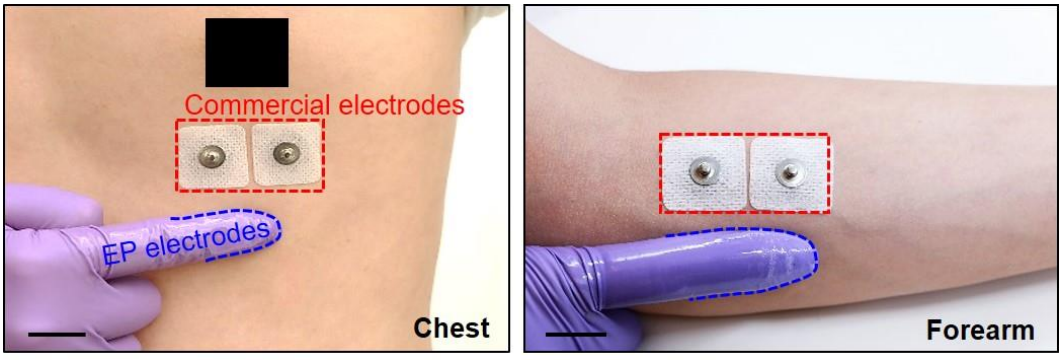

Figure 3.10. Optical images of the e-glove system in contact with the skin of the chest (Left) and forearm (Right) for the measurements of ECGs and EMGs, respectively. Scale bar is 2 cm.

3.3.3 Mechanical behaviors of replicating human skin-like properties

Human skin is elastic, flexible, and stretchable. Accordingly, the e-glove system demands the corresponding physical properties without any degradation in the performance of the embedded electronic materials. To achieve these physical properties, several strategies are used as follows: (1) the outermost skin layer of the e-glove system is comprised of a thin layer (~300 μm thick) of a silicone elastomer (Young's modulus (E) $\approx$ 0.5 MPa) that can provide softness and resilience similar to those of adult human skin[74], (2) the constituent materials of the e-glove system (e.g., a nitrile glove for the substrate, flexible Ag paste for interconnectors, and silicone elastomers for insulation/encapsulation) are flexible to accommodate mechanical loads during use and fitting, and (3) the filamentary serpentine traces incorporated along the electrical interconnectors provide the ability to mechanically isolate embedded semiflexible and rigid electronic components (e.g., capacitive hydration and temperature sensors) against stretching[77].

Figure 3.11a (top) shows a representative optical image of a unit filamentary serpentine trace of the flexible Ag paste on a nitrile glove under stretching at 40%, displaying no visible defects. The results of the finite element analysis (FEA) in Fig. 3.11a (bottom) reveal the maximum principal strains (ε~33%) of the constituent material (i.e., Ag paste). Representative images of the damaged units with different geometries after stretching beyond the fracture limit (50~100%) appear in Fig. 3.12. The corresponding FEA results under different stretching conditions and by using a testbed unit embedded with a rigid sensor element are summarized in Supplementary Fig. 3.13. The experimental and computational (FEA) results of the testbed unit under bending (Fig. 3.11b) and folding (Fig. 3.11c) produce consistent results. Figure 3.11d shows the measurement results of the relative resistance (R/R_0) of the testbed unit under stretching up to 40% (left), bending/folding (middle), and twisting up to 180° (right). The results confirm that the R/R_0 barely changes within less than ~5% for the mechanical deformations and then completely recovers when released. These results are consistent against repeated cycles of folding, while the R/R_0 increases up to ~2 and ~3 against 2000 cycles of stretching at 30 and 60% strains, respectively (Fig. 3.14).

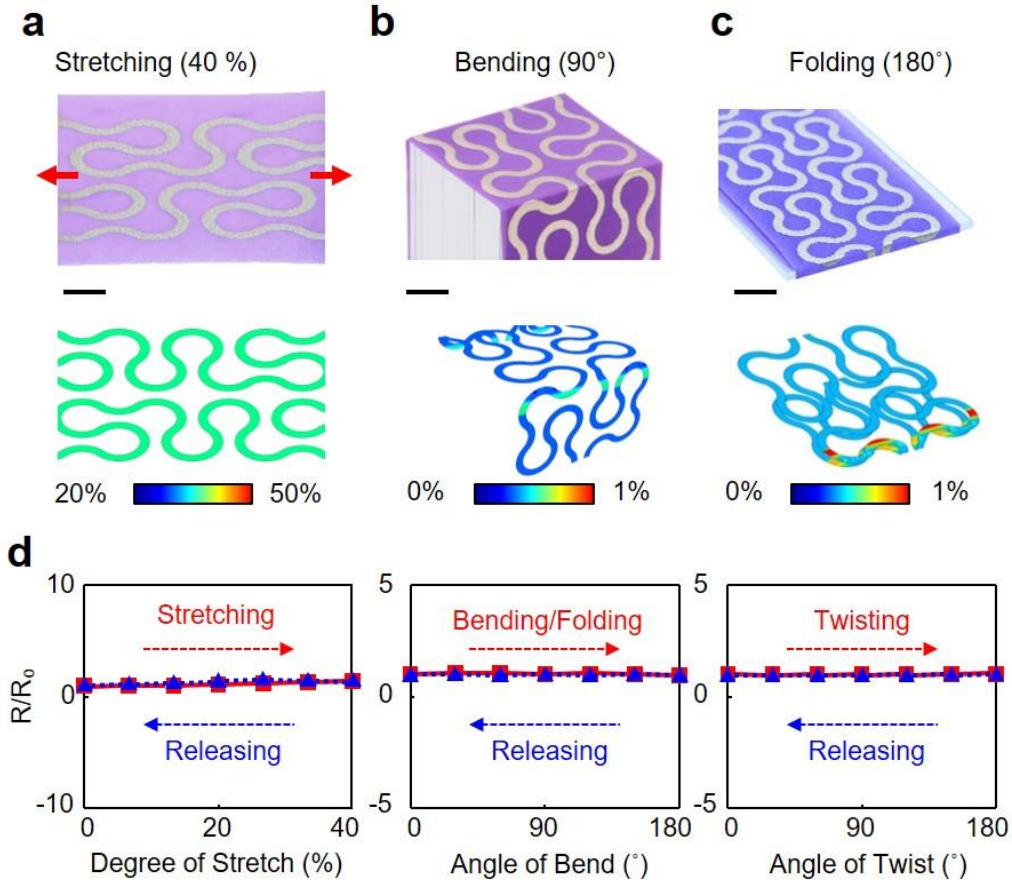

Figure 3.11. Mechanics of the conductive serpentine interconnects. (**a**) Experimental and finite element analysis (FEA) results for a representative testbed unit under stretching at 40 % strain. Scale bar is 7 mm. (**b**) Results for the testbed unit under bending at 90º. Scale bar is 5 mm. (**c**) Results for the testbed unit under folding at 180º. Scale bar is 6 mm. (**d**) Experimental data of normalized relative resistance (R/R_0) curves under stretching up to 40 % strain and release back to 0 % (left), bending to 180° and back to 0° (middle) and twisting to 180° and back to 0° (right).

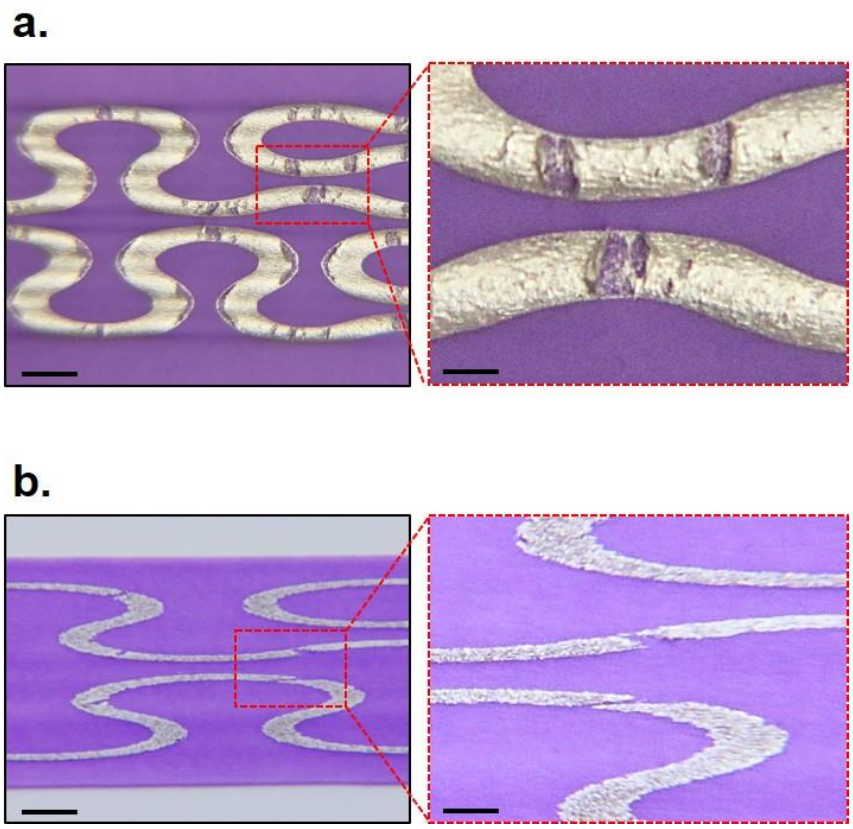

Figure 3.12. Representative optical images of the damaged Ag traces with different geometries under stretching beyond the fracture limit (50~100%). All scale bars are 3 mm (top, left), 1 mm (top, right), 2 mm (bottom, left) and 1 mm (bottom, right) respectively.

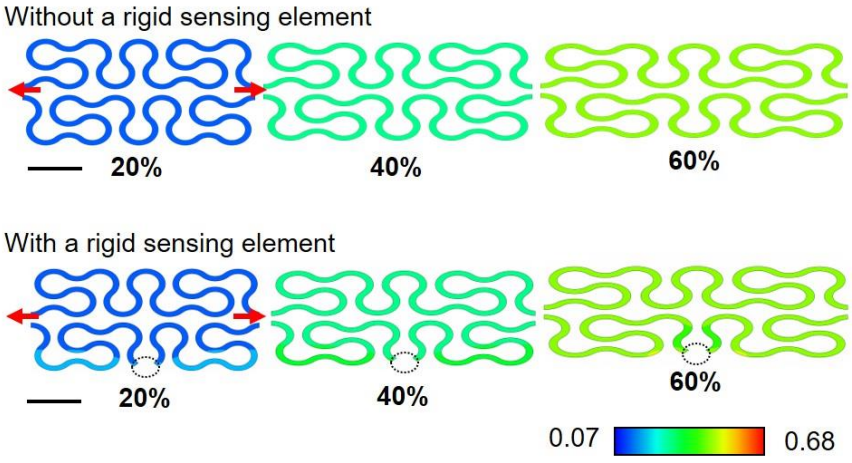

Figure 3.13. Computational (FEA) results of strain distributions of filamentary serpentine Ag interconnectors at 20 %, 40 %, and 60 % strains without and with a rigid sensor element. Scale bar is 4 mm.

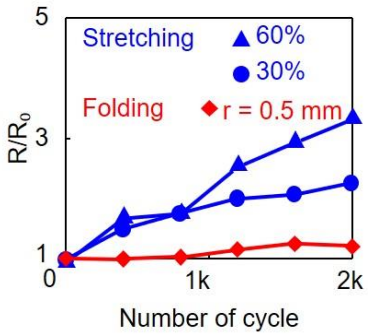

Figure 3.14. Measurement results of the relative resistance (R/R_0) of the testbed unit under repeated stretching (blue) up to 30 % and 60 % and folding (red) at r = 0.5 mm.

3.3.4 Demonstration of human hand-like appearance and warmth

Prosthetic hands with realistic human hand-like appearance and warmth can help users naturally integrate into social environments[60]. The outermost skin layer of the e-glove system can incorporate human skin tones, textures, artificial nails, and other features. Figure 3.15a shows representative examples of the e-glove systems colored with a range of commercial pigments (Slic Pig™, Flesh tone silicone pigment, Smooth-On, USA), wherein a detailed surface texture is obtained by exploiting a molding technique (see the Methods section for the details). Enlarged views of textured fingerprints (top) and an artificial nail (bottom) highlight the details of these features.

To replicate human hand-like warmth, a stretchable Joule-heating system is incorporated under the outermost skin layer of the e-glove system. The basic electronic components of this system include (1) serpentine resistive patterns of a flexible Ag paste for the Joule-heating element, which is stretchable up to ~40 % strain without any degradation in the performance (Fig. 3.15b), (2) a microcontroller unit that is capable of maintaining consistent temperature by exploiting the embedded proportional-integral-derivative (PID, P = 2, I = 5 and D = 0) (Fig. 3.15c), and (3) an automatic shutdown unit to eliminate potential overheating risk by which an immediate shutdown of the entire system occurs when any inadvertent incident of overheating beyond the preset limit (40 °C) is detected (Fig. 3.15d). The basic circuit configuration of the internal electronics appears in Fig. 3.16a, wherein a miniaturized p-i-n Si diode-based temperature sensor chip (RN142ZS, p-i-n diode, 0.6 mm × 0.3 mm, Rohm Semiconductor, Japan, sensitivity: ~2.24 mV/°C)

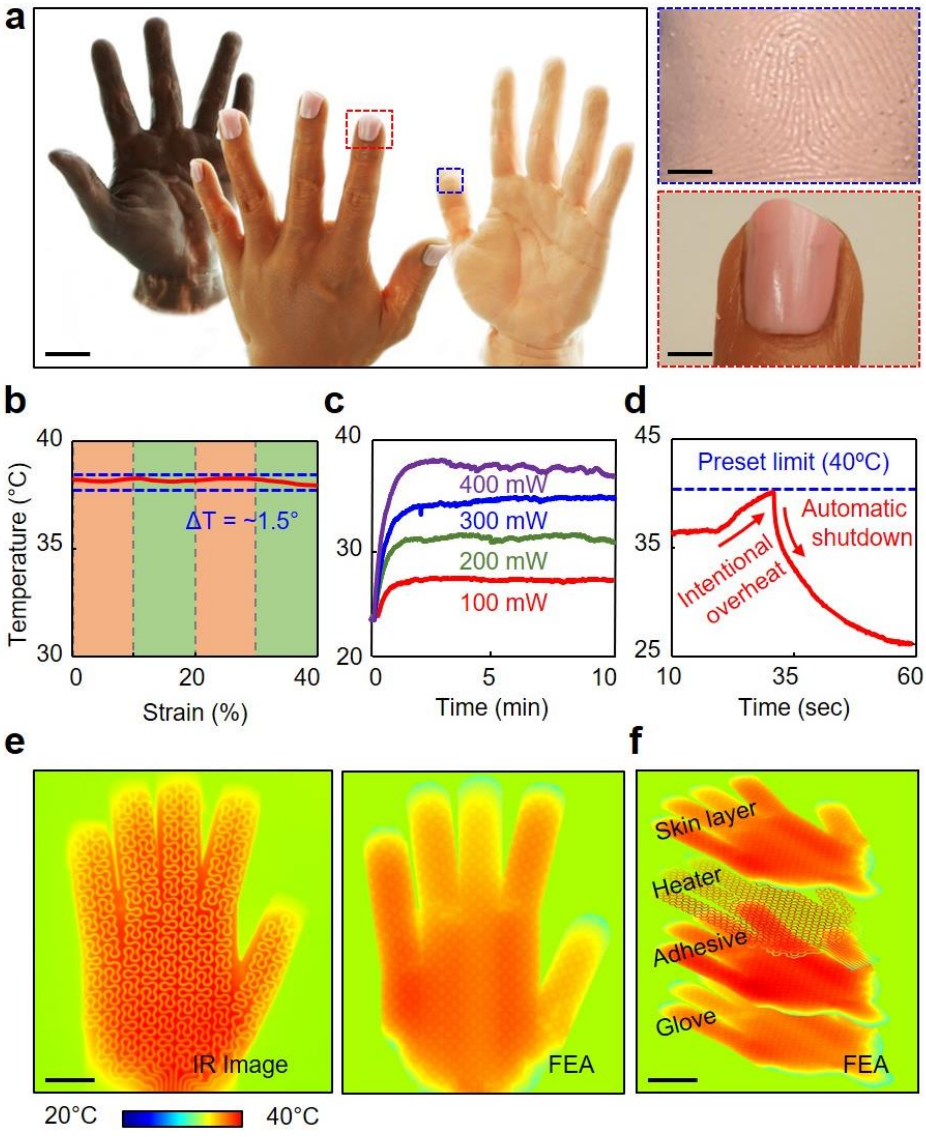

Figure 3.15. Demonstration of human hand-like appearance and warmth. (**a**) Optical image of the e-glove systems featured with several different skin tones, textures, and nails. The enlarged images highlight the detailed features. Scale bars are 2.5 cm (left), 5 mm (right top) and 6 mm (right bottom), respectively. (**b**) Temperature measured for the warmed skin of the e-glove system under stretching up to 40% strain. (**c**) Temperature measured over time by increasing the applied power from 100 mW to 400 mW. (**d**) Demonstration of the embedded automatic shutdown upon an intended incident of overheating beyond the preset temperature of 40ºC. (**e**) IR image (left) and FEA results (right) for the warmed skin of the e-glove system maintained at ~35ºC. Scale bar is 2.5 cm. (**f**) FEA results of the temperature distributions at several selected layers of the e-glove system. Scale bar is 3 cm.

is added to this shutdown unit to detect overheating events (Fig. 3.16b). In this scheme, the trigger of controlled heat (warmth) occurs by pushing a button on the control wristwatch unit in an on-demand manner whenever necessary (i.e., before shaking a hand), while the resistive-based temperature sensors at the center of the palm remain deactivated. Figure 3.15e shows the experimental (IR, left) and computational (FEA, right) results of the warmed e-glove system in which the skin temperature remains at a preset temperature of ~35 °C. The exploded view (Fig. 3.15f) of the FEA results reveals the temperature distribution of several selected layers of the e-glove system, implying that the prosthetic hand experiences similar or slightly lower temperature than that of the outer skin layer (~35 °C) due to reduction of the temperature through the adhesive layer (i.e., the epoxy) and the substrate (i.e., the nitrile glove), which have low thermal conductivities of 0.1 and 0.24 W/mK, respectively.

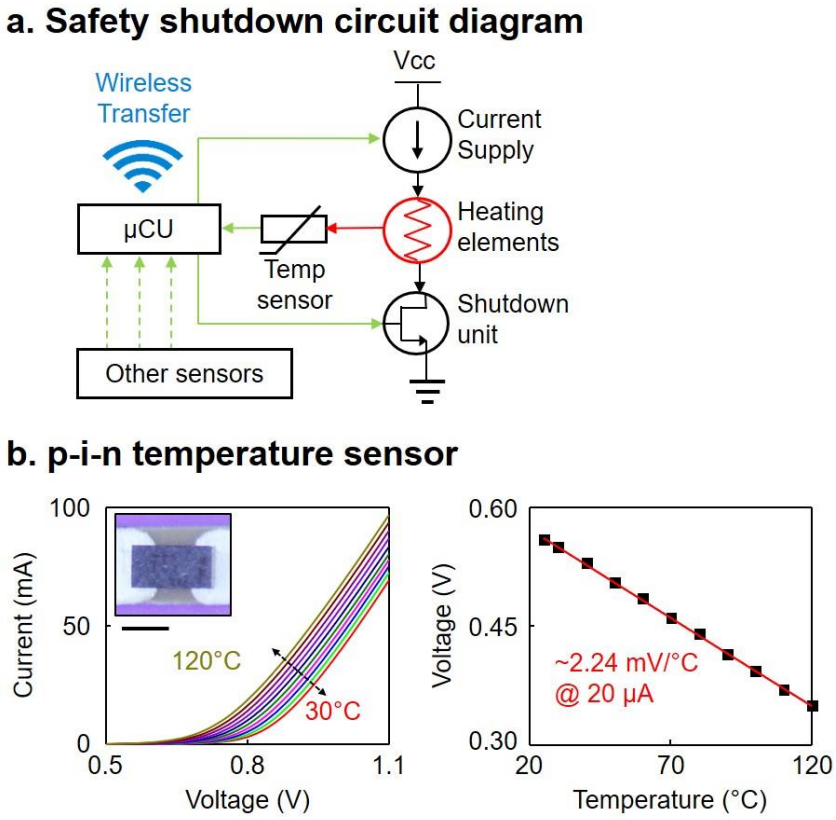

Figure 3.16. (**a**) Basic circuit configuration of the internal electronics for the human hand-like skin layer of the e-glove system, (**b**) Calibration curves of the embedded p-i-n Si diode-based temperature sensor.

3.3.5 Assessment of prosthetic hand-human interaction scenarios

Experimental demonstrations of the e-glove systems in interactions with human subjects provide assessments of how well the systems replicate the details of a real human hand; a close resemblance to a real hand can enhance the confidence and ability of the prosthetic hand user in many social interactions. Figure 3.17a presents a within-subjects experimental design that includes four different prototypes featured with human hand-like softness and skin tone (A), along with textures (B), warmth (C), and texture and warmth (D), all deployed in a randomized sequence to eliminate learning bias. A total of 32 subjects, including 24 males and eight females, with an average age of 30 were recruited for this study. Seventeen of the subjects had seen or interacted with the prosthetic hand before the tests. The subjects were asked to interact with each of the prototypes sequentially by touching, poking, scratching/rubbing, and handshaking gently or firmly (Fig. 3.17b). Subsequently, the subjects were asked to complete a questionnaire consisting of 12 questions totaling 60 points with ratings on a scale from 1 (low) to 5 (high) to evaluate the comfort, warmth, convenience, and human-like feeling after every interaction (Fig. 3.18), and finally, rank the prototypes in a comparative evaluation. The average duration of a subject study was ~40 min, and no skin irritations or adverse effects to the subjects' hands were observed throughout the studies.

Figure 3.17c presents the results of one-way repeated measures analysis of variance (ANOVA) test[78], indicating a substantial difference ($F(3,93) = 17.94$, $p < 0.00001$) at $p \leq 0.05$ in the subjects' preference to the e-glove prototypes with human hand-like features. Mauchly's test for sphericity ($X^2(5) = 2.79$, $p = 0.73$) confirms that no violation on the sphericity (univariate) assumption exists[79]. The results of post hoc tests using the two-tailed paired samples t-test on the dependent means[80] reveal that prototypes B–D with at least one human hand-like feature (either texture, warmth or both) yield significantly higher rating scores compared with the counterpart (A–B: $t(31) = 4.99$, $p < 0.00005$; A–C: $t(31) = 3.19$, $p < 0.00324$; A–D: $t(31) = 6.21$, $p < 0.00001$). While there is no significant difference between prototypes B and D ($t(31) = 1.53$, $p = 0.13638$), there are significant differences between B and C ($t(31) = -2.40$, $p = 0.02246$) and D and C ($t(31) = 4.16$, $p = 0.00024$). The corresponding summary table appears in Table 2.3. The results appearing in Fig. 3.17d and e support that prototype D is the most preferred (ranked) while prototype C is not preferred over prototypes B and D.

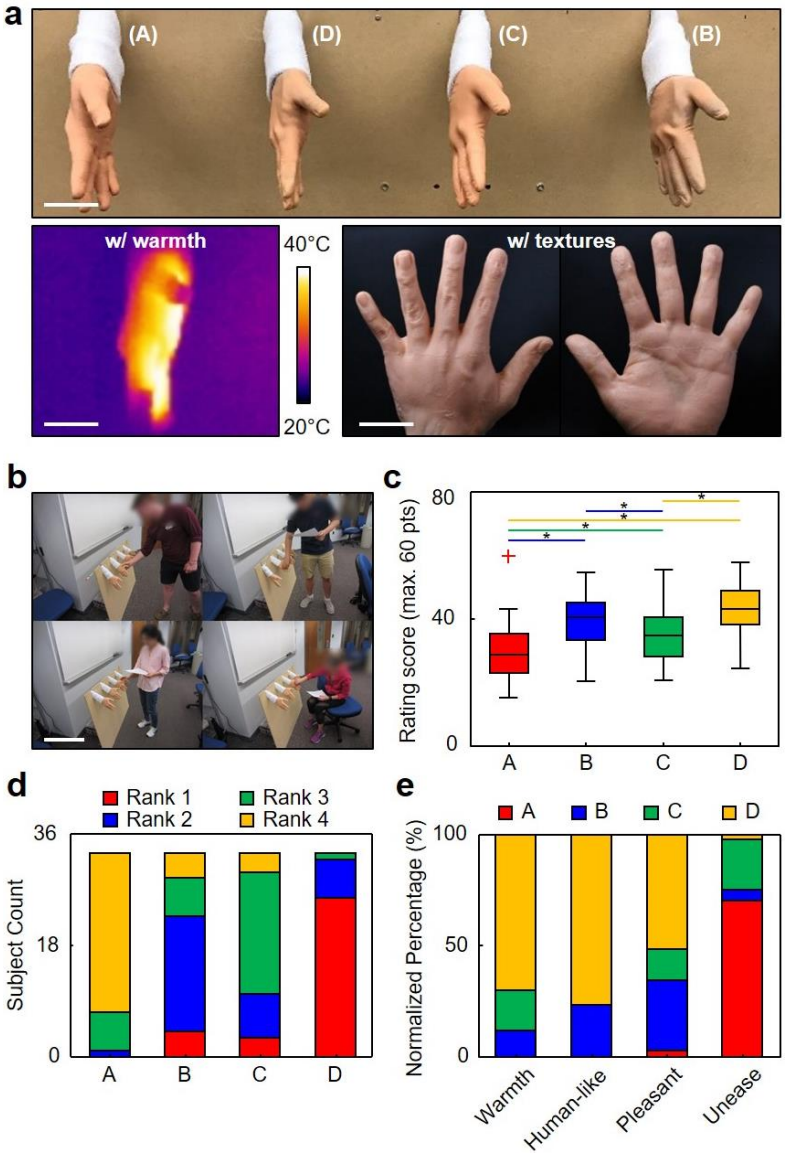

Figure 3.17. Assessment of prosthetic hand-human interaction scenarios. (**a**) Optical image (top frame) of the experimental setup for the four different prototypes. The IR and optical images (bottom frame) show the human hand-like warmed and textured e-glove prototypes, respectively. Scale bars are 7 cm (top), 6 cm (left bottom), and 5 cm (right bottom), respectively. (**b**) Optical images of the participants interacting with the prototypes. Scale bar is 60 cm. (**c**) Statistical analysis results of the subject rating score, one-way ANOVA with two-tailed paired sample t-test post hoc test in the human-hand interaction study. (**d**) Results of subject responses on the prototypes A-D, ranked from 1 (best) to 4 (worst). (**e**) Results of the subject ranking of the prototypes as normalized percentages of the categories of warmth, human-like, pleasant, and unease.

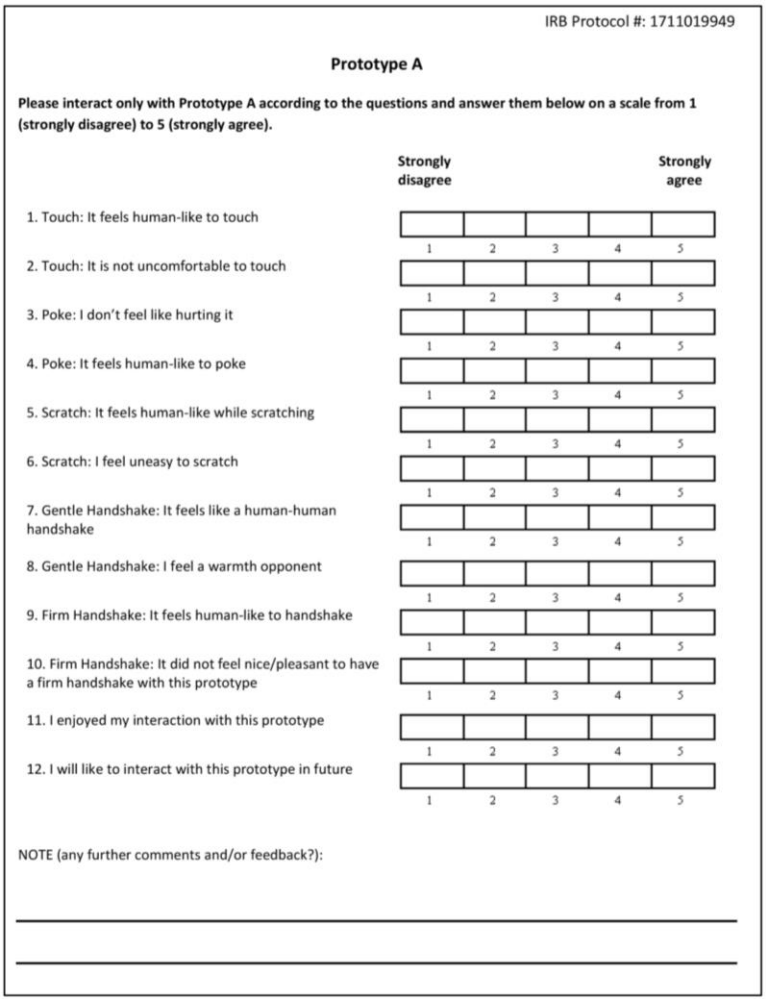

IRB Protocol #: 1711019949

Prototype A

Please interact only with Prototype A according to the questions and answer them below on a scale from 1 (strongly disagree) to 5 (strongly agree).

	Strongly disagree				Strongly agree
1. Touch: It feels human-like to touch	1	2	3	4	5
2. Touch: It is not uncomfortable to touch	1	2	3	4	5
3. Poke: I don't feel like hurting it	1	2	3	4	5
4. Poke: It feels human-like to poke	1	2	3	4	5
5. Scratch: It feels human-like while scratching	1	2	3	4	5
6. Scratch: I feel uneasy to scratch	1	2	3	4	5
7. Gentle Handshake: It feels like a human-human handshake	1	2	3	4	5
8. Gentle Handshake: I feel a warmth opponent	1	2	3	4	5
9. Firm Handshake: It feels human-like to handshake	1	2	3	4	5
10. Firm Handshake: It did not feel nice/pleasant to have a firm handshake with this prototype	1	2	3	4	5
11. I enjoyed my interaction with this prototype	1	2	3	4	5
12. I will like to interact with this prototype in future	1	2	3	4	5

NOTE (any further comments and/or feedback?):

Figure 3.18. An example of the human subject study questionnaire for assessment in prosthetic hand-human interaction scenarios. Note, questions 6 and 10 had inverted scores.

Table 3.3. Summary of subject rating scores along with statistical results, and rankings on each category in prosthetic hand-human interaction study.

	Prototype A	Prototype B	Prototype C	Prototype D
Rating scores - max. 60 points				
Mean	29.09	39.09	34.63	41.72
Std. Deviation	9.22	7.99	9.08	8.05
One-way (repeated measures) ANOVA				
Results	$F(3,93) = 17.94$, $p < 0.00001$, Sig. diff. found at $p \leq 0.05$			
Post hoc tests				
Prototypes Pair	t(31)	p	Sig. diff. found at $p \leq 0.05$?	Best Prototype
A-B	4.99	< 0.00005	Yes	B
A-C	3.19	= 0.00324	Yes	C
A-D	6.21	< 0.00001	Yes	D
B-C	-2.40	= 0.02246	Yes	B
B-D	1.53	= 0.13638	No	-
C-D	4.16	= 0.00024	Yes	D
Rankings (with normalized percentage, if available)				
Overall	4	2	3	1
Most warmth	-	3 (12.12%)	2 (18.18%)	1 (69.7%)
Most pleasant and comfortable	4 (3.03%)	2 (31.31%)	3 (14.14%)	1 (51.52%)
Most human-like skin and feel	-	2 (22.44%)	-	1 (76.56%)
Most unease	1 (70%)	3 (5%)	2 (22.5%)	4 (2.5%)

3.4 Discussion

The results presented here demonstrate that various electronic circuits and sensors can be printed on a commercial stretchable nitrile glove that already possesses the desired ergonomic design, allowing for seamless integration with arbitrary hand shapes. This integration has been challenging using conventional approaches that typically involve the use of multiple flexible sensors wrapped around prosthetic hands to accommodate the geometric complexity of the hand shape[62]. The user interface via a wristwatch unit provides the advantages of the capability for real-time display of the sensory data measured on a control wristwatch unit, remote data transmission to an external reader for data postprocessing, providing benefits and convenience to the user, and a multisensory feedback/display in one device (e.g., temperature, pressure, and humidity sensing two-dimensional data of the whole palm). Adding additional sensory cues through audio and tactile/vibrational feedback to further improve the user interface would be interesting[81]. The realistic human hand-like features of the e-glove system offer an expanded set of options for the daily activities of prosthetic hand users, with the potential to improve their mental health and well-being by helping the user more naturally integrate into social contexts. Although this study focuses on applications for general passive prosthetic hands, the results also suggest opportunities in the integration of the e-glove system with the recently emerging cutting-edge active prosthetic hands controlled by the mind, voice, and/or muscles of the user[82-85]. The hybrid printing method for the fabrication of the e-glove system is cost-effective and compatible with various electronic materials and sophisticated design layouts, thereby foreshadowing the implications for a wide range of users; further development of an e-glove system that can fit the hand of a small child or an extra-large adult is also important. Finally, the application of the established e-glove platform can also be extended to smart gloves for assistive robotic hands, automotive factory workers, and home-based rehabilitations[86].

3.5 Acknowledgements

The figures, results and manuscript in this chapter is reprinted/adapted with permission from "Soft-packaged sensory glove system for human-like natural interaction and control of prosthetic hands" *NPG Asia Materials* **11**, 43. Copyright 2019 Springer Nature. I express sincere gratitude to all of the coauthors on this journal publication, Dr. Ramviyas Nattanmai Parasuraman (Purdue

University), Liu Wang (University of Texas at Austin), Yeonsoo Park (Purdue University), Bongjoong Kim (Purdue University), Seung Jun Lee (Purdue University), Prof. Nanshu Lu (University of Texas at Austin), Prof. Byung-Cheol Min (Purdue University), and Prof. Chi Hwan Lee (Purdue University).

4. SOFT HANDLING OF DELICATE BIOMATERIALS AND BIOELECTRONICS

4.1 Introduction

In the past decade, there have been great achievements in constructing high-performing complex architecture of thin biological and electronic materials. For example, single layer cell sheets have observed to replicate the physiological activities of the original tissue and show improved therapeutic effects compared to individual cells because of increased interaction between cell to cell within the extracellular matrix[87-90]. There is a great focus on studying these cell sheets to construct an in vitro disease models which can lead to treatment of damaged or defective tissues and even on to the organ level. Independently, reducing the thickness of electronics devices allow conformal adhesion to the target minimizing the interfacial gap, in turn, enhances device performance for sensing and eventually leading to better diagnosis, and therapeutic treatments[9,91-93]. However, manipulation of thin and delicate materials for transport and assembly without causing damage still remains as grand obstacle. External forces which are applied during gripping, holding, and unloading such soft and delicate materials often causes deformations, wrinkles, or damages[94]. In previous studies, such handicap was avoided by utilizing thin sacrificial polymeric materials like water-soluble or thermal release tapes as a support during the manipulation and handling[71,95 96]. However, such support structures must be removed chemically or by applying long-lasting heat after the thin materials were placement of onto a target site, thus making them not feasible in many situations.

Recent efforts have developed methods to handle thin electronic materials by replicating the actions of cephalopods (e.g., octopus and squid) to capture and release their preys[97-99]. Cephalopods use multitude of muscle actuated suction cups (suckers), on limbs to make conformal adhesion to the target in both wet and dry environments[100,101]. The suction cups are controlled by the bioelectrical signals which causes rapid contraction and relaxation of the muscle. This results

in changes of the internal pressure within the suckers once they are attached. However, many of the material-handling systems studies tried to mimic the force of the suction cups by duplicating the anatomical structure but fails to incorporate the on-demand control via bioelectrical signal for the suction cups. As a result, such studies require external mechanical force to attach and detach target materials. Synthetic suction cups fabricated with polydimethylsiloxane (PDMS) or polyurethane acrylates demonstrate high rigidity compared to the natural suction cup counterpart by 2-3 orders of magnitude[97,99]. Controlling such rigid suction cups require even greater forces when compared to the naturally occurring biological suction cups which can lead to increased probability of damaging the delicate target materials. There were efforts to construct a device which can pick up and unload materials by heat with a coating of porous PDMS mixed with thermally activated poly(N-isopropyl acrylamide) (PNIPAAm)[98]. However, the process was only capable wet conditions, submerged in water. However, the device required 30 min to hours to transport one material.

4.2 Materials and Methods

4.2.1 Preparation of the microchanneled PNIPAAm gel

NIPAAm (1.25 g) and N,N′-methylenebisacrylamide (12.5 mg [0.01 weight % (wt %) of NIPAAm]) were dissolved in distilled water (8.75 ml) for 1 day at 25°C to ensure the complete dissolution. Then, 25 mg (0.5 wt % of NIPAAm) of radical photo-initiator (Irgacure 2959) was added into the obtained solution and stirred until all the solids completely dissolved. The resulting pregelled NIPAAm solution was poured onto a Si-wafer substrate (4 inches, 550 μm thick) with silicone mold (50 mm by 50 mm by 1 mm or 20 mm by 20 mm by 10 mm). Then, the Si-wafer substrate was put on a liquid nitrogen reservoir for the directional crystallization of the pregelled NIPAAm solution. The distance between the bottom surface of the Si-wafer and the top surface of liquid nitrogen was 1 cm. After complete crystallization of the pregelled NIPAAm solution, the samples were irradiated with a UV lamp ($\lambda = 365$ nm) for 6 hours at a −25°C freezer for the radical cryo-polymerization. The as-prepared poly-NIPAAm gel (PNIPAAm) was then washed with fresh water three times to remove the ice crystals. For comparison, PNIPAAm gel with randomly oriented microchannels was prepared by placing the pregelled NIPAAm solution in a freezer at −25°C for random crystallization. Then, the resultant samples were cryo-polymerized and washed

at the same condition described above. PNIPAAm gel free of microchannels was prepared by skipping the crystallization and subsequently irradiated with a UV lamp for 1 hour at 4°C. All hydrogel samples were soaked in 250-ml distilled water at 25°C, which was repeatedly replaced for 1 day to remove unreacted impurities before using them.

4.2.2 Characterization of PNIPAAm gel

The morphology of microchanneled PNIPAAm gels was examined using an environmental scanning electron microscope (ESEM; Quanta FEG 450, FEI) and microcomputed tomography (micro-CT, MicroXCT-200, Xradia Inc.). For cross-sectional analysis, the samples were immersed in liquid nitrogen for 30 min and immediately cryo-fractured. One hundred points from 10 different ESEM images were taken to determine the average pore size. The porosity of gels was determined by the gravimetric method. The pore volume of gels was divided by the total volume of gels as:

$$Porosity(\%) = \left\{\frac{W_{Swollen} - W_{Dry}}{\rho_W}\right\} / \left\{\frac{W_{Swollen} - W_{Dry}}{\rho_W} + \frac{W_{Dry}}{\rho_{PNIPAAm}}\right\}$$

where W_{swollen} and W_{dry} are the weights of swollen and dry gels, respectively; ρ_{w} is the water density; and ρ_{PNIPAAm} is the NIPAAm density (1.1 g/cm3). For the ESR measurement, the weight of PNIPAAm gels at different temperatures (4° to 40°C) was measured with 4°C increments. The ESR was defined as the following:

$$ESR(\%) = \{(W_s - W_d)/W_d\} \cdot 100$$

The hydrogel samples were equilibrated at each temperature for 12 hours and weighted (W_{s}) after removing excess water. The dry weight of the samples (W_{d}) was measured after lyophilization. Five samples of each PNIPAAm gel were averaged. For dynamic deformation analysis of hydrogels in response to temperature change, hydrogel samples immersed in 25°C were trimmed into a cylinder shape (d = 25 mm, t = 1 mm) and placed on a copper plate (t = 1 mm). Then, the plate was put onto a heated Peltier stage (40 °C) to investigate the deswelling kinetics of samples. For reswelling kinetics, deswelled samples were transferred to a cooled Peltier stage (25 °C). The volume change in response to temperature was monitored using an optical microscope that

connected with the Peltier device (TP104SC-mK2000A, Instec). All optical images were analyzed using ImageJ software. The compressive modulus of hydrogels was measured on an electronic universal testing machine (Instron 5943, Instron) equipped with a water bath. Samples were cut into a square shape (10 mm by 10 mm by 10 mm). All mechanical tests were conducted in a water bath (25 °C). There were five replicates for all mechanical tests.

4.2.3 Preparation of the flexible joule heater

The heater was fabricated on a copper/polyimide film (t = 9 μm/12 μm, Pyralux AC091200EV, Dupont). A standard photolithographic patterning with a dry film photoresist (Riston MM540, Dupont) followed by the wet etching method (CE-100, Transene Inc.) defined the copper layer into a joule heating element. The copper traces were coated with 1 μm thick layer of tin (Sn) (421 Liquid Tin, MG Chemicals) to protect the copper from oxidation in elevated temperatures within a humid environment. The resulting heater was then connected to an external power supply, where a voltage range of 2 to 5 V and its thermal characterizations over time were recorded using an infrared camera (E40, FLIR Systems).

4.2.4 Fabrication of the soft manipulator

The cyanoacrylate-based adhesive was spread on top of the flexible heating array[102]. Immediately after, the hydrogel was trimmed into a cylinder shape (d = 25 mm, t = 1 mm) and pressed onto the substrate. The bonding occurs within 30 seconds. The resulting gel/heater was attached to a 3D printed supporter using double-sided tape (VHB, 3M). Then, the soft manipulator was connected to an electrical power supply.

4.2.5 Characterization of the soft manipulator

For dynamic deformation analysis of the soft manipulator in response to activation of a heater, a monochrome camera (DS-Qi2, Nikon) was attached to an optical microscope (Eclipse LV100, Nikon) for top-view analysis of the gel in the soft manipulator. A digital camera with an optical zoom macro lens (Canon, MP-E 65 mm) was used for the side view analysis of the soft manipulator. Gels in the soft manipulator were incubated with colored water (Green, McCormick) for visualization of water. Adhesion tests were performed with a DMA (ESM303, Mark-10). The

soft manipulator was mounted on a load cell of the DMA (M5-5 or M5-200, Mark-10), and the vertical approach and retraction speeds of the soft manipulator were 0.1 mm/s. Force-displacement profiles with time were measured at room temperature.

To examine the capability of the soft manipulator to handling materials with different elastic moduli, alginate hydrogels with elastic moduli of 23 and 70 kPa were used in this study. Pregelled alginate solution was prepared by mixing 2 wt % alginate solution in MES buffer (pH 6.5) with sulfonated N-hydroxysuccinimide and 1-ethyl-3-(3-dimethylaminopropyl) carbodiimide. Then, the pregelled alginate solution was cross-linked by adding adipic acid dihydrazide (AAD). The elastic modulus of the alginate gels was controlled by varying the molar ratio between AAD and uronic acids of alginate (M_{AAD}). Cross-sectional fluorescence images were obtained from 3D z-stack confocal images (LSM 880, Carl Zeiss). The Rhodamine B was mixed with water for tracking of water inside the soft manipulator before and after the attachment process. To investigate surface contamination of the soft manipulator, an adhesion tests to silicon wafers was performed using either the soft manipulator or a commercial medical grade tape (Transpore, 3M). After detachment of the samples, the resulting wafer was incubated with a dye (Rhodamine B) for 30 min. All samples were washed with distilled water three times in total. Then, the wafer surface was dried using N_2 gas and subsequently observed the wafer surfaces using fluorescent optical microscopy.

4.2.6 Preparation of stem cell sheets

C2C12 cells (mouse skeletal myoblast cell line, CRL1772) and D1 cells (bone marrow–derived mesenchymal stem cell line, CRL12424) were obtained from the American Type Culture Collection (ATCC). C2C12 or D1 cells were plated on temperature-responsive PNIPAAm-grafted culture dishes (d = 35 mm, UpCell, Thermo Fisher Scientific) with seeding density of 5×10^5 cells. The cells were then cultivated for 3 days according to the guidelines of ATCC. To harvest sheets, confluent cells were rinsed twice with warmed Dulbecco's phosphate-buffered saline (DPBS). Then, the monolayers were detached from the culture dish by lowering the incubation temperature from 37 ° to 20 °C.

4.2.7 Analysis of cell sheets after transport using the soft manipulator

The viability of cell sheets was examined using the LIVE/DEAD Viability/Cytotoxicity Assay Kit for mammalian cells (Invitrogen) according to the manufacturer's instructions. The cultured cells or transferred cells were gently washed three times with DPBS. Calcein acetoxymethyl (AM) and ethidium homodimer-1 (EthD-1) were diluted together in DPBS. Diluted calcein AM and EthD-1 solution (1 ml) was added to cultured cells and kept for 45 min at room temperature. The live cells were stained with calcein AM, and dead cells were stained with EthD-1. After staining, cells were gently washed with 1× DPBS for three times and imaged with a fluorescence microscope (LSM-880, Carl Zeiss). Off-axis deformation of the cell sheets before and after the delivery process was quantified using SLIM. The optical system was assembled by attaching a SLIM module (CellVista SLIM Pro, Phi Optics) to the output port of an existing inverted phase-contrast microscope[103].

4.2.8 Assembly of a multilayered cell sheet using the soft manipulator

C2C12 cells were cultured onto a temperature-responsive culture dish to produce cell sheets as described above. After incubation, confluent cells were stained with Cell Tracker Orange CMRA (Invitrogen) or calcein AM (Invitrogen). Then, cell sheets were detached from the culture dish by lowering the incubation temperature from 37 ° to 20 °C. The detached cell sheets were captured and transferred using the soft manipulator with electrical heater control. A multilayered cell sheet was fabricated by repeating the transfer procedure. The resulting multilayered tissue structure was imaged using a fluorescence microscope (LSM-880, Carl Zeiss).

4.2.9 Transplant of a stem cell sheet onto the anterior surface of the cornea

Long-Evans/BluGill rats were used in this study. All experimental protocols followed the National Institutes of Health Public Health Service Policy on Humane Care and Use of Laboratory Animals and were approved by the University of Illinois at Urbana-Champaign (UIUC) Institutional Animal Care and Use Committee. For fixation of the cornea, the perfusion needle was inserted into the left ventricle of the heart. A cut was made within the right atrium to allow blood evacuation. Saline was injected at a rate of 300 ml/min to clear the blood from the rat, followed by injection of paraformaldehyde (PFA) at 300 ml/min. The perfusion was confirmed by checking

PFA dripping from the nose of the rate, stiffening of the extremities and the liver, and contractures of the musculature. After completing the perfusion, the stem cell sheet was placed on the rat's cornea using the soft manipulator. The other rat eye was used as a control. Enucleation was then performed using micro-scissors.

4.2.10 Immunohistochemistry and imaging of the transplanted stem cell sheet

Enucleation was followed by placement of the eyeball on dry ice then into a mold. The mold was subsequently filled with an optimal cutting temperature (OCT) compound–embedding medium to ensure OCT. Cryosectioning at 40 μm slices was performed using a cryostat. Slices were then fixed using 4% PFA because the eyeball was fixed but not the stem cell sheet. The sample was washed three times in tris-buffered saline (TBS) for 5 min. The section was stained with hematoxylin and eosin staining, followed by dehydration in citrasol for 5 min. The stained tissue section was imaged using Axio Zoom V16.

4.2.11 Fabrication of the EP sensor and the evaluation using the soft manipulator.

The fabrication of the EP sensor began by spin-coating a layer of poly(methyl methacrylate) (PMMA; ~1 μm thick) on a glass substrate, followed by thermal annealing at 180 °C for 1 min. A subsequent layer of polyimide (~1 μm thick) was coated and cured in a vacuum oven at 250 °C for 1 hour. Thin films of Cr and Au (t = 5 nm/150 nm thick) were deposited by using an electron beam evaporation. Photolithographic patterning using a negative-type photoresist (Riston MM540, DuPont) followed by wet etching with Au and Cr etchants (Transene) defined the joule-heating element. The resulting structure was submerged in acetone to dissolve the bottom PMMA layer. An anisotropic conductive film cable (ACF; HST-9805-210, Elform) was bonded to the terminals and was connected to an external data acquisition system. The measurement of ECG signals began by attaching two commercial conducting electrodes (30 mm × 24 mm, H124SG, Kendall) diagonally across the pig heart. The electrodes were then connected to an arbitrary waveform generator (3390, Keithley) to apply a preprogrammed cardiac waveform (1 Hz frequency, 50 mV amplitude). The EP sensor was transferred onto the surface of the pig heart with the soft manipulator. The sensor was connected to an external preamplifier (Octal Bio Amp,

ADInstruments) and data acquisition unit (PowerLab 16/35, ADInstruments), where the captured ECG signal was digitally filtered with a band-pass filter at the bandwidth of 0.5 ~ 100 Hz.

4.3 Results

4.3.1 Design of the electrothermal soft manipulator for delicate material transport

Figure 4.1a is a schematic representation which demonstrates a soft manipulator capable of repeat the holding and unloading of thin and delicate materials responding within 10 s of an electrical signal. It was hypothesized that a rapid thermo-responsive, microchanneled hydrogel layered with a joule heater would lift and release target materials without applying excessive external force due to temperature-induced internal pressure change within microchannels of the gel (Fig. 4.1b). In addition, the gel is tailored to be as soft as biological suction cups and it would allow fast and notable changes in internal pressure in response to small temperature changes while minimizing the amount of force applied onto the thin material to be transported. This hypothesis was examined by attaching a flexible electric heater, which converts electrical signals into heat, to a microchanneled PNIPAAm hydrogel. It was observed that the extent that the electrothermal signal controls the shrinkage and expansion of microchannels of the gel along with subsequent pressure change inside microchannels. The resulting soft manipulator was examined for its ability to pick up and release thin and delicate materials onto target sights promptly in response to the electrothermal control signal. These thin and delicate materials can include therapeutic stem cell sheets and ultrathin wearable bioelectronic devices.

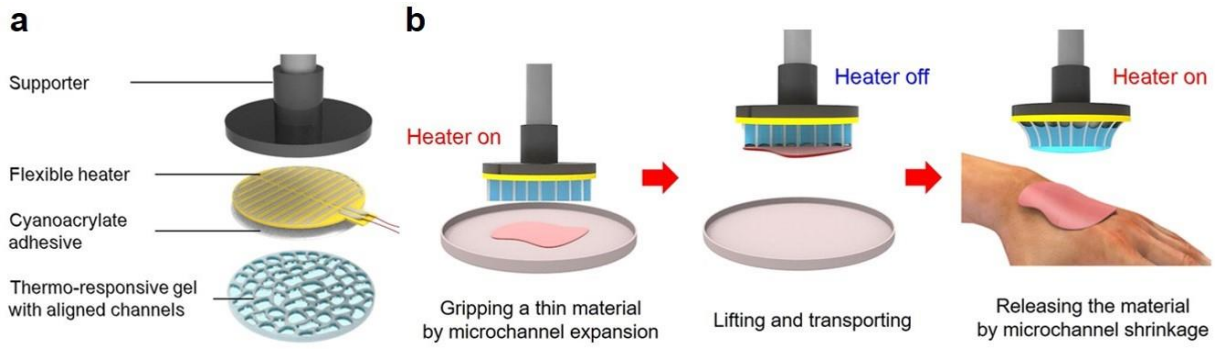

Figure 4.1. Schematic illustration of the soft, electrothermally controlled manipulator and the process to transport a thin material using the soft manipulator. (**a**) The soft manipulator consists of a supporter, flexible heater, cyanoacrylate adhesive, and a thermo-responsive PNIPAAm hydrogel with aligned microchannels. (**b**) The process to transport materials of interests using the soft manipulator. (1) The soft manipulator is lowered for the gel to contact the target therapeutic cell sheet or an ultrathin film device. The heater is activated to contract microchannels of the gel. (2) The heater is turned off to open microchannels of the gel and generate negative pressure within the microchannels. As a result, the gel holds, lift up, and transport the target. (3) The heater is turned on to close microchannels and generate positive pressure in the microchannels. The positive pressure serves to release the thin material onto the target surface.

4.3.2 Fabrication and analysis of rapid temperature-responsive gel

The hydrogel that undergoes a rapid volumetric change in response to a temperature change was prepared by introducing anisotropically aligned microchannels into the PNIPAAm gel. The microchanneled gel was assembled by placing the pregelled NIPAAm solution on top of a liquid nitrogen reservoir. Then, ice crystals nucleated from the bottom and grew to the top surface due to the temperature gradient (step 1 in Fig. 4.2a). Simultaneously, solutes, including NIPAAm monomer, cross-linker, and photo-initiator in the solution, were separated from the growing ice crystals because of the decreased solubility in ice crystals (step 2 in Fig. 4.2a). This continuous and directional segregation of the solutes formed a cryo-concentrated phase between growing ice crystals. Subsequent exposure of the frozen sample to ultraviolet (UV) light–activated polymerization and cross-linking reaction fixed the anisotropically aligned PNIPAAm network (step 3 in Fig. 4.2a)[104,105]. The final washing process with the water removed ice crystals and created a PNIPAAm gel with continuously aligned microchannels (Fig. 4.2b). The resulting gel exhibited an average microchannel diameter of ~20 ± 4 μm and an average wall thickness of 0.2 μm in the gel at room temperature (Fig. 4.2c) where the porosity reached 95 ± 1%.

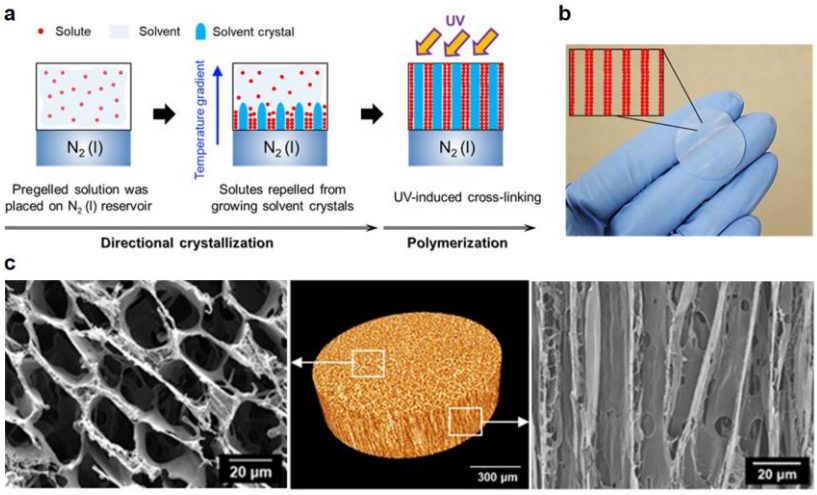

Figure 4.2. Fabrication and analysis of rapid temperature-responsive gel. (**a**) Schematic illustration of the fabrication process of the gel with anisotropically aligned microchannels. The gel is prepared by directional crystallization and subsequent polymerization. (**b**) Image of the resulting microchanneled hydrogel after swelling in water. **c** Microstructure of the gel: scanning electron microscopy (SEM) micrograph of the top surface (left), 3-dimensional imaging of the micro-channeled hydrogel via micro-computed tomography (middle), and SEM micrograph of microchannels that connect the top and bottom of the gel (right).

For comparison, randomly oriented water crystals were created in the PNIPAAm gel by placing the pregelled NIPAAm solution in a freezer at −25 °C and curing it under UV light. The resulting hydrogel showed a similar porosity to the PNIPAAm gel prepared by directional crystallization. However, the microchannels of varying diameters were oriented randomly (Fig. 4.3a). In addition, PNIPAAm gel free of microchannels was prepared by skipping the crystallization step. It was examined the equilibrium swelling ratios (ESRs) of the resulting gels. All samples showed the volumetric swelling change at around 32 °C, which corresponds to the lower critical solution temperature (LCST) of PNIPAAm (Fig. 4.3b). The difference in the ESR between 25 ° and 35 °C was dependent on the microchannel architecture of the gel. In particular, gels with anisotropically aligned microchannels showed a 2.7-fold higher swelling ratio than those with randomly oriented microchannels and a 1.4 times higher swelling ratio than those free of microchannels. The elastic modulus of the gel with anisotropically aligned microchannels was dependent on the direction of microchannels (Fig. 4.3c). The elastic modulus measured by compressing the gel perpendicular to the microchannel was 2.4 kPa, which was twofold lower than that measured by compressing the gel in parallel with the microchannels. In contrast, the gel with randomly oriented microchannels and the gel free of microchannels showed the minimal dependency of the elastic modulus on the direction of compression.

Next, it was examined the extent that the microchannel architecture of the gel modulates the volumetric swelling rate in response to temperature change. The gel without microchannels exhibited minimal volumetric change over 10 s when the temperature was increased from 25 °C to 40 °C. In contrast, the gel with anisotropically aligned microchannels reduced its volume by 60 % within 10 s when temperature increased to 40 °C (Fig. 4.4). This heat-triggered shrinkage is attributed to the decrease of the average cross-sectional diameter of microchannels from 20 to 9 μm as examined with scanning electron microscope images (Fig. 4.5). The microchannel alignment was maintained during the shrinkage. The gel with randomly oriented microchannels also shrank within 10 s when temperature increased to 40 °C (Fig. 4.4). However, the degree of shrinkage was approximately 0.4, which was 20 % lower than the gel with anisotropically aligned microchannels. The electron microscopic images showed lots of open voids as well as micropores collapsed incompletely (Fig. 4.6). In contrast, the gel with aligned microchannels exhibited a more uniform decrease in the microchannel diameter and minimal macro-sized voids after heating (Fig.

4.5). This result indicates that micropores of varying diameters and orientation limit heat-induced collapse, thus leading to the decreased volume shrinkage. Cooling the gel from 40 °C to 25 °C resulted in gel expansion. The speed and degree of volumetric expansion were dependent on the microchannel architecture. The gel without microchannels did not recover its original volume even after 1 hour (Fig. 4.4 and Fig. 4.7). In contrast, both of the gels with microchannels restored their original volume within 10 s due to reswelling. The reswelling plot displayed in Fig. 4.4 was used to quantify the effective water diffusion coefficient (Fig. 4.8). Higuchi equation was used derived under the steady-state approximation of Fick's law of diffusion as follows[106]

$$V_t = V_{25} \cdot (S/V_{40}) \cdot (D' \cdot t/\pi)^{1/2}$$

where V_t is the volume of a gel at time t, D' is an effective diffusion coefficient, and S is an effective surface area. V_{40} and V_{25} are the volume of a gel at 40 °C and 25 °C, respectively. It was assumed that water diffusion occurred exclusively on the gel surface. Anisotropically microchanneled gels had a 75 times higher water diffusion rate than the gel free of microchannels (Fig. 4.8). In addition, the gel with anisotropically aligned microchannels showed a 10 % higher water diffusion rate than that of the gel with randomly oriented microchannels.

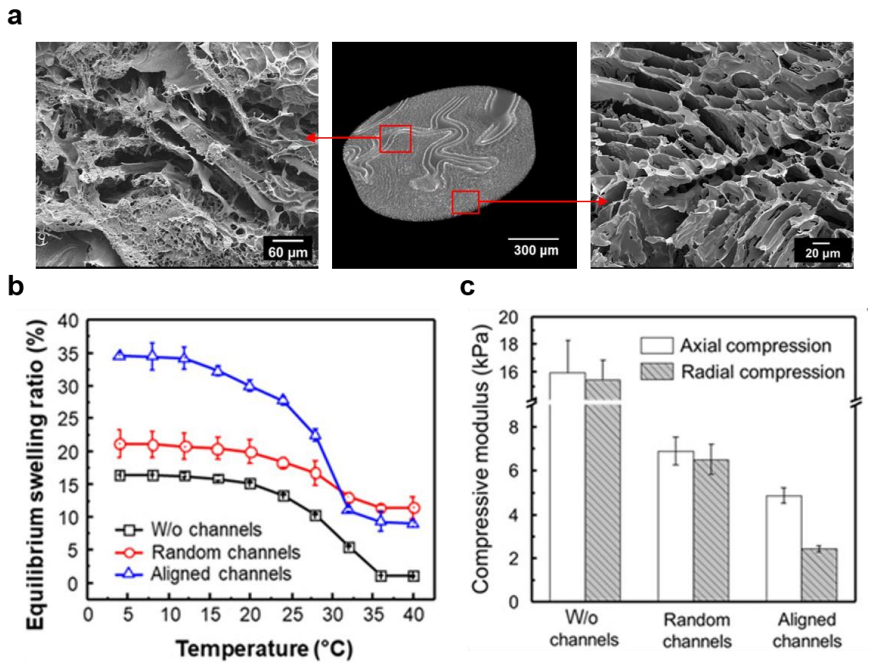

Figure 4.3. (**a**) Microstructure analysis of the gel with randomly oriented microchannels: a, scanning electron microscopy (SEM) micrograph of the top surface (left), 3-dimensional imaging of the hydrogel via micro-computed tomography (middle), and cross-sectional SEM image (right). Freeze-dried samples were used for imaging. (**b**) Equilibrium swelling ratio of gels at different temperatures. (**c**) The compressive elastic moduli of gels. Samples were compressed in parallel with microchannel direction (axial compression) and perpendicular to microchannel direction (radial compression).

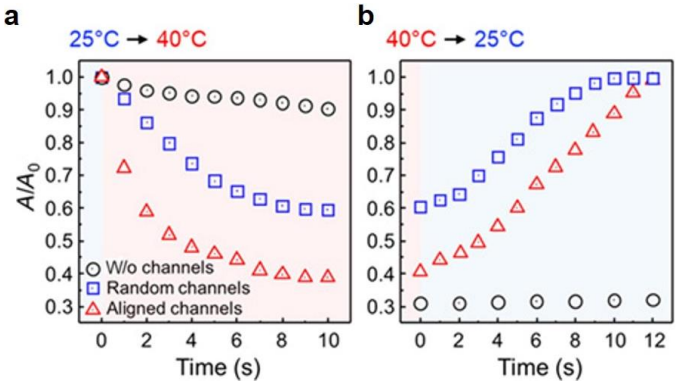

Figure 4.4. Time-dependent volumetric changes of microchanneled gel on heating (left) and cooling (right). The samples were placed on 40° or 25°C plate. The resulting volumetric change was recorded.

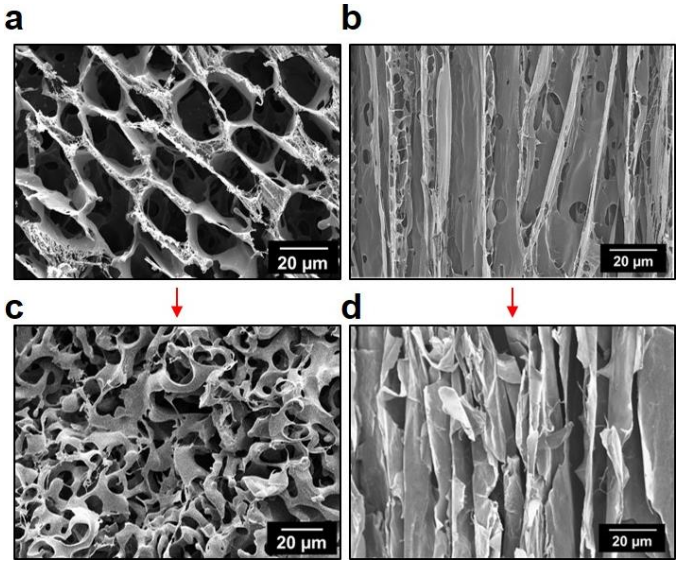

Figure 4.5. SEM micrographs of the top-view (**a**) and lateral view of anisotropically aligned microchannels (**b**) of the gel at 25 °C. SEM micrographs of the top-view (**c**) and lateral view of anisotropically aligned microchannels (**d**) in the gel after shrinkage. The shrinkage was induced by increasing temperature (40 °C).

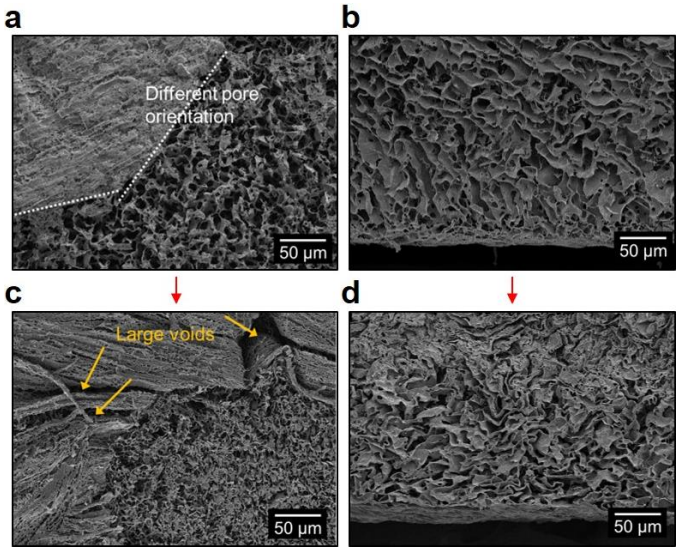

Figure 4.6. SEM micrographs of the top-view (**a**) and lateral view of randomly oriented microchannels (**b**) of the gel at 25°C. SEM micrographs of the top-view (**c**) and lateral view of randomly oriented microchannels (**d**) in the gel after shrinkage. The shrinkage was induced by increasing temperature (40°C).

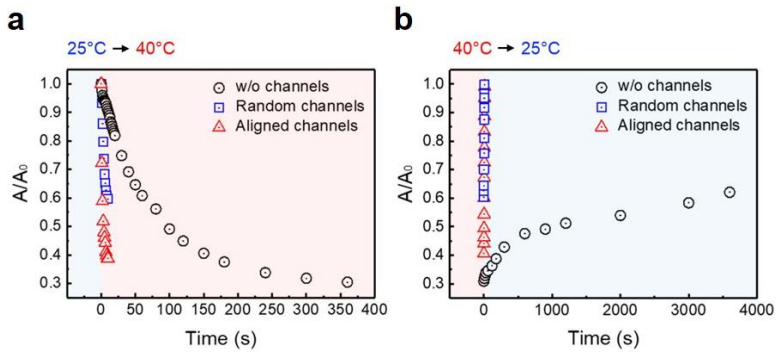

Figure 4.7. Time-dependent areal changes (A/A_0) of the gel without microchannels during heating (**a**) and cooling (**b**). The gel samples were placed on a plate at 40 °C or 25 °C. The subsequent change in the gel surface area was recorded.

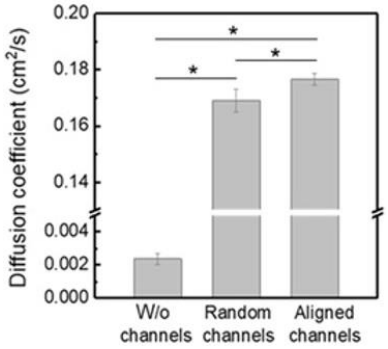

Figure 4.8. Effective diffusion coefficient of water in gels quantified by the reswelling plot (Fig 4.4b). * represents the statistical significance of the difference of values between conditions indicated with line (*P < 0.01).

4.3.3 Design of soft, electrothermal soft manipulator

Separately, a flexible electric (joule) heater was fabricated by photolithographic patterning of a copper/polyimide film (thickness, 9 μm copper/12 μm polyimide). The linewidth and spacing of the copper pattern were kept at 300 μm to provide uniform heat across the gel disk (Fig. 4.9a). The heater was additionally coated with a layer of tin (t ~ 1 μm) to prevent oxidation of the copper at an increased temperature within a humid environment. The heater was then connected to an external power supply with a voltage range of 2 to 5 V (Fig. 4.9b). The activated temperature was examined using an infrared camera, showing that the heater reached the target temperature at 37 °C within 5 s after applying a voltage of 2 V (Fig. 4.9a,b). After the power was turned off, the temperature was dropped immediately back to 25 °C. Such electrothermal heater was attached to

the gel disk using a cyanoacrylate-based adhesive[102]. The bilayered hydrogel-heater construct was finally attached to a three-dimensional (3D) printed supporter (Fig. 4.9c).

The resulting electrothermal soft manipulator, the response of the gel disk to the electrical signal was examined. The test was conducted outside water. Figure 4.10 shows the side view of the gel disk and the microstructural changes of the gel surface during the electrically controlled heating and cooling cycle. Switching on the heater triggered shrinkage of microchannels within 10 to 20 s and simultaneously released a fraction of water from the gel (Fig. 4.10a). With the power off, the gel expanded the microchannels and reabsorbed the water within a few seconds (Fig. 4.10b). The shrinkage and expansion of microchannels could be repeated hundreds of times by turning the power on and off. No structural failure of the gel was observed during repeated operation. It was further examined the heat transfer through the gel layer placed on the heater at a temperature of 40 °C (Fig. 4.11a). With the heater on, the temperature of the gel increased rapidly from the bottom (point 1 in Fig. 4.11b) to a top (point 4 in fig. 4.11b) within 20 seconds. This result confirms heat propagation along the gel thickness direction. The gel temperature increased at a rate of 0.3 °C/mm·s, independent of the region of observation. Last, the temperature of the entire gel became equal to that of the heater within 30 s (Fig. 4.11c). The gel with randomly oriented microchannels also underwent shrinkage and expansion in response to the electrothermal signal. However, the area undergoing microchannel shrinkage and expansion was not as uniform as in the gel with anisotropically aligned microchannels (Fig. 4.12). Therefore, the gel released water locally. The gel without microchannels showed a very slow release and limited absorption of water when the electric heater was on and off, respectively (Fig. 4.13).

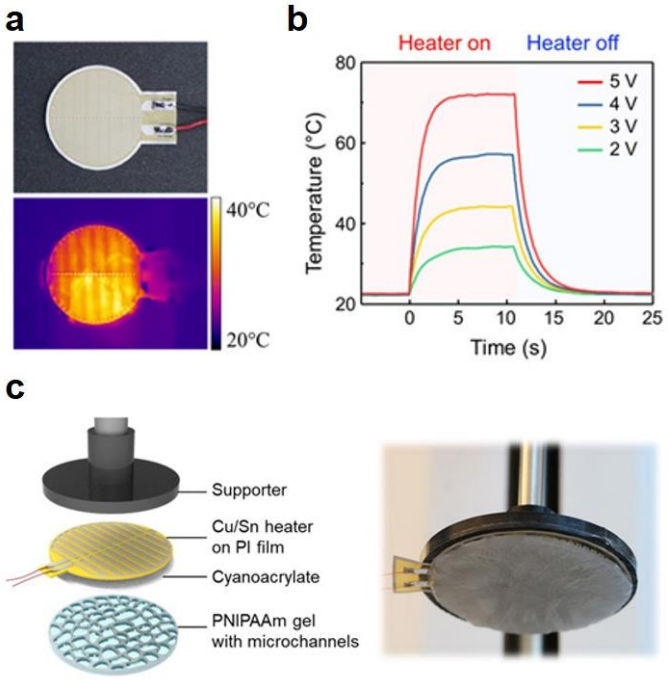

Figure 4.9. (**a**) Photograph (top) and a thermal image of the flexible heater captured using an infrared camera (bottom). (**b**) Temperature change over time at differently applied voltages. The temperature profiles of the heater were obtained using an infrared camera. **c** Structural configuration of the soft manipulator (left) and a photograph of the soft manipulator (right).

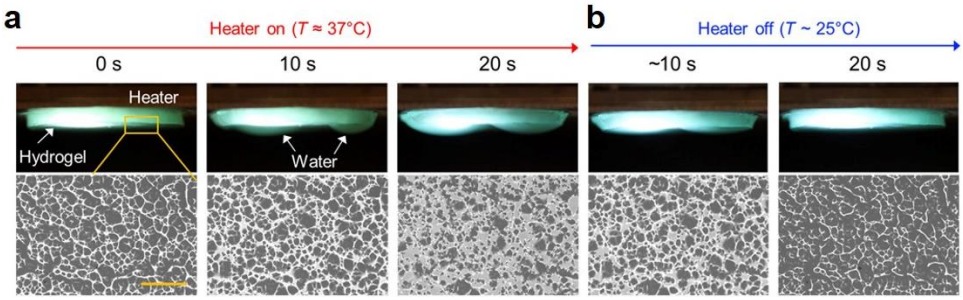

Figure 4.10. Optical image of the microchanneled gel in the soft manipulator when the heater was turned on (**a**) and off (**b**). Images on the bottom row represent optical microscopic images of the gel surface when the heater was turned on and off. When the heater was turned on, aligned microchannels of the gel pushed water out while being closed for 20 s (**a**). When the heater was switched off, the gel in the soft manipulator opened microchannels and pulled water back into microchannels within 20 s (**b**). Scale bar, 100 μm. Working mechanism and characterization of the soft manipulator.

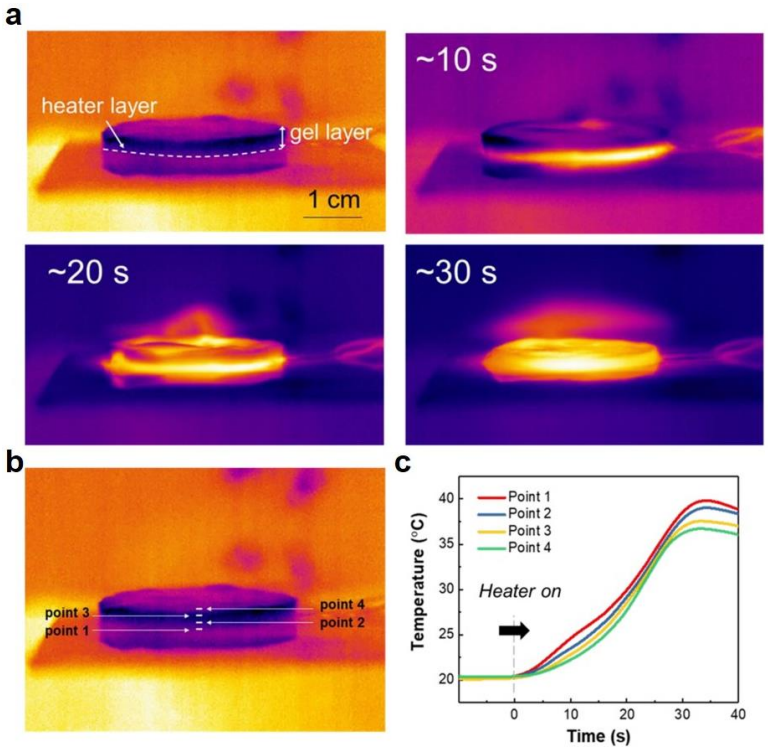

Figure 4.11. Heat transfer properties of the soft manipulator. (**a**) Snapshots show the heat propagation through the gel, which is attached to a heater. The activation temperature of the heater was 40 °C. The gel used herein is the microchanneled PNIPAAm gel. (**b**) A thermal image showing regions of interest. (**c**) Temperature of the gel versus time. The diameter and thickness of the gel used in this analysis are 30 and 2 mm, respectively.

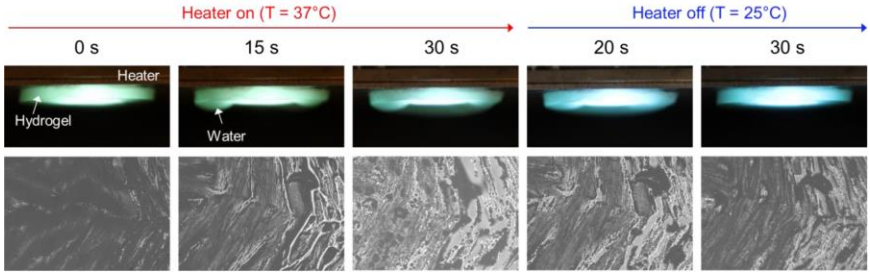

Figure 4.12. Snapshots of the gel with randomly oriented microchannels when the heater was turned on and off (upper images). Below images are optical microscopic images of the corresponding surface of the gel. The dark area represents the gel bulk, and the bright area represents the wall of microchannels.

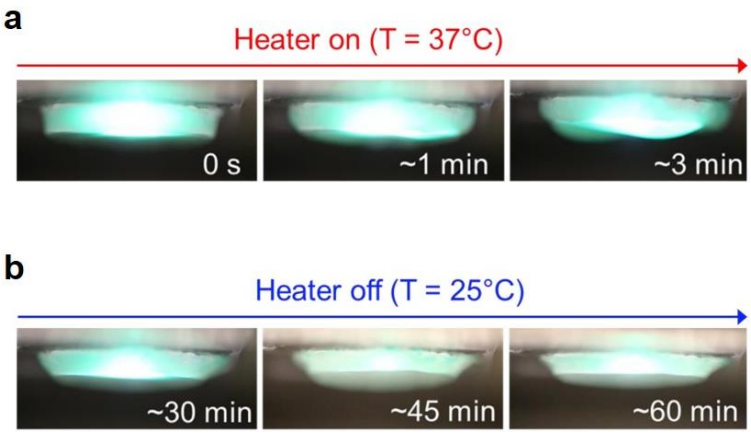

Figure 4.13. Snapshots of the gel without microchannels when the heater was turned on (**a**) and turned off (**b**).

4.3.4 Working mechanism and characterization of the soft manipulator

The shrinkage and expansion of anisotropically aligned microchannels allowed the gel to grip, lift, and release materials of interest (Fig. 4.14). The manipulator with a diameter of 25 mm was used in this study. The manipulation process was conducted as follows. First, the upper part of the microchannels of the hydrogel was shrank by activating the heater (stage 1 in Fig. 4.14). During this process, the gel released a fraction of water, thus creating an empty pocket between the heater and residual water in the microchannels. The gel was then placed on a 4-inch-diameter silicon wafer, a model material that should be transported (stage 2 in Fig. 4.14). Next, the heater was deactivated to expand the shrunken microchannels and move residual water upward [stage 3 (i) in Fig. 4.14]. The subsequently formed vacant space between water within the microchannels and the silicon wafer decreased the pressure inside microchannels, thus making the gel adhere to the silicon substrate. Thus, the soft manipulator could lift the substrate [stage 3 (ii) in Fig. 4.14]. Last, with the power on, microchannels adjacent to the heater shrank and pushed water out of the microchannel (stage 4 of Fig. 4.14). The subsequent pressure increases inside the microchannels served to dislodge the silicon wafer quickly. This mechanism is distinct from artificial handling systems assembled with an inspiration from anatomy of the cephalopods suction cup. These handling systems, however, require external force to hold and release materials of interest. In contrast, the manipulation process performed by our soft manipulator resembles the neuromuscular actuation in which cephalopods grip and release materials of interests. Through control of

electricity, the rapid electrothermal actuation of the gel enabled the manipulator to systematically lift up and release target materials without external forces.

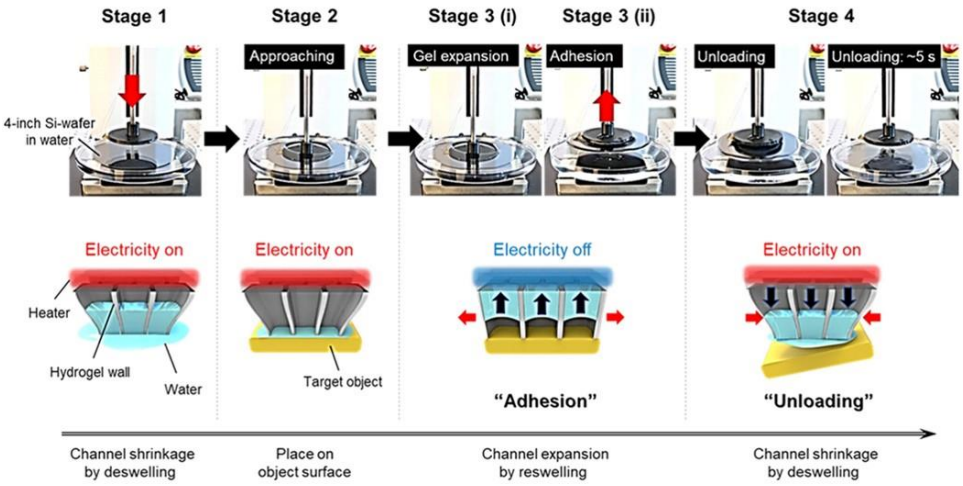

Figure 4.14. Snapshots showing the transport of a 4-inch-diameter silicon wafer using a soft manipulator (upper images). Schematic illustrating the shrinkage and expansion of microchannels and subsequent water movement in microchannels controlled by the electrothermal signal (bottom images). The operating power of the soft manipulator was 5W.

The normal pressure development of the gel to the silicon surface was further measured, particularly during stages 2 and 3. This measurement was conducted by attaching the bilayered gel-heater construct to a dynamic mechanical analyzer (DMA) (Fig. 4.15). First, the gel was preheated by the heater and brought into contact with a 4-inch silicon wafer ("Approaching" stage in Fig. 4.15). Next, when the power was turned off to expand microchannels, the load was increased in the negative direction for 25 s ("Gel expansion" stage in Fig. 4B). This bilayered gel-heater construct was then slowly pulled upward at 0.1 mm/s by DMA to monitor the increase of the adhesion strength ("Adhesion" stage in Fig. 4.15). The maximum adhesion strength reached 1.5 kPa. Once the power was turned on before the stress reached 1.5 kPa, the normal adhesion strength decreased quickly to 0 kPa within 5 s ("Unloading" stage in Fig. 4.15).

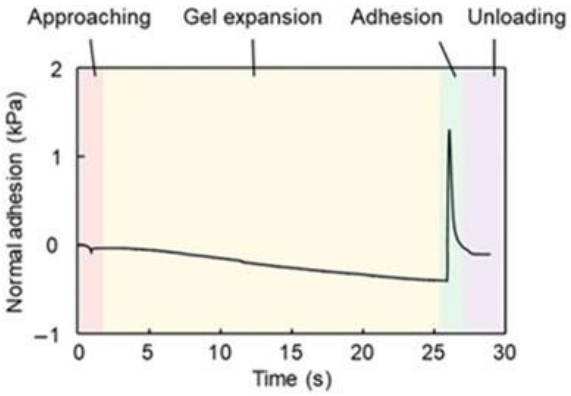

Figure 4.15. The time-dependent variation of normal adhesion strength measured by the dynamic mechanical analyzer (DMA) during stages 2 and 3 in (4.14). An initial contact strength of 0.05 kPa was applied to the soft manipulator for this measurement.

Without temperature control, the manipulator does not exhibit adhesion. It was further examined whether temperature-induced contraction and expansion of microchannels are essential to create adhesion. The soft manipulator preheated to 37 °C was placed on the silicon wafer immersed in water with controlled temperatures. Then, the heater of the soft manipulator was turned off. At temperatures below LCST of the gel layer (i.e., ~32 °C), the adhesion strength increased rapidly with decreasing temperatures (Fig. 4.16). This result confirms that temperature of the heating layer in the manipulator controls the degree of expansion of the microchanneled gel layer and, in turn, regulates adhesion strength. It was proposed that the electrothermally controlled adhesion of the gel to the silicon wafer results from the pressure difference (ΔP) between two ends of microchannels. The mixture of rhodamine B and water were introduced the into microchannels of the gel and monitored the vertical movement of water through the individual microchannel during stage 3 (i) in Fig. 4.14. According to the side view of the gel captured with confocal microscopy, the micro-channeled gel disk was fully filled with water (Fig. 4.17, top). Heating and the subsequent cooling process resulted in the space in the lower part of the microchannel adjacent to the silicon substrate by moving residual water upward in the microchannels (Fig. 4.17, bottom). This image is similar to the scheme that represents stage 3 in Fig. 4.14. The average height of space in the microchannel was approximately 50 μm. The pressure difference of a single microchannel in the gel was quantified with a height of the empty part in the microchannel as follows

$$\Delta P = \rho_W \cdot g \cdot (h_i - h_f)$$

where ρ_w is the density of water, g is the gravitational acceleration, and h_i and h_f are the height of the space in microchannels when the power was turned on and off, respectively. According to the calculation, each microchannel in the gel produced 0.5 Pa of negative pressure after the cooling process.

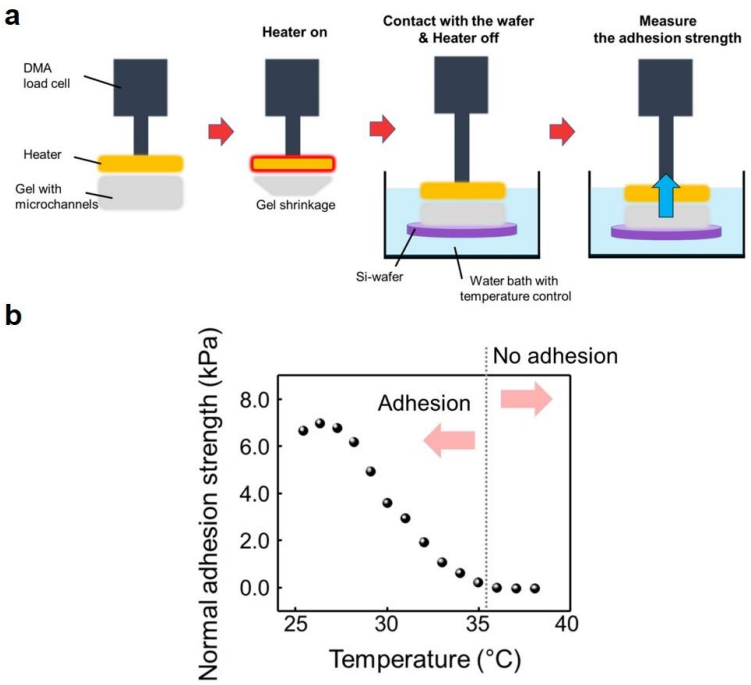

Figure 4.16. (**a**) Schematic illustration of the set-up that measures the normal adhesion strength in the water of varying temperatures. The gel layer of the soft manipulator was pre-heated by the heater and brought into contact with a 4-inch diameter silicon wafer immersed in a water bath. The temperature of the water bath was controlled by a digital circulator. Then, the heater of the soft manipulator was turned off. The adhesion strength was measured by a DMA. (**b**) The adhesion strength of the soft manipulator measured at different temperatures of water.

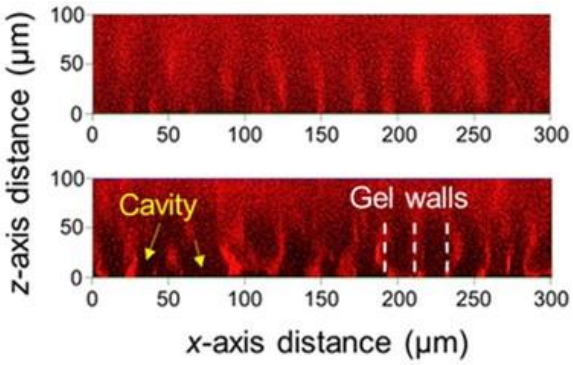

Figure 4.17. Fluorescence images of water in microchannels of the gel. The image was obtained from a 3D z-stack confocal microscope before (top) and after adhesion (bottom) of the soft manipulator to a target surface. The heater was attached to the upper part of the gel.

The adhesion strength of the gel to the silicon wafer was dependent on the initial load applied to the soft manipulator (Fig. 4.18). The maximum adhesion strength reached 65 kPa with the initial pressure of 5.0 kPa. The maximum adhesion strength reached 65 kPa with the initial pressure of 5.0 kPa. To underlie the mechanism, the normal pressure development which varies with the initial contact pressure was examined using a DMA equipment. As shown in fig. 4.19a, the heated soft manipulator was placed on the target silicon wafer. As soon as the heater was turned off, the gel layer expanded and pushed the silicon wafer more strongly. As a consequence, the normal pressure developed in the opposite direction. The normal pressure increased with the initial contact pressure (Fig. 4.19b). Increasing the initial contact pressure enlarged the effective suction area of the soft manipulator and also augmented the normal pressure.

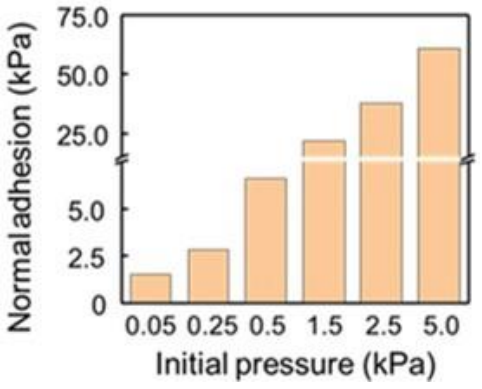

Figure 4.18. Dependency of the adhesion strengths on the initial load.

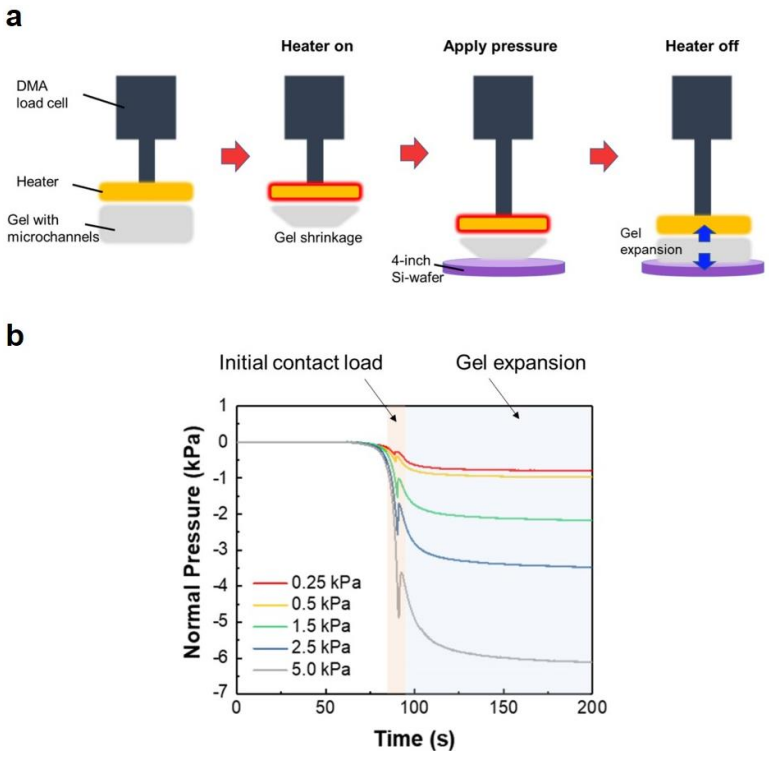

Figure 4.19. (**a**) Schematic illustration of measurement of the normal pressure development under different initial contact pressures. The gel layer of the soft manipulator was pre-heated by the heater and brought into contact with a 4-inch diameter silicon wafer. DMA controlled the initial contact pressure of the gel layer onto the silicon wafer. Then, the heater of the soft manipulator was turned off to expand the gel layer. (**b**) The normal pressure developed by the soft manipulator varies with the initial contact pressure.

It was also observed that the effect of elastic modulus of target materials on the adhesion strength. Alginate hydrogels with elastic moduli of 22.5 and 69.8 kPa was prepared as target materials for transport (Fig. 4.20a). As confirmed with the pressure development profiles, with a given initial contact pressure of 0.25 kPa, the soft manipulator exhibited a similar magnitude of the adhesion strength to the alginate gels as well as the silicon wafer with a much higher elastic modulus of 140 to 180 GPa. This result suggests that it is not necessary to vary the initial contact pressure with the target material stiffness (Fig. 4.20b). The adhesion strength was not reduced during the repeated cycles of closure and opening of microchannels (Fig. 4.21). No chemical contamination or residue was observed on the silicon wafer after the process (Fig. 4.22). The soft manipulator could transport plastic and glass materials by exerting a similar magnitude of the adhesion strength regardless of material hydrophobicity (Fig. 4.23). The soft manipulator functioned to transport materials immersed in aqueous media and those in the air.

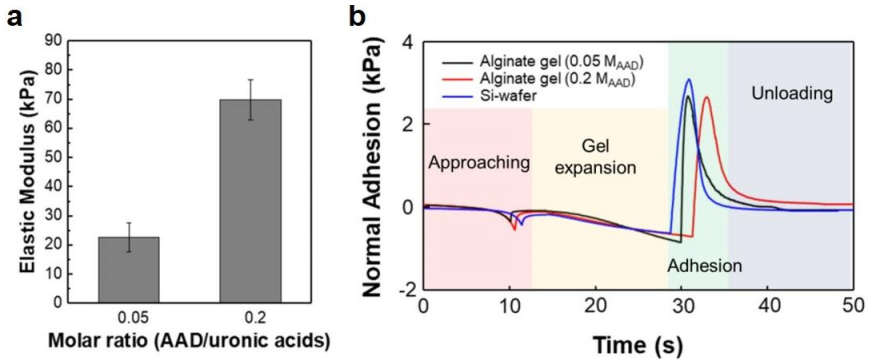

Figure 4.20. (**a**) Elastic modulus of the alginate hydrogels prepared by cross-linking reaction between uronic acid of alginate and adipic acid dihydrazide (AAD). 0.05 and 0.2 represent the molar ratio between AAD and uronic acids of alginate (MAAD). (**b**) The normal pressure development of the soft manipulator against different target materials. An initial contact strength of 0.25 kPa was applied to the soft manipulator for this measurement.

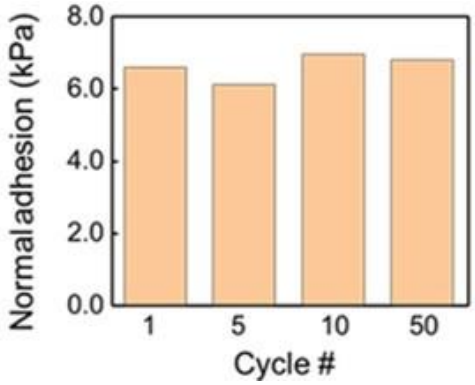

Figure 4.21. Variation in the adhesion strength as a function of cycle number.

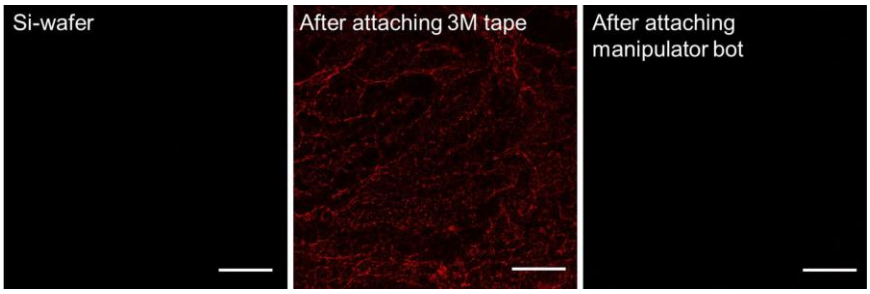

Figure 4.22. Fluorescence images of the surface of silicon wafers before and after the adhering process. Samples were incubated with Rhodamine B for 30 minutes after performing the adhesion test.

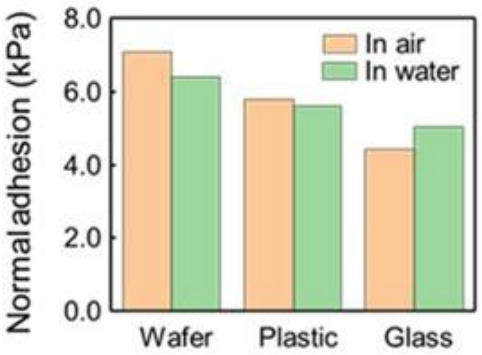

Figure 4.23. Adhesion strength of the soft manipulator measured with the various target substrates in water and air. An initial contact strength of 0.5 kPa was applied to the soft manipulator using DMA for this measurement.

4.3.5 Demonstration of the soft manipulator to transport cell sheets to target sites

Last, capability of the soft manipulator to lift up, transport, and release ultrathin and delicate materials, such as living cell sheets and ultrathin thin film devices was examined. A single-layered mouse skeletal myoblast cell sheet was prepared in a cell culture dish. In general, monolayered cell sheets were easily damaged or crumpled when picking up the sheet from the cell culture dish with forceps (Fig. 4.24a). By switching the heater of the soft manipulator on and off, it was possible to lift the myoblast cell sheet and transport them to the new target sites. First, the cell sheet was transferred to a glass dish using the soft manipulator (Fig. 4.25b). Then, it was examined whether the soft manipulator caused and damages to the sheet during transplantation. Off-axis deformation and viability of the cell sheet before and after delivering process were measured using the spatial light interference microscopy (SLIM) and the live-dead assay kit, respectively. According to SLIM observation and live-dead assay results, there was no substantial wrinkling nor loss of viability of cells that formed the cell sheet during this transport process (Fig. 4.25c). This simple transportation process allowed us to fabricate a 3D tissue by stacking multiple myoblast sheets using the soft manipulator (Fig. 4.24d). The resulting three-layered myoblast tissue showed a dense construct with three different layers.

The soft manipulator allowed us to pick up various types of cell sheets and deliver them rapidly to any target surfaces. As a demonstration, previously cultured myoblast cell sheet was delivered

to an ex vivo muscle tissue without any structural breakages (Fig. 4.25a). The entire transport process could be completed within 30 seconds. In contrast, the soft manipulator assembled using a gel with randomly oriented micropores could not uniformly deliver the cell sheet due to the nonuniform micropore shrinkage (Fig. 4.25b). The soft manipulator was used as a device to support atraumatic transplantation of a stem cell sheet to the anterior surface of the cornea. Similar to the myoblast cell sheet, mesenchymal stem cell sheets on a donor substrate could be easily transferred to the corneal epithelium of a rat eye (Fig. 4.26a). The reliable attachment of the stem cell sheet to the anterior surface of the cornea was confirmed, within the position of the corneal epithelium of the rat eye by histological observation (Fig. 4.26b). A method to atraumatically transplant ex vivo generated stem cell sheets could simplify surgical technique and expand access to corneal epithelial stem cell transplants and it could have useful application in the treatment of corneal epithelial injuries, persistent epithelial defects, limbal stem cell deficiencies, nonhealing corneal ulcers, and blast injuries[107,108].

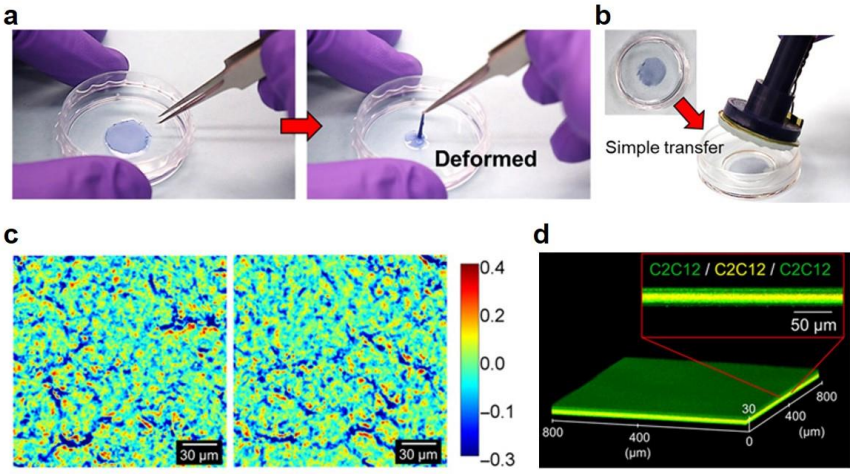

Figure 4.24. (**a**) Snapshots of a process to pick up a skeletal myoblast sheet with forceps. The cell sheet was deformed when picking up the sheet using forceps (right). The cell sheet was stained with methylene blue for visualization. (**b**) Snapshot of a process to transport the skeletal myoblast sheet onto a glass surface using the soft manipulator. (**c**) Spatial light interference microscopy (SLIM) images of the cell sheet before (left) and after (right) the transfer, showing off-axis diffraction of the cell sheet. (**d**) Fluorescence image of a multilayered cell sheet consisting of three different myoblast sheets. The multilayered sheet was prepared by stacking cell sheets using the soft manipulator.

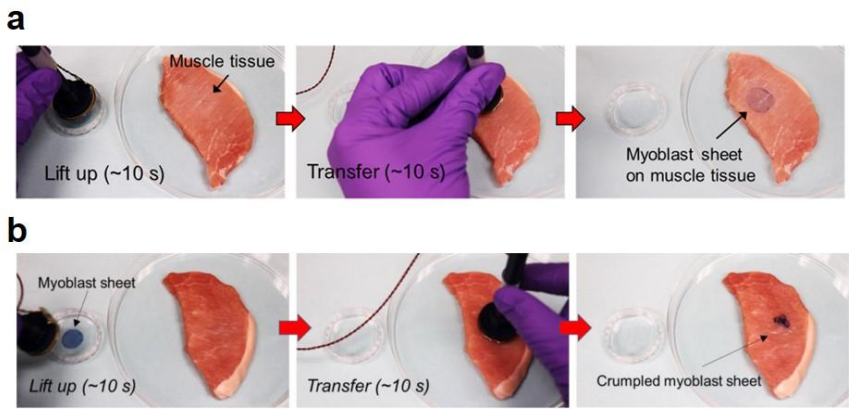

Figure 4.25. (**a**) Snapshots of a process to transport a skeletal myoblast sheet onto a muscle tissue. It took 30 s for the entire transfer process. (**b**) Snapshots of a process to transport a skeletal myoblast sheet onto a muscle tissue using a soft manipulator made with the gel layer with randomly oriented microchannels.

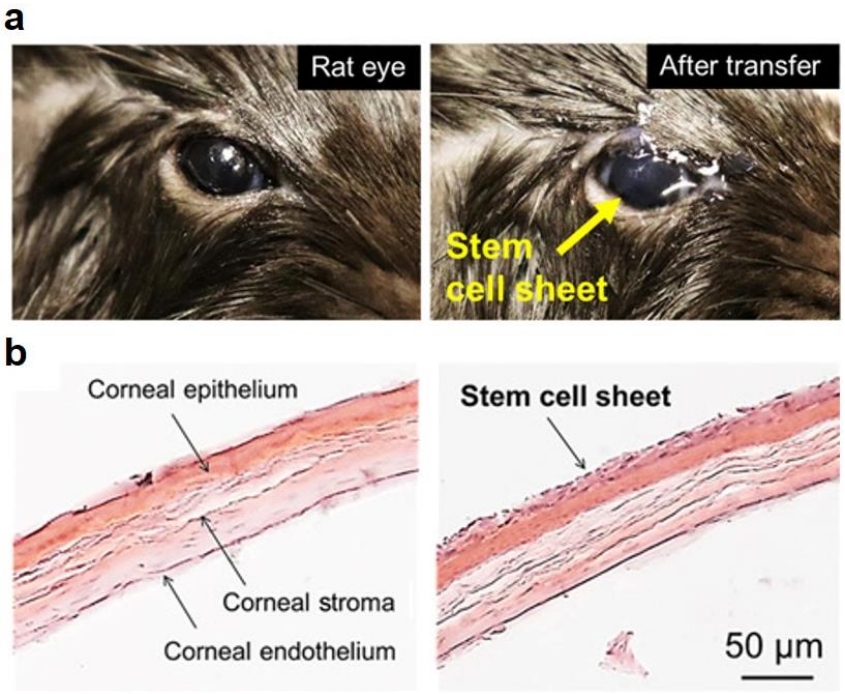

Figure 4.26. (**a**) Photographs of a rat eye before and after transplantation of a stem cell sheet. The cell sheet transplanted to the corneal epithelium of a rat eye using the soft manipulator. It took 30 s for the entire transfer process. (**b**) Histological examination of the rat eye before (left) and after (right) a stem cell sheet transfer. Hematoxylin and eosin staining revealed that the stem cell sheet was able to be successfully transplanted onto the anterior corneal surface without substantial interface space generation.

4.3.6 Transportation of an ultrathin EP sensor

In addition, the soft manipulator was used to transport an ultrathin electrophysiological (EP) sensor (thickness, ~1 μm) without causing wrinkling. The EP sensor that consists of reference, ground, and measurement electrodes was fabricated allowing high-quality recording of electrocardiogram (ECG) signals (Fig. 4.27a)[76,109]. Generally, such ultrathin film devices were easily crumpled when picking up from a donor substrate, which typically requires the use of a temporary handling support (Figure 4.27b). By using the soft manipulator, it was possible to controllably transfer the EP sensor from the donor substrate to the surface of the pig heart within a minute (Fig. 4.28a). No substantial wrinkles were observed after completing the transport (Fig. 4.28b). A waveform generator was used to apply a preprogrammed ECG signals across the pig heart using an Ag/AgCl electrode. The resulting ECG signals captured from the EP sensor were nearly identical to those generated from the waveform generator (Fig. 4.28c). The Pearson's correlation coefficient of the signals was 0.98.

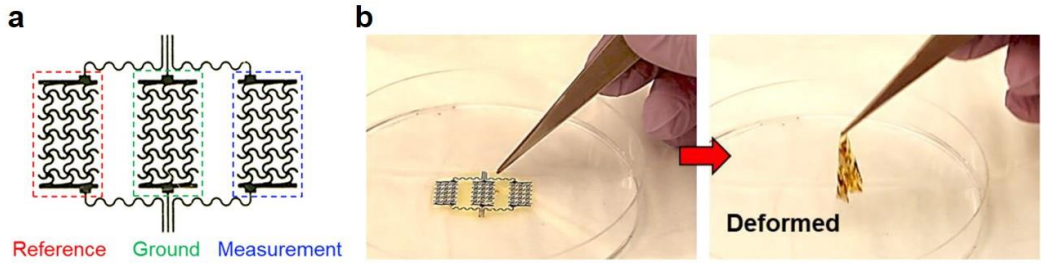

Figure 4.27. (**a**) Device configuration of the ultrathin EP sensor. (**b**) Snapshots of a process to pick up the ECG device with forceps. The device was deformed when picking up with forceps.

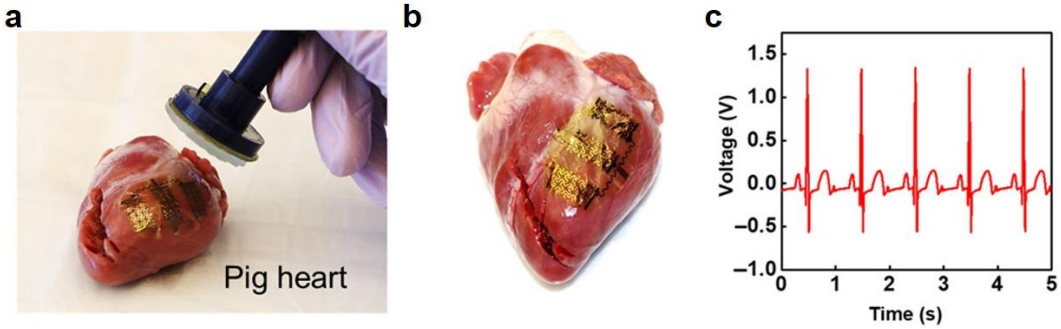

Figure 4.28. (**a**) Snapshot of a process to transport the device to the surface of the pig heart. (**b**) Photograph of the device transplanted to the pig heart using the soft manipulator. (**c**) Representative ECG signals measured using the transplanted device.

4.4 Discussion

Altogether, this study demonstrates that the soft manipulator assembled by integrating a rapid thermal-responsive microchanneled gel and an electrothermal heater can transport ultrathin biological and electronic materials quickly and safely. The resulting soft manipulator could be switched on and off with electricity to lift and release thin and delicate materials within tens of seconds. This rapid handling could be attained with the electrothermally controlled change in the adhesion force between the soft manipulator and target materials. Such an actuation mechanism is very similar to the muscular action of cephalopod suction cups. Therefore, this soft manipulator is distinct from previous suction cup–mimicking platforms that need external force for detachment of materials. In addition, the soft manipulator could move thin materials of interest in both wet and dry conditions. Using this unique functionality, it is possible to assemble multilayered cell sheets and place an ultrathin biosensor to the target tissue without impairing its function. It is possible that further modification of this soft manipulator with an electronic sensor would allow robots to transport ultrathin materials autonomously. For instance, the resulting smart soft manipulator would be able to monitor the degree of deformation of transporting materials during contact and, in turn, adjust the suction force to a level at which materials retain their structural integrity and functionality. By doing so, the soft manipulator would improve its performance from the standpoint of safety and accuracy of material handling and assembly. The present design concept may be widely used as a new soft handling tool for the fabrication of ultrathin film devices, tissue engineering, and transplant surgery.

This study demonstrated an electrically controllable soft machinery useful to transport ultrathin, delicate objects, including therapeutic cell sheets and thin, wearable biosensing devices. This system, named as the electrothermal soft manipulator, consisted of a flexible heater attached with a rapid thermo-responsive PNIPAAm hydrogel disk with controlled microchannel architecture and tissue-like softness. Compared with hydrogels free of microchannels or those with randomly oriented microchannels, the anisotropically aligned PNIPAAm hydrogel could shrink and expand in response to the electrically induced heat much faster, on the order of seconds. Such a fast-volumetric change of the microchannels on the surface of an object could produce and remove pressure-induced adhesion repeatedly. This controlled actuation mechanism is similar to the activity of cephalopod suction cups that hold and release objects of interest using bioelectric

signals. As a consequence, the soft manipulator could move thin biological and bioelectronic devices quickly in both wet and dry conditions without causing wrinkling or damage of the thin materials. Such an electrothermally controlled soft manipulator would be useful to various applications that require the sophisticated manipulation of fragile and delicate biological tissues and bioelectronic devices.

4.5 Acknowledgements

The figures, results and manuscript in this chapter is reprinted/adapted with permission from "Electrothermal soft manipulator enabling safe transport and handling of thin cell/tissue sheets and bioelectronics devices" *Science Advances*, 6, 42 eabc5630. Copyright 2020 American Association for the Advancement of Science. I express sincere gratitude to all of the coauthors on this journal publication, Dr. Byoung Soo Kim (University of Illinois at Urbana-Champaign), Younghak Cho (Korea Advanced Institute of Science and Technology), Eman E. Hamed (University of Illinois at Urbana-Champaign), Martha U. Gillette (University of Illinois at Urbana-Champaign), Hyeongyun Cha (University of Illinois at Urbana-Champaign), Nenad Miljkovic (University of Illinois at Urbana-Champaign), Vinay K. Aakalu (University of Illinois at Chicago), Kai Kang (University of Illinois at Chicago), Kyung-No Son (University of Illinois at Chicago), Kyle M. Schachtschneider (University of Illinois at Chicago), Lawrence B. Schook (University of Illinois at Urbana-Champaign), Chenfei Hu (University of Illinois at Urbana-Champaign), Gabriel Popescu (University of Illinois at Urbana-Champaign), Yeonsoo Park (Purdue University), William C. Ballance (University of Illinois at Urbana-Champaign), Dr. Seunggun Yu (Korea Electrotechnology Research Institute), Prof. Sung Gap Im (Korea Advanced Institute of Science and Technology), Prof. Jonghwi Lee (Chung-Ang University), Prof. Chi Hwan Lee (Purdue University) and Prof. Hyunjoon Kong (University of Illinois at Urbana-Champaign).

5. 3D SCAFFOLD SENSOR FOR MONITORING OF CELLULAR BEHAVIOR

5.1 Introduction

The ability to record cellular behaviors and functions with high spatial and temporal resolutions enables fundamental understanding of the underlying biophysics and cellular electrophysiology[110-114]. Conventionally, the real-time monitoring of electrical activities of living cells occurs by using various sensing platforms such as optical imagers with voltage-sensitive dyes[114], graphene-based sensors[115], multiplexed electrode arrays[116,117], and planar field-effect transistors (FETs)[118-120], but their spatial resolution remains limited because these methods are tailored for 2D cultured cells. The recent advent of injectable or roll-able scaffold systems enables the spatially resolved 3D mapping of the cellular behaviors and functions in human tissue-mimicking environments[121,122]. Nonetheless, challenges remain for their long-term, high-fidelity recording due to the lack of effective means to electrically decouple all of the necessary electronic instrument settings from submerged conditions in a cell culture medium including oxygen, pH, conductivity, and/or agitation, which often requires additional packaging to prevent wetting and damaging[123].

In this chapter, a 3D-stackable electronic scaffold (e-scaffold) integrated with an engineered ultrabuoyant structure that allows the entire structure to remain afloat on the surface of medium and therefore offers favorable environments for both biological cells and electronics. The e-scaffold system contains multimodal arrays of sensing elements in vertically stackable configurations, providing the capability for spatially resolved 3D mapping of cellular behaviors and functions. Demonstrations of the e-scaffold system in 3D mapping of cellular impedances and cardiac action potentials from cancer and cardiomyocyte cells with high fidelity over weeks illustrate the utility of this concept. Comprehensive in vitro studies reveal the important features of the underlying materials, design rules, operational arrangements, and all of the relevant aspects of operations.

5.2 Materials and methods

5.2.1 Fabrication of the e-scaffold system

The fabrication began by spin-casting the layers of PMMA (1 μm thick) and PI (1 μm thick) on a Si substrate. Thin films of Cr/Au film (5 nm/150 nm) were deposited by using an electron-beam (e-beam) evaporator. A photolithographic patterning with a photoresist (AZ 1518, 3000 rpm, 30 s) and subsequent wet etching steps in solutions of Cr and Au etchants (Transene, Inc.) followed to define the metallic thin film electrodes and the interconnecting traces. The encapsulation layer of PI (1 μm thick) was spin-casted on top and patterned by photolithography with a photoresist (AZ 9260, 3000 rpm, 1 min) and oxygen (O_2) plasma reactive ion etching (RIE) to define the basic structure of the e-scaffold system.

5.2.2 Fabrication of microporous sponge-like ultra-buoy

The fabrication began by spin-casting a mixture of PDMS base material and curing agent (10:1 weight ratio) on a glass substrate at 100 rpm for 10 min. The as-prepared PDMS was then placed into a pressure cooker maintained at the preset pressure (90 kPa) and temperature (100 °C) for 20 min. The microscale pores were formed during the high-pressure steaming step while the PDMS was completely polymerized, providing the super hydrophobicity and antiwetting performance. The resulting microporous sponge-like PDMS was dried in a convection oven at 70 °C for 1 h to remove the residual water molecules. A solution of Teflon (1 wt % AF2400, Dupont, USA) mixed with PTFE nanoparticles (0.2–5 μm, Polysciences, Inc. and Sigma-Aldrich, USA) was spin-casted at 1000 rpm for 5 min and then cured at 150 °C on a hot plate to increase the surface tension force, leading to increased static water contact angle and decreased effective surface adhesion against cell medium.

5.2.3 Measurement of static contact angle and dynamic droplet

The static contact angle was measured by placing a droplet (~10 μL) of distilled (DI) water and oil on a specimen by using a computer-controlled contact angle analyzer (Surface Electro Optics, Phoenix-10). The dynamic droplet behaviors of DI water and oil when dropped (~15 μL) from a height of ~4 cm was monitored by using a high-speed camera at 50 frames per second.

5.2.4 Cell compatibility assay

The specimens were sterilized by soaking in 70% (v/v) ethanol for 30 min and rinsing twice with phosphate buffer saline (PBS) followed by dehydration under UV irradiation for 1 h. The specimens were treated with O_2 plasma (35 W, 3 min) and immersed in fibronectin/gelatin solution (0.5% fibronectin, F1141, Sigma-Aldrich, USA, and 0.02% gelatin, Fisher Scientific, USA) for 1 day. The cells suspended in 50% medium and 50% Matrigel (Corning Life Sciences, USA) were then seeded on the specimens. In order to assess the cell proliferation, ~5 × 103 cells were seeded and incubated. After the incubation, 3-(4,5-dimethylthiazol-2-yl)-2,5-diphenyltetrazolium bromide (MTT, Sigma-Aldrich, USA) was added to the cells, and the fluorescent intensity was measured at 580 nm by using a microplate reader (SpectraMax Plus 384 reader, Molecular Devices, USA). For the confocal microscopy analysis, the cells were fixed with 4% v/v paraformaldehyde in PBS for 15 min, stained with DAPI (500 nM, Invitrogen, USA) or Draq5 (1 μM, Invitrogen, USA) for 2 min, and mounted with an antifade reagent. The resulting cells were imaged by using the A1Rsi confocal microscope (Nikon, Japan).

5.2.5 Cardiomyocyte isolation

Primary neonatal mice cardiomyocytes were prepared according to the Pierce Primary Cardiomyocyte Isolation Kit (Thermo Scientific, USA). Briefly, neonatal hearts were isolated from 1–3 day old neonatal mice and placed into separate sterile microcentrifuge tubes containing 500 μL of ice-cold Hank's Balanced Salt Solution (HBSS). Each isolated heart was then minced into 1–3 mm^3 pieces and washed twice with 500 μL of ice-cold HBSS to remove blood from the tissue. The minced tissues were incubated with 200 μL of reconstituted Cardiomyocyte Isolation Enzyme 1 (with papain) and 10 μL of Cardiomyocyte Isolation Enzyme 2 (with thermolysin) to each tube in an incubator at 37 °C for 30 min. After the incubation, the tissues were removed from the enzyme solution and washed twice with 500 μL of the ice-cold HBSS and 500 μL of complete Dulbecco's modified Eagle's medium (DMEM) was added for primary cell isolation to the tissues. The cardiomyocytes (6×10^6) were seeded onto a specimen with 50 % medium and 50 % matrigel (Corning Life Sciences, USA). The cell constructs were supplemented with complete DMEM for primary cell isolation and further incubated.

5.2.6 Immunostaining

For the cardiomyocyte immunostaining, the cardiomyocytes were fixed with 4% paraformaldehyde (Electron Microscope Sciences, USA) in PBS for 30 min and then washed three times with PBS. The cardiomyocytes were incubated with 0.25 % Triton X-100 (Sigma-Aldrich, USA) in PBS for 1 h and washed three times with ice-cold PBS and preblocked for 1 h at room temperature in PBS containing 10 % FBS, after which the specimens were washed three times with PBS. The specimens were incubated with primary antisarcomeric α-actinin mouse monoclonal antibodies (1:250; Sigma-Aldrich, USA) in SuperBlock (TBS) blocking buffer solution (Thermo Scientific, USA) for 1 hour at room temperature, washed three times, and then incubated with AlexaFluor-488 goat antimouse secondary antibody (1:400; Invitrogen, USA) for 1 hour, followed by rinsing with PBS. For the cell nuclei staining, the cardiomyocytes were stained with 1 μM of Draq5 for 2 min and then rinsed with PBS. The resulting specimens were imaged by using the A1Rsi confocal microscope (Nikon, Japan).

5.2.7 Measurement of impedance

The impedance was measured by using an LCR meter (Agilent 4294A, USA) with a voltage (between two adjacent recording electrodes) of ~1 mV for 48 h at frequencies of 1, 5, 10, 20, 30, 50, 100, 150, 200, and 250 kHz, respectively. The e-scaffold system was placed in the incubator (5 % CO2, 37 °C; Thermo Scientific, USA) and wired to the LCR meter located outside of the incubator via flexible ACF cables. The data were collected every 2 hours from the e-scaffold system. The frequency responses of the cytotoxic effects were obtained by measuring the impedance of the MCF7 cells treated with different doses of Dox at the frequency of 30 kHz.

5.2.8 Measurement of ECG signals

The ECG signals of the cardiomyocytes were acquired by using the multichannel electrophysiological data acquisition unit (BioRadio, USA) with a notch filter (60 Hz) and a custom filter (Filter type: Bandpass, Filter design: Butterworth, order: 4, lower cutoff: 0.5, upper cutoff: 10). The e-scaffold system was placed in the incubator (5% CO2, 37 °C; Thermo Scientific, USA) and wired to the data acquisition unit via flexible ACF cables. The data were collected at a sample rate of 2 kHz through differential programmable channels and then postprocessed using

commercial software (BioCapture). The solution of norepinephrine bitartrate (10 μM; Sigma-Aldrich, USA) was used to increase the beating rate of the cardiomyocytes.

5.3 Results

5.3.1 Basic configuration of the e-scaffold system

Figure 5.1a shows an exploded schematic view (left) and an optical image (right) of the e-scaffold system afloat on a cell culture medium (Eagle Medium, Gibco). The basic components of the e-scaffold system include (1) multimodal arrays of sensing elements to detect electrical cell–substrate impedance and/or electrophysiological signals, (2) thin films (<1 μm thick) of waterproof polyimide (PI) elastomer to serve as the substrate and encapsulation, (3) high concentration of cold Matrigel (20 mg/mL, Corning) surrounding the entire e-scaffold to serve as the matrix that contains biological cells, (4) flexible anisotropic conductive film (ACF) cables (HST-9805-210, Elform, Inc., USA) to connect the e-scaffold with an external data acquisition unit, and (5) a sheet of highly water-repellent ultrabuoy that consists of microporous spongelike polydimethylsiloxane (PDMS) with an effective specific weight of ~456 kg/m^3 that is >4 times lower than the cell culture medium (~1926 kg/m^3), all anchored to the peripheral area of the e-scaffold. In this configuration, all of the electronic components including the ACF cables, connecting the sensing electrode to the external DAQ system, remain on the top of the spongelike PDMS to avoid wetting, while cells can reside and grow within the e-scaffold attached below the ultra-buoy and submerged within the culture media. To further promote the ultra-flotation capability, the spongelike PDMS is additionally incorporated with polytetrafluoroethylene (PTFE) nanoparticles (NPs, 0.2–5 μm diameter) covered by a thin layer of medical-grade Teflon (AF2400, DuPont, USA), leading to a substantial increase of the buoyancy force and the surface tension by >20 % and >35 %, respectively (Figure 5.1b). This results in ultra-flotation capability allowing the e-scaffold to keep out of the medium even against intentional pressing up to ~51 N/m^2 (Figure 5.1c) while continuously offering favorable environments for both electronics and cells. A series of scanning electron microscope (SEM) images of the sponge-like PDMS appear in Figure 5.1d, highlighting the internal features. Further characterizations of the sponge-like PDMS in terms of the effective specific weight, contact angle, dynamic droplet behavior, and critical immersion weight and depth appear in Figure 5.2, with the summarized results in Table 5.1. Figure 5.3 presents experimental

results showing that the electrical impedance of the e-scaffold system remains nearly unaffected when deployed on the surface of the cell medium in an incubator (Midi CO_2 Incubators, Thermo Scientific, USA) at 37 °C under an atmosphere with 5% of CO_2 over 2 weeks, whereas abrupt reduction of the impedance occurs within a short period of time in the control groups without the microporous sponge-like ultra-buoyant structure and with a conventional encapsulation using untreated (nonporous) PDMS due to short-circuit paths by wetting and penetration of the cell media.

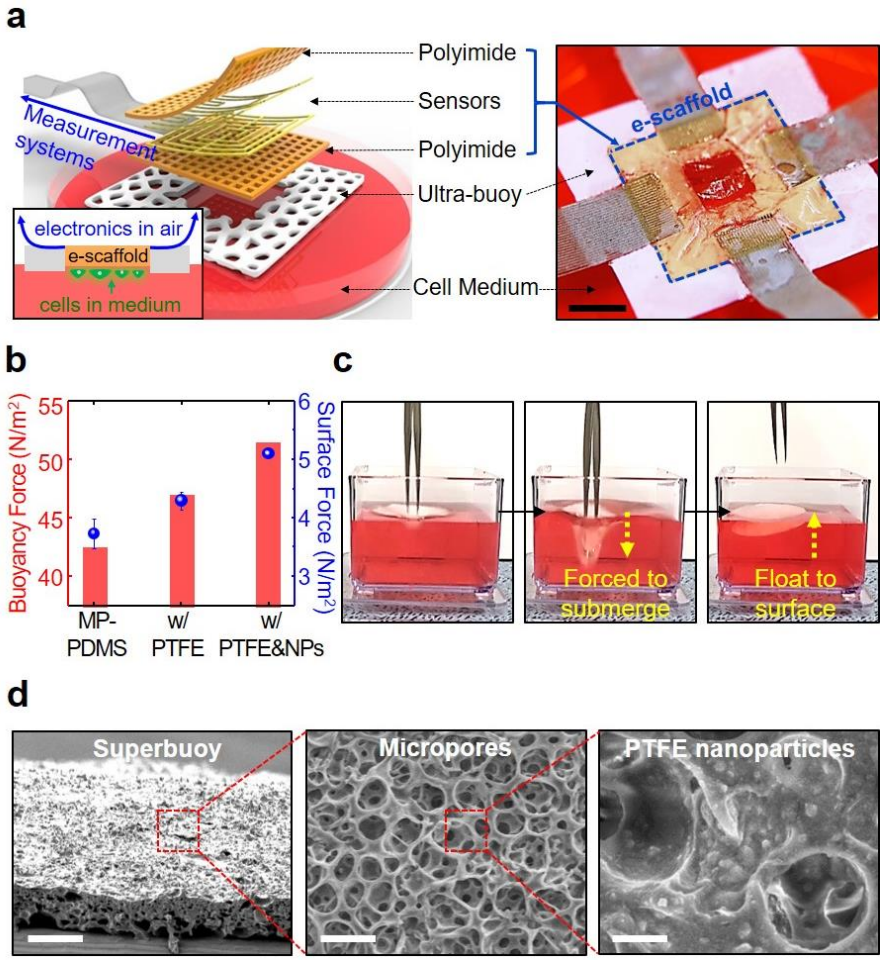

Figure 5.1. Basic configuration of the e-scaffold system. (**a**) An exploded schematic view (left) and an optical image (right) of the e-scaffold system afloat on a cell culture medium. Scale bar is 1 cm. (**b**) Results of the buoyancy and surface tension forces of the e-scaffold system. (**c**) Sequential optical images of microporous sponge-like PDMS coated with Teflon and PTFE NPs floating on a cell culture medium against intentional force. Scale bar is 3 cm. (**d**) SEM images of the microporous sponge-like PDMS. All scale bars are 40 μm.

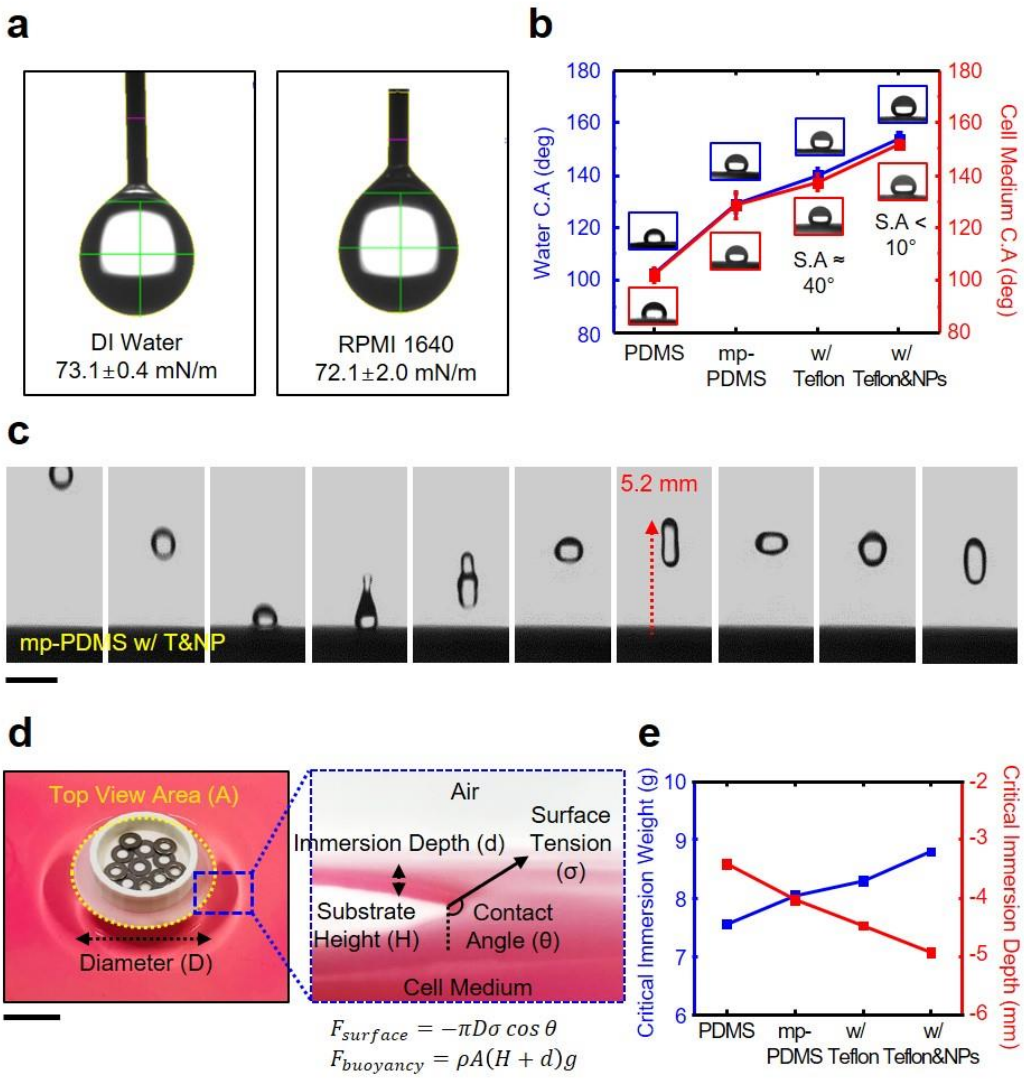

Figure 5.2. (**a**) Theoretical calculation of the effective specific weight of the microporous sponge-like PDMS against control untreated (non-porous) PDMS. (**b**) Summary of the measured surface tension, (**c**) static contact angle, (**d**) dynamic droplet (Scale bar: 2.5 mm), (**e**), (**f**) critical immersion weight and depth (Scale bar: 1 cm).

Table 5.1. Summary of the experimental results for the ultra-hydrophobicity, water-resistance static immersion, and effective specific weight of the sponge-like PDMS

	Cell Medium Contact Angle	Critical Immersion Depth (mm)	Critical Immersion Weight (g)	$F_{surface}$ (N/m^2)	$F_{buoyancy}$ (N/m^2)	Effective Specific Weight (kg/m^3)
PDMS	102.0°±2.6°	-3.4	7.6	1.4±0.3	36.4	965
Sponge-like PDMS	128.7°±4.9°	-4.0	8.1	3.7±0.3	42.4	456
Sponge-like PDMS w/Teflon	137.2°±3.3°	-4.5	8.3	4.3±0.2	46.7	456
Sponge-like PDMS w/Teflon & NPs	151.4°±1.8°	-4.9	8.8	5.1±0.1	51.2	456

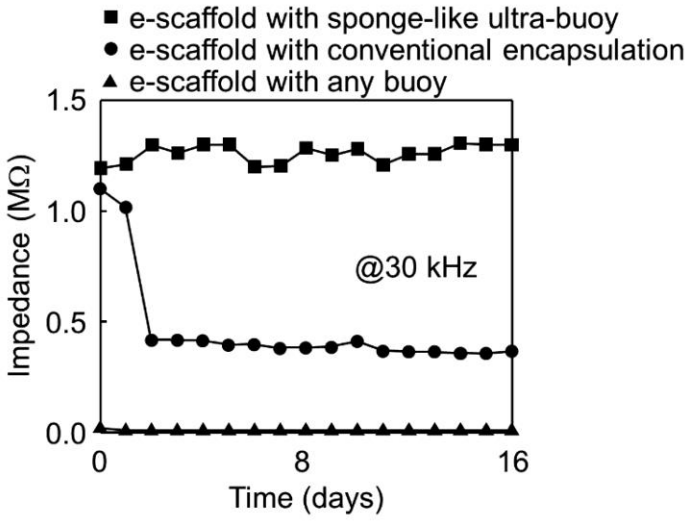

Figure 5.3. Measured impedance of the e-scaffold system over two weeks at 30 kHz signal by comparison with the control groups without the microporous sponge-like ultra-buoy and a conventional encapsulation using untreated (non-porous) PDMS.

5.3.2 Cell compatibility and 3D construction

Cell compatibility of the e-scaffold system is a key consideration for its implementation in 3D cell culture and tissue engineering applications[124-127]. Figure 5.4a (red bars) presents representative results of a cell compatibility assay (MTT, Sigma-Aldrich, USA) for the e-scaffold system seeded with green fluorescent protein (GFP)-expressed MCF7 cells and floated upside down on the medium. Prior to the cell seeding, the e-scaffold system along with the sponge-like PDMS was sterilized with 70 % (v/v) ethanol for 30 min and dried under ultraviolet (UV) irradiation for 1 hours and then stored in an incubator (Midi CO_2 Incubators, Thermo Scientific, USA) at 37 °C

under an atmosphere with 5% of CO_2. The results show that the proliferation rate of the cells increases consistently throughout the assay period (2 days) while displaying no substantial difference compared to those obtained from a control group without any electronics embedded inside (black bars). Figure 5.4b shows the corresponding confocal fluorescence microscope images (A1Rsi confocal microscope, Nikon) of a monolayer of the cells at day 2, wherein the yellow dashed lines indicate the embedded recording electrodes (Au, 150 nm). A control experiment on green immunofluorescence stained cardiomyocyte cells at the 8-day incubation produces consistent results (Figure 5.4c), confirming that the e-scaffold system is conducive to cell growth, proliferation, and extracellular matrix formation. Details about the cell culture and associated experimental procedures appear in the materials and methods section of this chapter.

Another interesting aspect is that the e-scaffold system can be stacked multiple layers within a single Matrigel, providing the desired 3D cell culture environments where cells can grow and interact with the surrounding environment in all dimensions to form tissues for a variety of tissue-engineering applications[124-127]. Figure 5.4d presents pilot data obtained from the four-layer-stacked e-scaffold system surrounded with dense cell (MCF7) layers after the 3-day incubation with the corresponding confocal fluorescence microscope image in Figure 5.4e. The results consistently indicate that the e-scaffold system supports cell growth and tissue formation. Furthermore, alternative stacking of the e-scaffold system seeded with a specific sequence of different cells is possible, thereby yielding a 3D heterocellular structure[128-130]. Figure 5.4f and g shows representative confocal fluorescence microscopy images for the e-scaffold system with alternately stacked cancer cells (e.g., GFP-MCF7) and endothelial cells (e.g., GFP-HUVEC cells). Each cell layer is separately incubated for 2 days under different culture conditions and then stained with DAPI and Draq5 for the MCF7 and HUVEC cells, respectively. The corresponding top view images in Figure 5.5 highlight the confluent layers of the well-attached cells with normal morphologies. The formation of vascular tubes in the HUVEC cells occurs, exhibiting extensive branches with a typical length of 80 μm at day 3 (Figure 5.6). The subsequent treatment of both vascular endothelial growth factor (VEGF) and fibroblast growth factor (β-FGF) remains required to form the tumor vasculature, thereby allowing for more systematic investigations[131,132].

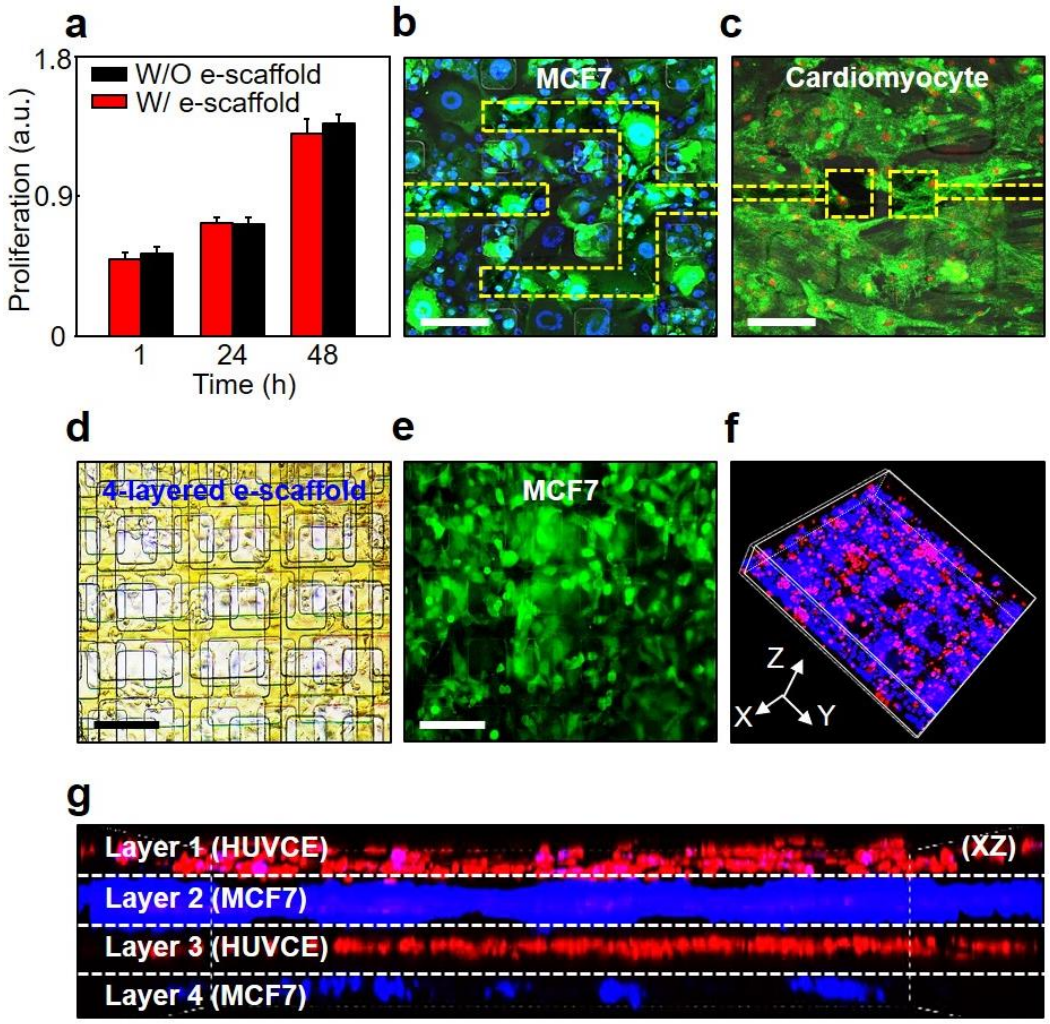

Figure 5.4. 3D construction and the cell compatibility. (**a**) Results of MTT assays for GFP-MCF7 cells seeded on the e-scaffold system. (**b**) Conformal fluorescence microscope image of the monolayer of the GFP-MCF7 cells at the 2-day incubation (green = GFP, blue = DAPI). Scale bar is 100 μm. (**c**) Results of control experiments with green immunofluorescence stained cardiomyocyte cells at the 8-day incubation (green = FITC, red = Draq5). Scale bar is 60 μm. (**d**) Optical image of the 4-layers-stacked e-scaffold system surrounding with dense cell (MCF7) layers after the 3-day incubation. Scale bar is 200 μm. (**e**) Confocal fluorescence microscope image of the stacked e-scaffold system (green = GFP). Scale bar is 200 μm. (**f**) and (**g**) Tilted and side view of the stacked e-scaffold system with alternatively stacked GFP-MCF7 cells and GFP-HUVEC cells (blue = DAPI, red = Draq5).

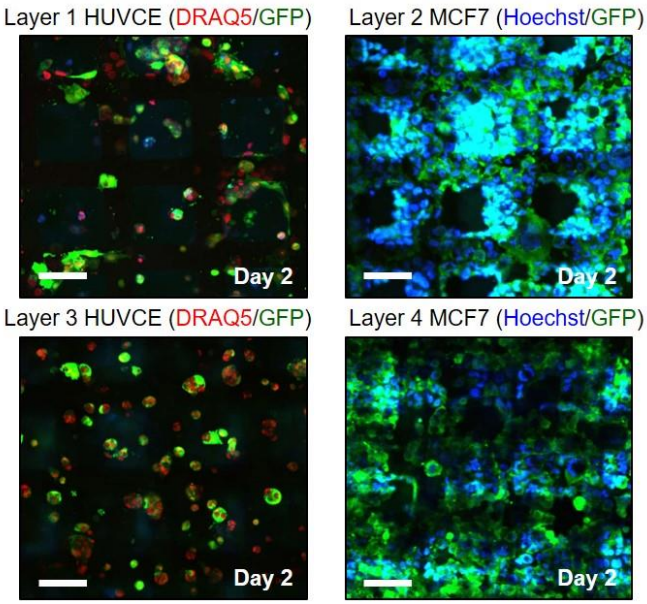

Figure 5.5. Confocal fluorescence microscope images of the GFP-MCF7 and the GFP-HUVEC cells seeded on the four-layers-stacked e-scaffold (green = GFP, red = Draq5 and blue = DAPI). Scale bar is 200 μm.

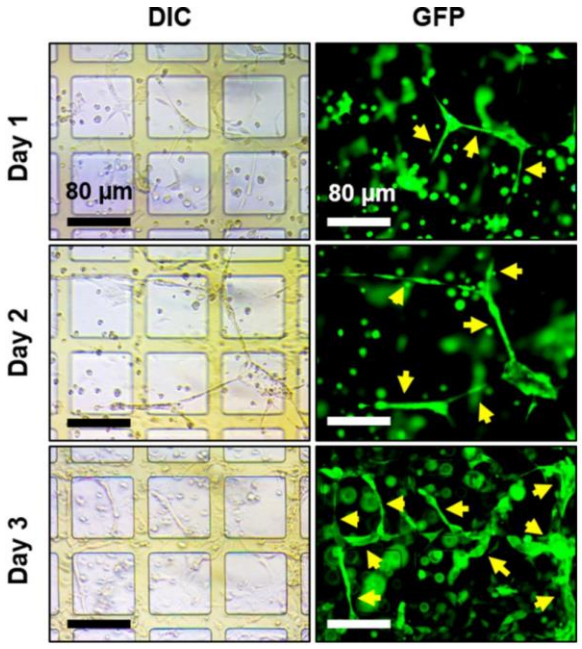

Figure 5.6. DIC (left) and confocal fluorescence microscope images (right) of the endothelial (GFP-HUVEC) vascular tubes formed on the e-scaffold system with the mesh pore size of 100 μm (green = GFP). Yellow arrows represent the formation of the vascular tubes. Scale bars are 80 μm.

5.3.3 Real-time monitoring of electrical cell-substrate impedance

Real-time monitoring of electrical cell–substrate impedance presents a non-labeling technique to understand cellular functions such as adhesion, growth, differentiation, mitigation, and drug effect on cell behaviors[133]. Biological cells serve as dielectric particles due to the insulating properties of their membranes, and therefore, their attachment and detachment affect the current flow between the recording electrodes, leading to distinguishable changes in the impedance values[134]. To illuminate this capability, a model e-scaffold system is constructed into a configuration of interdigitated arrays (width 80 μm, gap 100 μm) of the embedded recording electrodes (Au, 150 nm) for the measurement of electrical impedance (Figure 5.7). The equivalent circuit model appears in Figure 5.8a, showing the recording electrode resistance (R_E), cell culture medium (R_{medium}), Helmholtz double-layer interfacial capacitance (C_I), and additional resistance (R_{cells}) and capacitance (C_{cells}) by the introduction of cells. The recording electrodes act as a normal capacitor wherein the resulting impedance:

$$X_c = \frac{1}{j\omega c}, \qquad c = \frac{(\varepsilon_r \varepsilon_0 A)}{d}$$

is subject to frequency (ω), dielectric constant (ε_r) of the surrounding materials (air = 1.00059, water = 80.4, medium = 80), cross-sectional area of the recording electrode (A = ~3900 μm^2), and gap between the interdigitated arrays (d = 100 μm). A representative frequency–impedance curve of the e-scaffold system at a frequency range of 1–250 kHz appears in Figure 5.8b. Details about the measurement of cellular impedance appear in the Materials and methods section of this chapter.

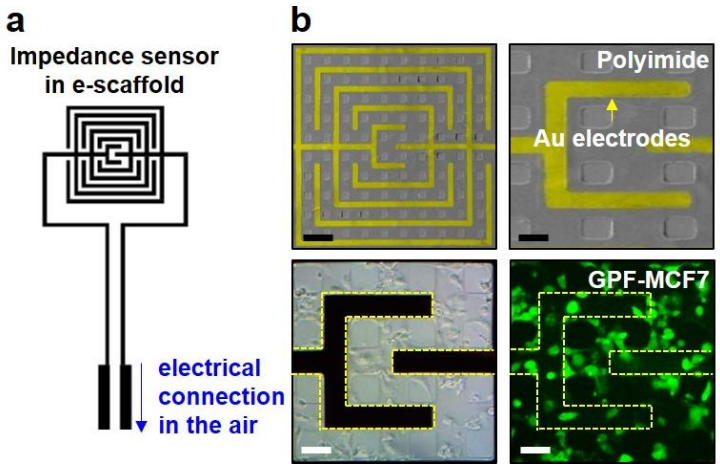

Figure 5.7. (**a**) Schematic illustration of the basic design layout of the impedance sensor embedded in the e-scaffold. (**b**) SEM, DIC, and confocal fluorescence microscope images of the e-scaffold seeded with GFP-MCF7 cells at day 1 (green = GFP). Scale bars are 300 μm, 100 μm, 100 μm, and 100 μm from the top left, top right, bottom left, and bottom right.

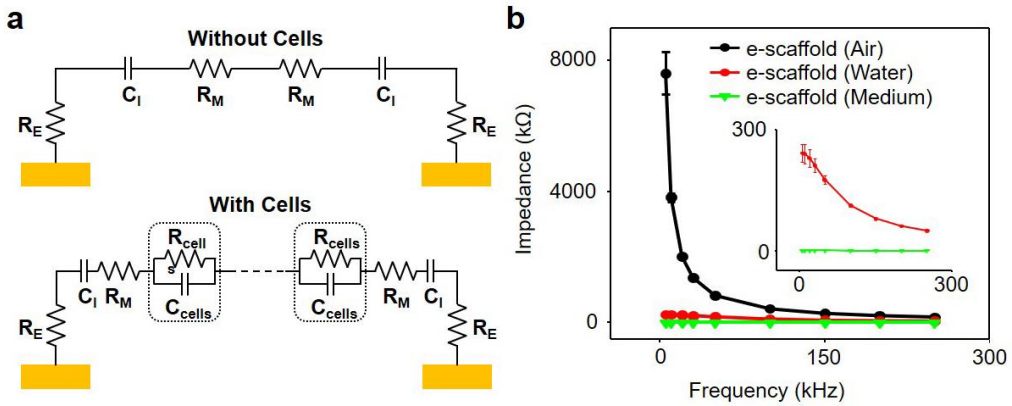

Figure 5.8. (**a**) the equivalent circuits for the impedance sensor without (top) and with (bottom) cells. (**b**) Measured frequency-impedance curve of the e-scaffold at the frequency range of 1-250 kHz.

Figure 5.9a shows representative SEM (left), microscopy (middle), and conformal microcopy (right) images of the model e-scaffold system within a Matrigel seeded with MCF7 cells after 1 h of incubation. The e-scaffold system remains afloat on the medium, wherein the recording electrodes are entirely surrounded by the PI elastomers. The ACF cables placed on the spongelike PDMS are wired to an external data acquisition system (E4980AL Precision LCR meter, Keysight Technologies, USA) through the air. Figure 5.9b shows the results of time-dependent impedance obtained separately from MCF7 cells (black line), SKOV3 cells (red line), and HUVEC cells

(green line) for 50 h during the period of growth and proliferation. The results show that the impedance increases linearly for the first ~4 h when the cells start to settle down and become adherent to the recording electrodes, implying that the cells act as an electrical insulating medium[135]. From ~16 h later, a drastic increase of the impedance occurs due to the cell aggregation and continuous proliferation. This tendency is more obvious in the MCF7 cells because the population doubling time of MCF7 cells (~29 h) is shorter than that of SKOV3 cells (~48 h) and HUVEC cells (~60 h). Consistently, the impedance of the MCF7 cells increases proportionally to the cellular density (Figure 5.9c). An impedimetric cytotoxicity plot for the MCF7 cells appears in Figure 5.9d, while a model drug such as a hydrophilic and water-soluble doxorubicin (Dox, doxorubicin hydrochloride, Fisher, USA, solubility ~50 mg/mL) is introduced in the medium with different dosages at 1-day incubation. The results reveal that the impedance starts to decrease within ~4 h after the drug administration (100 μM) when the effect of the Dox becomes apparent and eventually leads to cell death and detachment. It is observed that no substantial decrease of the impedance appears in the control groups with the low drug administration (10 μM).

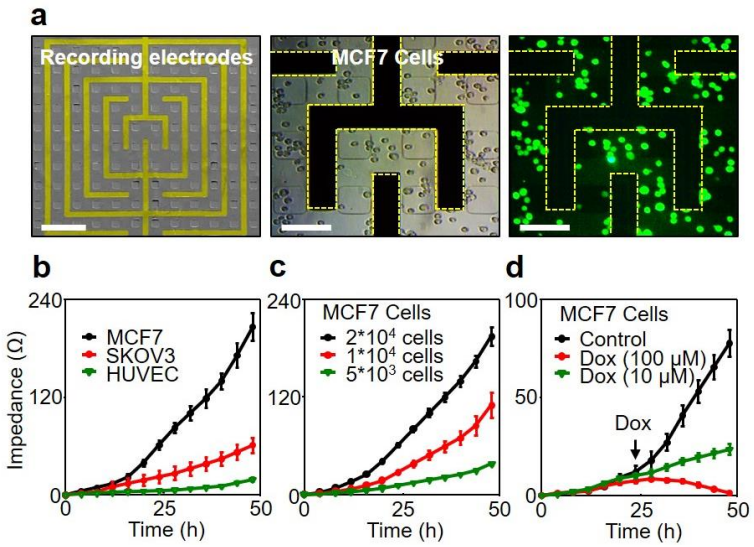

Figure 5.9. Real-time monitoring of electrical cell-substrate impedance. (**a**) Representative SEM (left), microscopy (middle), and conformal microcopy (right) images of the e-scaffold system embedded with impedance sensors (green = GFP). Scale bars are 300 μm, 100 μm and 100 μm from the left. (**b**) Results of the time-dependent impedance for the MCF7 cells (black line), SKOV3 cells (red line), and HUVEC cells (green line) for 50 hrs. (**c**) The corresponding results of the different density of the MCF7 cells. (**d**) Impedimetric cytotoxicity plot for the MCF7 cells with the administration of Dox.

Laminating the e-scaffold systems multiple times provides the capability of monitoring spatially resolved impedance from cultured cells in 3D-structured environments[136]. Figure 5.10a shows a schematic illustration for the three-layer-stacked e-scaffold system within a single Matrigel seeded with MCF7 cells, which is floated upside down on the medium by using the spongelike PDMS. In this configuration, each layer of the e-scaffold system remains spaced apart a fixed distance of ~5 mm along the perimeter by using spacers made of PDMS. Figure 5.10b shows the time-dependent impedance obtained from each layer of the e-scaffold system on the top (black line), middle (red line), and bottom (green line), while 1 mM of Dox is introduced on the uppermost top at the 1-day incubation. The impedance increases at nearly the same rate during the cell growth and proliferation and then abruptly decreases following the drug administration with different rates (top: ~10.1 Ω/h, middle: ~5.4 Ω/h, bottom: ~1.6 Ω/h), as the Dox molecules diffuse downward from the top within the Matrigel. These results are consistent with the confocal fluorescence microscopy images (Figure 5.11) obtained from the top (left image), middle (middle image), and bottom (right image) layer of the e-scaffold system at 12 h after the treatment of Dox (1 mM), indicating that the top layer contains the most Dox, followed by the middle and bottom layers. This platform for the real-time impedimetric analysis of drug-induced cellular events in 3D environments can provide important insights into the mechanism of complex cellular phenomena for the identification of diseased cells at different stages and their interactions with therapeutic agents[137].

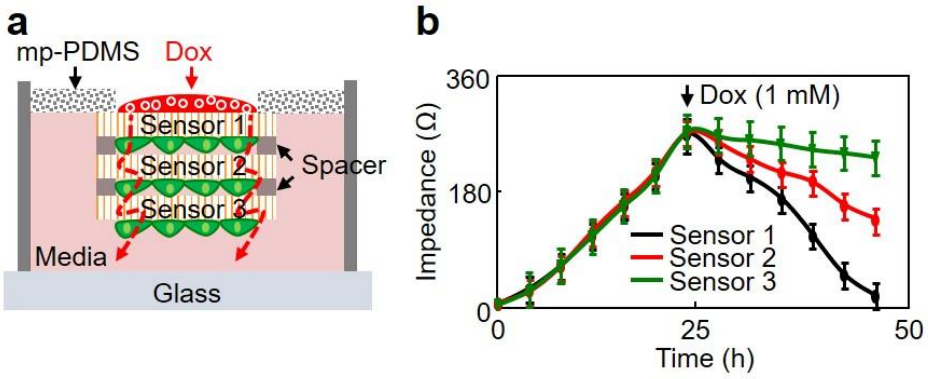

Figure 5.10. (**a**) Schematic illustration for the 3-layers-stacked e-scaffold system within a single matrigel seeded with MCF7 cells. (**b**) Results of the real-time monitoring of the impedances. Data are presented as means ± S.E. (n = 3).

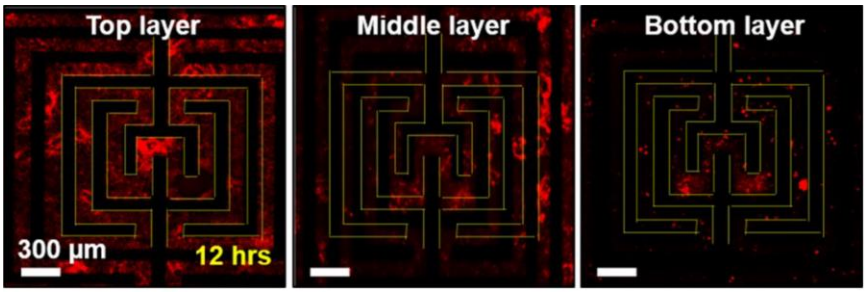

Figure 5.11. Confocal fluorescence microscopy images obtained from the top (left), middle (middle), and bottom (right) layer of the 3-layers-stacked e-scaffold system at 12 hrs after the treatment of Dox (1 mM) (red = hydrophilic doxorubicin). Scale bars are 300 μm.

5.3.4 Real-time 3D monitoring of cardiac action potential

Real-time 3D monitoring of electrophysiological signals in electrically active cells such as the heart, brain, and muscle cells enables spatially resolved quantitative analysis of action potential propagations to understand tissue development, drug modulation, and functions of diseased or damaged tissues[122,138]. To demonstrate the potential use of the e-scaffold system in this context, a model three-layer-stacked e-scaffold system is constructed within a single Matrigel containing cardiomyocytes and tailored for the detection of electrocardiography (ECG) signals. Each layer of the e-scaffold system consists of 36 recording electrodes (Au, 150 nm, width = 60 × 60 μm^2, electrode gap = 10 μm, distance between the recording electrodes = 1150 μm) (Figure 5.12). In this configuration, the monitoring of the cellular contractions occurs on each recording electrode, while the array-type mapping reveals the spatial distributions and variations of the cardiomyocyte throughout the 3D environment. The cardiomyocytes undergo maturation in culture, leading to formation of a tissue layer aligned to the e-scaffold system at day 8 in vitro. The representative immunostained confocal images of cardiomyocytes stained with sarcomeric α-actinin taken from several different areas after 8 days of incubation reveal that cardiomyocytes are homogeneously distributed along the surface and elongated with high aspect ratios, providing information on the maturation of cells and formation of tissues with hallmarks of the native myocardium. As the cardiomyocytes mature, the sarcomeres assemble in series to form myofibrils that extend across the cells wherein the myofibrils are anchored to the ends of the cardiomyocytes by the cell–cell junctional structure.

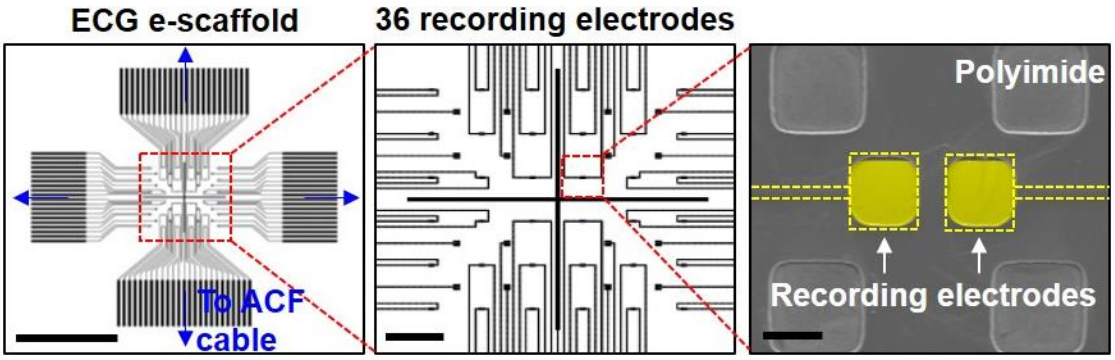

Figure 5.12. Schematic illustrations (left) and SEM image (right) of the e-scaffold system embedded with 36 ECG recording electrodes with the distance between each sensor of 1,150 μm. Scale bars are 1 cm, 1 mm and 40 μm from the left.

Figure 5.13a shows the recorded ECG signals in real time from the cardiomyocytes at the day 2, 6, and 8, exhibiting the typical shape of cardiac action potential signals at frequencies of 4.8, 1, and 0.6 Hz, respectively. The beating rate decreases from 288 to 60 bpm and to 36 bpm, whereas the amplitude increases from 66 to 83 μV and to 511 μV at day 2, 6, and 8, respectively. The results imply that spontaneous contractions of the individual cells initially occur, followed by stronger and more synchronized contractions as the cells become more in contact with each other. Figure 5.13b shows the continuously recorded ECG signals from the cardiomyocytes at day 8 in response to the addition of 100 μL of norepinephrine (NE) into the medium, displaying that the beating rate increases nearly 2-fold within ~3 min after the NE administration. A representative microscopy image in Figure 5.13c highlights the embedded four-channel-multiplexed sensing electrodes with the cardiomyocytes at day 8 within the domain of 1.4 × 1.4 mm^2. The results in Figure 5.13d show the synchronized beating rate (~0.63 Hz), amplitude (638–763 μV), and peak width (~1.6 s), which are within the range of those reported in previous studies[118,122]. The 3D mapping results of the action potentials (Figure 5.13e) obtained from the total 48 ECG sensors (4 × 4 array in each layer) reveal the spontaneous beating activities of the cardiomyocytes at day 2, 6, and 8, without showing any toxic effect.

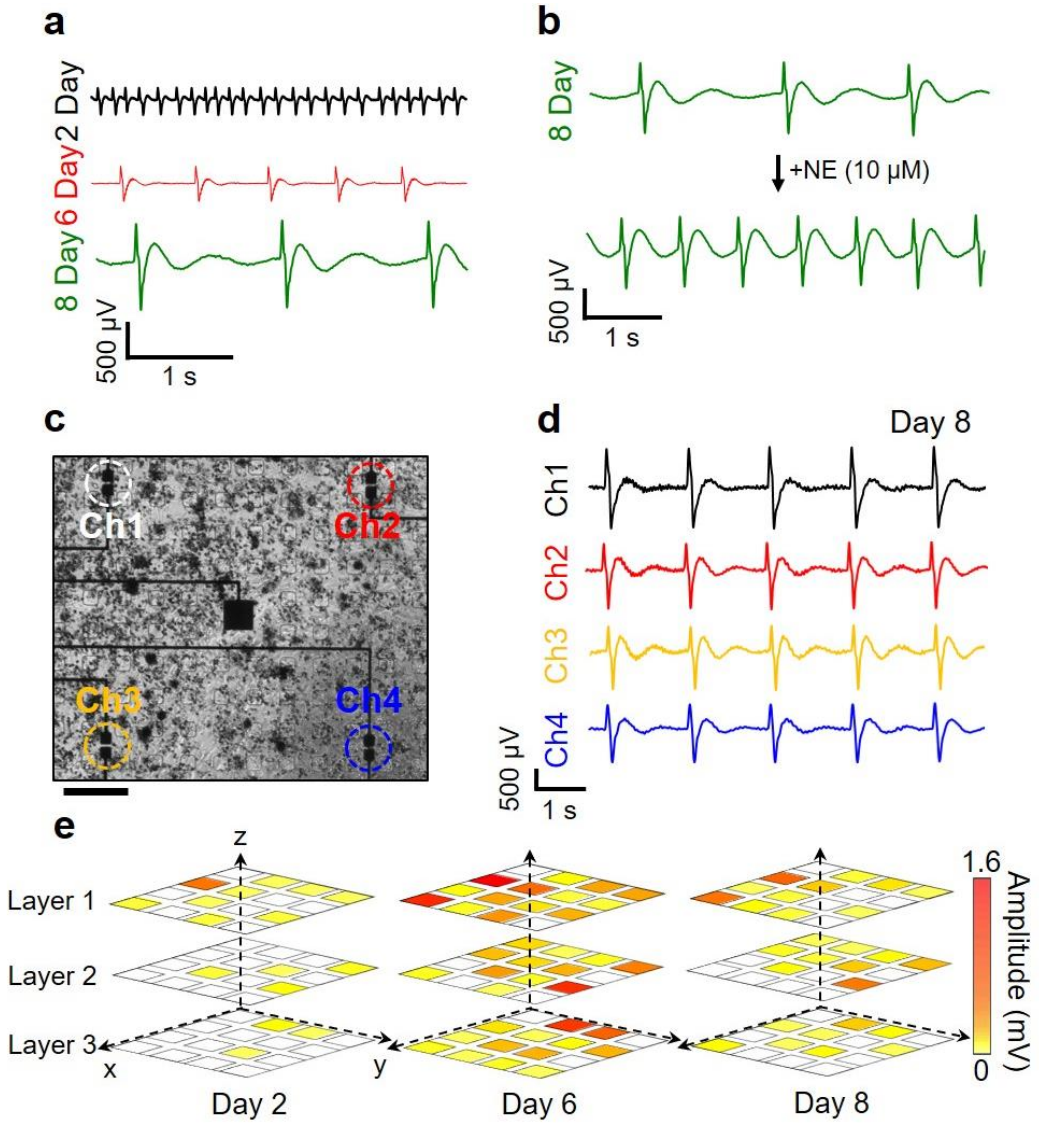

Figure 5.13. 3D mapping of Electrocardiogram. (**a**) Results of the ECG signals recorded from the cardiomyocytes at the day 2, 6, and 8. (**b**) Continuously recorded ECG signals recorded from the cardiomyocytes at the day 8 in response to the addition of 100 μL of norepinephrine (NE) into the medium. (**c**) Representative microscopy image of the embedded 4-channel-multiplexed ECG sensors with cardiomyocytes at the day 8. Scale bar is 200 μm. (**d**) Results for the synchronized beating of the cardiomyocytes at the day 8. (**e**) Results of the 3D mapping of the action potentials of cardiomyocytes at the day 2, 6, and 8 from the left.

5.4 Discussion

The results presented here demonstrate that the e-scaffold integrated with the microporous sponge-like ultra-buoyant structure on medium allows long-term, high-fidelity monitoring of cellular behaviors and functions in favorable environments for both biological cells and electronics. The physical stacking of the e-scaffold system enables the incorporation of large numbers of addressable sensors in a multidirectional arrangement, offering the 3D mapping capability. These findings suggest an expanded set of potential options such as long-term stable monitoring of tissue functions during/after in vivo transplant to replace diseased or damaged tissues[139]. The real-time monitoring of the cellular behaviors and functions with temporal resolutions during endothelial lumen formation in tumor tissue or during the invasion of SKOV3 cells into HUVEC cells to obtain information on their interactions between invading cancer cells and the adherent cells would be highly desired, suggesting directions for future research[140-142]. It might be also interesting to consider constructing a bioresorbable form of the e-scaffold system such that the constituent materials degrade harmlessly in the body following implantation and after a clinically useful period, thereby eliminating the need for postsurgical extraction[143-146]. Although this study focuses on the advantages provided by impedance and electrophysiological sensor, similar systems instrumented with more diverse sensing modalities, such as detection of pH, pressure, temperature, and/or mechanical strains, can be considered[147-149].

5.5 Acknowledgements

The figures, results and manuscript in this chapter is reprinted/adapted with permission from "Sensor-Instrumented Scaffold Integrated with Microporous Spongelike Ultrabuoy for Long-Term 3D Mapping of Cellular Behaviors and Functions" *ACS Nano*, 13, 7, 7898-7904. Copyright 2019 American Chemical Society. I express sincere gratitude to all of the coauthors on this journal publication, Dr. Hyungjun Kim (Purdue University), Hanmin Jang (Hanyang University), Bongjoong Kim (Purdue University), Prof. Dong Rip Kim (Hanyang University) and Prof. Chi Hwan Lee (Purdue University).

6. CONCLUSION AND OUTLOOK

Wearable devices are starting to play a more significant role in areas of medical engineering and transforming healthcare. More and more applications are beginning to utilize smart data science algorithm to analyze data from multitude of biosensors and trying to gain meaningful interpretation of the biosignal and processes. However, such smart systems can only be built upon reliable, high quality data. To achieve high fidelity data acquisition, wearable devices must be imperceptible and make conformal contact with the target by overcoming the mechanical mismatch between the device and the tissue. Therefore, careful considerations in materials selection, design strategies and fabrication methods are required. Devices presented in this dissertation were a study into constructing robust and reliable wearable devices for different applications with various physical challenges and constraints and to serve as a platform for further development of wearable devices.

Chapter 2, looked into design strategies on how to design a sensor patch targeted towards a geometrically complex curvilinear area of the body like the submental area for the monitoring of swallowing function in dysphagia. Initial device was constructed from a thin film but the cost of single device was too high and it was too difficult for the clinicians and patients to use. An engineering solution was to utilize a commercially available polyimide/copper clad substrate processed by rapid prototyping method. The thicker substrate was much more durable allowing greater usability while maintaining necessary stretchability when fabricated into a hexagon mesh. The honeycomb hexagon mesh feature was able to effectively distribute the stress during mounting and peeling off process to ensure multiple reusability without device failure. Wireless submental sensor patch integrated with sEMG and strain sensor demonstrated it potential in telerehabilitation of swallow disorder. Adoption of machine learning in signal analysis in future research can be greatly beneficial to clinicians and to patients.

Chapter 3 was an investigation into the design and integration of multimodal sensor array on a geometrically challenging area like the hand where it constantly under dynamic stresses from repeated stretching and folding. The initial challenges of the glove sensor were identifying and constructing each type of sensors and how to integrate them in a monolithic manner with human-

like encapsulation outer layer. A combination of batch process fabrication techniques was used to construct the electronic glove. The prefabricated sensors were transfer-printed to a predetermined location. Then, the interconnecting traces and joule heating element were constructed using a screen-printing method. The electronic glove was able to collect pressure, temperature, and hydration data from the hand area and demonstrated human-like appearance, texture and warmth. The sensory information was displayed on the watch unit or wirelessly transmit the data for simple visual feedback. Electronic glove can serve as a platform in future research into integration with a smart robotic prosthetic or augmented reality.

Chapter 4 was an investigation into the soft handling of delicate biomaterials and bioelectronics, eliminating the need for sacrificial or carrier layer. A thermally triggered hydrogel was fabricated with vertically aligned microchannels which acts like suction cups providing adhesion in wet and dry conditions. A thin film joule heater was fabricated to ensure uniform heat distribution upon activation. The soft manipulator was able to transport thin and delicate bioelectronics and transplant biomaterials like cell sheets. The ease scalability in fabricating the soft manipulator, future research may focus in large area capability to transport entire wafer scale devices or even be used in large area skin graft transplant.

Chapter 5 was a study into integrating a stretchable sensor platform within the 3D scaffold to monitor cell behavior during proliferation. However, wet cell culture environment was unfavorable to electrical components which resulted in poor signal acquisition. Mounting the 3D scaffold sensor on to a superhydrophobic buoy lifted the electrical connections out of the wet environment ensured long term measurement stability. An array of differential pair recording electrodes distributed within the scaffold allowed 3D mapping of cell proliferation and cardiomyocyte electrocardiogram. Future research into fabricating the scaffold sensor with bioresorbable materials can serve as a platform for applications such as wound monitoring.

Despite recent achievements, common fundamental challenges still remain with the current devices such as compatible power source (battery or wireless), integration of rigid electronic, and power requirement for high bandwidth wireless data transmission. More importantly, commonly

used materials like PDMS, polyimide, copper and gold (higher modulus compared to the tissue) still require special design scheme to bridge the mechanical mismatch with the skin.

Looking at the larger picture, current commercial wearable devices have integrated of various sensors which are independent from each other. For the wearable system to provide more comprehensive health information and determine more selective and specific detection of physiological conditions, smart technologies such as big data, machine learning and artificial intelligence should be adopted to analyze the data and make data driven decisions based on a combination of information from the body. In order to achieve such goal, future researches in wearable devices should focus on making every component truly imperceptible and allowing seamless integration with the human body.

REFERENCES

1 Wang, S., Oh, J. Y., Xu, J., Tran, H. & Bao, Z. Skin-inspired electronics: an emerging paradigm. *Accounts of chemical research* **51**, 1033-1045 (2018).

2 Wang, X. *et al.* Recent progress in electronic skin. *Advanced Science* **2**, 1500169 (2015).

3 Lee, C. H. Smart assembly for soft bioelectronics. *IEEE Potentials* **35**, 9-13 (2016).

4 Chortos, A. & Bao, Z. Skin-inspired electronic devices. *Materials Today* **17**, 321-331 (2014).

5 Dang, W., Vinciguerra, V., Lorenzelli, L. & Dahiya, R. Printable stretchable interconnects. *Flexible and Printed Electronics* **2**, 013003 (2017).

6 Won, S. M. *et al.* Recent advances in materials, devices, and systems for neural interfaces. *Advanced Materials* **30**, 1800534 (2018).

7 Lee, Y. *et al.* Wearable sensing systems with mechanically soft assemblies of nanoscale materials. *Advanced Materials Technologies* **2**, 1700053 (2017).

8 Dolbashid, A. S., Mokhtar, M. S., Muhamad, F. & Ibrahim, F. Potential applications of human artificial skin and electronic skin (e-skin): a review. *Bioinspired, Biomimetic and Nanobiomaterials* **7**, 53-64 (2017).

9 Kim, D.-H. *et al.* Epidermal electronics. *science* **333**, 838-843 (2011).

10 Perlman, A. L., Palmer, P. M., McCulloch, T. M. & Vandaele, D. J. Electromyographic activity from human laryngeal, pharyngeal, and submental muscles during swallowing. *Journal of Applied Physiology* **86**, 1663-1669, doi:10.1152/jappl.1999.86.5.1663 (1999).

11 Sörös, P., Inamoto, Y. & Martin, R. E. Functional brain imaging of swallowing: An activation likelihood estimation meta-analysis. *Human Brain Mapping* **30**, 2426-2439, doi:https://doi.org/10.1002/hbm.20680 (2009).

12 Malandraki, G. A., Sutton, B. P., Perlman, A. L., Karampinos, D. C. & Conway, C. Neural activation of swallowing and swallowing-related tasks in healthy young adults: An attempt to separate the components of deglutition. *Human Brain Mapping* **30**, 3209-3226, doi:https://doi.org/10.1002/hbm.20743 (2009).

13 Bhattacharyya, N. The Prevalence of Dysphagia among Adults in the United States. *Otolaryngology–Head and Neck Surgery* **151**, 765-769, doi:10.1177/0194599814549156 (2014).

14 Bhattacharyya, N. The prevalence of pediatric voice and swallowing problems in the United States. *The Laryngoscope* **125**, 746-750, doi:https://doi.org/10.1002/lary.24931 (2015).

15 Hutcheson, K. A. *et al.* Late dysphagia after radiotherapy-based treatment of head and neck cancer. *Cancer* **118**, 5793-5799, doi:https://doi.org/10.1002/cncr.27631 (2012).

16 Rofes, L., Vilardell, N. & Clavé, P. Post-stroke dysphagia: progress at last. *Neurogastroenterology & Motility* **25**, 278-282, doi:https://doi.org/10.1111/nmo.12112 (2013).

17 Langmore, S. E., Skarupski, K. A., Park, P. S. & Fries, B. E. Predictors of Aspiration Pneumonia in Nursing Home Residents. *Dysphagia* **17**, 298-307, doi:10.1007/s00455-002-0072-5 (2002).

18 Baijens, L. W. *et al.* European Society for Swallowing Disorders - European Union Geriatric Medicine Society white paper: oropharyngeal dysphagia as a geriatric syndrome. *Clin Interv Aging* **11**, 1403-1428, doi:10.2147/CIA.S107750 (2016).

19 Crary, M. A., Carnaby, G. D., LaGorio, L. A. & Carvajal, P. J. Functional and Physiological Outcomes from an Exercise-Based Dysphagia Therapy: A Pilot Investigation of the McNeill Dysphagia Therapy Program. *Archives of Physical Medicine and Rehabilitation* **93**, 1173-1178, doi:https://doi.org/10.1016/j.apmr.2011.11.008 (2012).

20 Robbins, J. *et al.* The Effects of Lingual Exercise in Stroke Patients With Dysphagia. *Archives of Physical Medicine and Rehabilitation* **88**, 150-158, doi:https://doi.org/10.1016/j.apmr.2006.11.002 (2007).

21 Martin-Harris, B. *et al.* Respiratory-Swallow Training in Patients With Head and Neck Cancer. *Archives of Physical Medicine and Rehabilitation* **96**, 885-893, doi:https://doi.org/10.1016/j.apmr.2014.11.022 (2015).

22 Malandraki, G. A. *et al.* The Intensive Dysphagia Rehabilitation Approach Applied to Patients With Neurogenic Dysphagia: A Case Series Design Study. *Archives of Physical Medicine and Rehabilitation* **97**, 567-574, doi:https://doi.org/10.1016/j.apmr.2015.11.019 (2016).

23 Krekeler, B. N., Broadfoot, C. K., Johnson, S., Connor, N. P. & Rogus-Pulia, N. Patient Adherence to Dysphagia Recommendations: A Systematic Review. *Dysphagia* **33**, 173-184, doi:10.1007/s00455-017-9852-9 (2018).

24 Shieh, W.-Y., Wang, C.-M. & Chang, C.-S. Development of a Portable Non-Invasive Swallowing and Respiration Assessment Device. *Sensors* **15**, 12428-12453 (2015).

25 Sazonov, E. *et al.* Non-invasive monitoring of chewing and swallowing for objective quantification of ingestive behavior. *Physiological Measurement* **29**, 525-541, doi:10.1088/0967-3334/29/5/001 (2008).

26 Ono, T., Hori, K., Masuda, Y. & Hayashi, T. Recent Advances in Sensing Oropharyngeal Swallowing Function in Japan. *Sensors* **10**, 176-202 (2010).

27 Tajitsu, Y. *et al.* Application of piezoelectric braided cord to dysphagia-detecting system. *Japanese Journal of Applied Physics* **57**, 11UG02, doi:10.7567/jjap.57.11ug02 (2018).

28 Lee, Y. *et al.* Soft Electronics Enabled Ergonomic Human-Computer Interaction for Swallowing Training. *Scientific Reports* **7**, 46697, doi:10.1038/srep46697 (2017).

29 Constantinescu, G. *et al.* Epidermal electronics for electromyography: An application to swallowing therapy. *Medical Engineering & Physics* **38**, 807-812, doi:https://doi.org/10.1016/j.medengphy.2016.04.023 (2016).

30 Gibson, L. J. Cellular Solids. *MRS Bulletin* **28**, 270-274, doi:10.1557/mrs2003.79 (2003).

31 Liu, B., Feng, X. & Zhang, S.-M. The effective Young's modulus of composites beyond the Voigt estimation due to the Poisson effect. *Composites Science and Technology* **69**, 2198-2204, doi:https://doi.org/10.1016/j.compscitech.2009.06.004 (2009).

32 Zhang, Y. Extended Stoney's Formula for a Film-Substrate Bilayer With the Effect of Interfacial Slip. *Journal of Applied Mechanics* **75**, doi:10.1115/1.2745387 (2008).

33 Liu, L. *et al.* Silicone-based adhesives for long-term skin application: cleaning protocols and their effect on peel strength. *Biomedical Physics & Engineering Express* **4**, 015004, doi:10.1088/2057-1976/aa91fb (2017).

34 Hedayati, R., Sadighi, M., Mohammadi Aghdam, M. & Zadpoor, A. A. Mechanical Properties of Additively Manufactured Thick Honeycombs. *Materials* **9**, 613 (2016).

35 Stepp, C. E. Surface Electromyography for Speech and Swallowing Systems: Measurement, Analysis, and Interpretation. *Journal of Speech, Language, and Hearing Research* **55**, 1232-1246, doi:doi:10.1044/1092-4388(2011/11-0214) (2012).

36 Dzedzickis, A. *et al.* Polyethylene-Carbon Composite (Velostat®) Based Tactile Sensor. *Polymers* **12**, 2905 (2020).

37 Lee, C. H. *et al.* Soft Core/Shell Packages for Stretchable Electronics. *Advanced Functional Materials* **25**, 3698-3704, doi:https://doi.org/10.1002/adfm.201501086 (2015).

38 Vafaiee, M., Vossoughi, M., Mohammadpour, R. & Sasanpour, P. Gold-Plated Electrode with High Scratch Strength for Electrophysiological Recordings. *Scientific Reports* **9**, 2985, doi:10.1038/s41598-019-39138-w (2019).

39 Mazzarello, V., Ferrari, M. & Ena, P. Werner syndrome: quantitative assessment of skin aging. *Clin Cosmet Investig Dermatol* **11**, 397-402, doi:10.2147/CCID.S167942 (2018).

40 Jang, K. I. *et al.* Soft network composite materials with deterministic and bio-inspired designs. *Nat Commun* **6**, 6566, doi:10.1038/ncomms7566 (2015).

41 Taylor, C. M., Smith, C. W., Miller, W. & Evans, K. E. The effects of hierarchy on the in-plane elastic properties of honeycombs. *International Journal of Solids and Structures* **48**, 1330-1339, doi:https://doi.org/10.1016/j.ijsolstr.2011.01.017 (2011).

42 Mousanezhad, D. *et al.* Elastic properties of chiral, anti-chiral, and hierarchical honeycombs: A simple energy-based approach. *Theoretical and Applied Mechanics Letters* **6**, 81-96, doi:https://doi.org/10.1016/j.taml.2016.02.004 (2016).

43 Liu, Y. P. & Hu, H. A review on auxetic structures and polymeric materials. *Sci. Res. Essays* **5**, 1052-1063 (2010).

44 Takahashi, T., Takei, K., Gillies, A. G., Fearing, R. S. & Javey, A. Carbon Nanotube Active-Matrix Backplanes for Conformal Electronics and Sensors. *Nano Letters* **11**, 5408-5413, doi:10.1021/nl203117h (2011).

45 Kim, J. *et al.* Stretchable silicon nanoribbon electronics for skin prosthesis. *Nature Communications* **5**, 5747, doi:10.1038/ncomms6747 (2014).

46 Fan, J. A. *et al.* Fractal design concepts for stretchable electronics. *Nature Communications* **5**, 3266, doi:10.1038/ncomms4266 (2014).

47 Wheeler-Hegland, K. M., Rosenbek, J. C. & Sapienza, C. M. Submental sEMG and Hyoid Movement During Mendelsohn Maneuver, Effortful Swallow, and Expiratory Muscle Strength Training. *Journal of Speech, Language, and Hearing Research* **51**, 1072-1087, doi:doi:10.1044/1092-4388(2008/07-0016) (2008).

48 Li, Q. *et al.* Development of a System to Monitor Laryngeal Movement during Swallowing Using a Bend Sensor. *PLOS ONE* **8**, e70850, doi:10.1371/journal.pone.0070850 (2013).

49 Doeltgen, S. H., Ong, E., Scholten, I., Cock, C. & Omari, T. Biomechanical Quantification of Mendelsohn Maneuver and Effortful Swallowing on Pharyngoesophageal Function. *Otolaryngology–Head and Neck Surgery* **157**, 816-823, doi:10.1177/0194599817708173 (2017).

50 McCullough, G. H. *et al.* Effects of Mendelsohn Maneuver on Measures of Swallowing Duration Post Stroke. *Topics in Stroke Rehabilitation* **19**, 234-243, doi:10.1310/tsr1903-234 (2012).

51 Athukorala, R. P., Jones, R. D., Sella, O. & Huckabee, M.-L. Skill Training for Swallowing Rehabilitation in Patients With Parkinson's Disease. *Archives of Physical Medicine and Rehabilitation* **95**, 1374-1382, doi:https://doi.org/10.1016/j.apmr.2014.03.001 (2014).

52 Clark, H. M. Neuromuscular Treatments for Speech and Swallowing. *American Journal of Speech-Language Pathology* **12**, 400-415, doi:doi:10.1044/1058-0360(2003/086) (2003).

53 Wang, C.-M., Shieh, W.-Y., Weng, Y.-H., Hsu, Y.-H. & Wu, Y.-R. Non-invasive assessment determine the swallowing and respiration dysfunction in early Parkinson's disease. *Parkinsonism & Related Disorders* **42**, 22-27, doi:https://doi.org/10.1016/j.parkreldis.2017.05.024 (2017).

54 Kantarcigil, C. & Malandraki, G. A. First Step in Telehealth Assessment: A Randomized Controlled Trial to Investigate the Effectiveness of an Electronic Case History Form for Dysphagia. *Dysphagia* **32**, 548-558, doi:10.1007/s00455-017-9798-y (2017).

55 Kantarcigil, C., Sheppard, J. J., Gordon, A. M., Friel, K. M. & Malandraki, G. A. A telehealth approach to conducting clinical swallowing evaluations in children with cerebral palsy. *Research in Developmental Disabilities* **55**, 207-217, doi:https://doi.org/10.1016/j.ridd.2016.04.008 (2016).

56 Chung, D. S., Wettroth, C., Hallett, M. & Maurer, C. W. Functional Speech and Voice Disorders: Case Series and Literature Review. *Movement Disorders Clinical Practice* **5**, 312-316, doi:https://doi.org/10.1002/mdc3.12609 (2018).

57 Mckechnie, P. & John, A. Anxiety and depression following traumatic limb amputation: a systematic review. *Injury* **45**, 1859-1866 (2014).

58 Grob, M., Papadopulos, N., Zimmermann, A., Biemer, E. & Kovacs, L. The psychological impact of severe hand injury. *Journal of Hand Surgery (European Volume)* **33**, 358-362 (2008).

59 Gallagher, P. & Desmond, D. Measuring quality of life in prosthetic practice: benefits and challenges. *Prosthetics and orthotics international* **31**, 167-176 (2007).

60 Cabibihan, J.-J., Pattofatto, S., Jomâa, M., Benallal, A. & Carrozza, M. C. Towards humanlike social touch for sociable robotics and prosthetics: Comparisons on the compliance, conformance and hysteresis of synthetic and human fingertip skins. *International Journal of Social Robotics* **1**, 29-40 (2009).

61 Cordella, F. *et al.* Literature review on needs of upper limb prosthesis users. *Frontiers in neuroscience* **10**, 209 (2016).

62 Kim, J. *et al.* Stretchable silicon nanoribbon electronics for skin prosthesis. *Nature communications* **5**, 1-11 (2014).

63 Wang, S. *et al.* Skin electronics from scalable fabrication of an intrinsically stretchable transistor array. *Nature* **555**, 83-88 (2018).

64 Kaltenbrunner, M. *et al.* An ultra-lightweight design for imperceptible plastic electronics. *Nature* **499**, 458-463 (2013).

65 Chossat, J.-B., Shin, H.-S., Park, Y.-L. & Duchaine, V. Soft tactile skin using an embedded ionic liquid and tomographic imaging. *Journal of mechanisms and robotics* **7** (2015).

66 Chortos, A., Liu, J. & Bao, Z. Pursuing prosthetic electronic skin. *Nature materials* **15**, 937-950 (2016).

67 Ota, H. *et al.* Application of 3D printing for smart objects with embedded electronic sensors and systems. *Advanced Materials Technologies* **1**, 1600013 (2016).

68 Mishra, R. K. *et al.* Wearable flexible and stretchable glove biosensor for on-site detection of organophosphorus chemical threats. *ACS sensors* **2**, 553-561 (2017).

69 Boley, J. W., White, E. L. & Kramer, R. K. Mechanically sintered gallium–indium nanoparticles. *Advanced Materials* **27**, 2355-2360 (2015).

70 Lee, P. *et al.* Highly stretchable and highly conductive metal electrode by very long metal nanowire percolation network. *Advanced materials* **24**, 3326-3332 (2012).

71 Carlson, A., Bowen, A. M., Huang, Y., Nuzzo, R. G. & Rogers, J. A. Transfer printing techniques for materials assembly and micro/nanodevice fabrication. *Advanced Materials* **24**, 5284-5318 (2012).

72 Kim, S. *et al.* Microstructured elastomeric surfaces with reversible adhesion and examples of their use in deterministic assembly by transfer printing. *Proceedings of the National Academy of Sciences* **107**, 17095-17100 (2010).

73 Wie, D. S. *et al.* Wafer-recyclable, environment-friendly transfer printing for large-scale thin-film nanoelectronics. *Proceedings of the National Academy of Sciences* **115**, E7236-E7244 (2018).

74 Lee, C. H. *et al.* Soft core/shell packages for stretchable electronics. *Advanced Functional Materials* **25**, 3698-3704 (2015).

75 Heikenfeld, J. *et al.* Wearable sensors: modalities, challenges, and prospects. *Lab on a Chip* **18**, 217-248 (2018).

76 Han, S. *et al.* Mechanically reinforced skin-electronics with networked nanocomposite elastomer. *Advanced Materials* **28**, 10257-10265 (2016).

77 Kim, D. H. *et al.* Optimized structural designs for stretchable silicon integrated circuits. *Small* **5**, 2841-2847 (2009).

78 Ellis, M. V. Repeated measures designs. *The Counseling Psychologist* **27**, 552-578 (1999).

79 Mauchly, J. W. Significance test for sphericity of a normal n-variate distribution. *The Annals of Mathematical Statistics* **11**, 204-209 (1940).

80 Norušis, M. J. *SPSS 14.0 guide to data analysis*. (Prentice Hall Upper Saddle River, NJ, 2006).

81 Cipriani, C. *et al.* A novel concept for a prosthetic hand with a bidirectional interface: a feasibility study. *IEEE Transactions on Biomedical Engineering* **56**, 2739-2743 (2009).

82 Moran, C. W. Revolutionizing prosthetics 2009 modular prosthetic limb-body interface: Overview of the prosthetic socket development. *Johns Hopkins APL Technical Digest* **30**, 250-255 (2011).

83 Hutchinson, D. T. The quest for the bionic arm. *JAAOS-Journal of the American Academy of Orthopaedic Surgeons* **22**, 346-351 (2014).

84 Raspopovic, S. *et al.* Restoring natural sensory feedback in real-time bidirectional hand prostheses. *Science translational medicine* **6**, 222ra219-222ra219 (2014).

85 Tabot, G. A. *et al.* Restoring the sense of touch with a prosthetic hand through a brain interface. *Proceedings of the National Academy of Sciences* **110**, 18279-18284 (2013).

86 Gurari, N., Kuchenbecker, K. J. & Okamura, A. M. Perception of springs with visual and proprioceptive motion cues: Implications for prosthetics. *IEEE Transactions on Human-Machine Systems* **43**, 102-114 (2012).

87 Yang, J. *et al.* Cell sheet engineering: recreating tissues without biodegradable scaffolds. *Biomaterials* **26**, 6415-6422 (2005).

88 Yang, J. *et al.* Reconstruction of functional tissues with cell sheet engineering. *Biomaterials* **28**, 5033-5043 (2007).

89 Nishida, K. *et al.* Functional bioengineered corneal epithelial sheet grafts from corneal stem cells expanded ex vivo on a temperature-responsive cell culture surface. *Transplantation* **77**, 379-385 (2004).

90 Sekine, H. *et al.* In vitro fabrication of functional three-dimensional tissues with perfusable blood vessels. *Nature communications* **4**, 1-10 (2013).

91 Kim, D.-H. *et al.* Electronic sensor and actuator webs for large-area complex geometry cardiac mapping and therapy. *Proceedings of the National Academy of Sciences* **109**, 19910-19915 (2012).

92 Tian, L. *et al.* Large-area MRI-compatible epidermal electronic interfaces for prosthetic control and cognitive monitoring. *Nature biomedical engineering* **3**, 194-205 (2019).

93 Jeong, J. W. *et al.* Materials and optimized designs for human-machine interfaces via epidermal electronics. *Advanced Materials* **25**, 6839-6846 (2013).

94 De, S. *et al.* Assessment of tissue damage due to mechanical stresses. *The International Journal of Robotics Research* **26**, 1159-1171 (2007).

95 Liang, X. *et al.* Toward clean and crackless transfer of graphene. *ACS nano* **5**, 9144-9153 (2011).

96 Yan, Z. *et al.* Thermal Release Transfer Printing for Stretchable Conformal Bioelectronics. *Advanced Science* **4**, 1700251, doi:https://doi.org/10.1002/advs.201700251 (2017).

97 Baik, S. *et al.* A wet-tolerant adhesive patch inspired by protuberances in suction cups of octopi. *Nature* **546**, 396-400, doi:10.1038/nature22382 (2017).

98 Lee, H. *et al.* Octopus-Inspired Smart Adhesive Pads for Transfer Printing of Semiconducting Nanomembranes. *Advanced Materials* **28**, 7457-7465, doi:https://doi.org/10.1002/adma.201601407 (2016).

99 Choi, M. K. *et al.* Cephalopod-Inspired Miniaturized Suction Cups for Smart Medical Skin. *Advanced Healthcare Materials* **5**, 80-87, doi:https://doi.org/10.1002/adhm.201500285 (2016).

100 Kier, W. M. & Smith, A. M. The Structure and Adhesive Mechanism of Octopus Suckers1. *Integrative and Comparative Biology* **42**, 1146-1153, doi:10.1093/icb/42.6.1146 (2002).

101 Tramacere, F. *et al.* The Morphology and Adhesion Mechanism of Octopus vulgaris Suckers. *PLOS ONE* **8**, e65074, doi:10.1371/journal.pone.0065074 (2013).

102 Wirthl, D. *et al.* Instant tough bonding of hydrogels for soft machines and electronics. *Science Advances* **3**, e1700053, doi:10.1126/sciadv.1700053 (2017).

103 Wang, Z. *et al.* Spatial light interference microscopy (SLIM). *Opt. Express* **19**, 1016-1026, doi:10.1364/OE.19.001016 (2011).

104 Kim, J., Cho, Y., Kim, S. & Lee, J. 3D Cocontinuous Composites of Hydrophilic and Hydrophobic Soft Materials: High Modulus and Fast Actuation Time. *ACS Macro Letters* **6**, 1119-1123, doi:10.1021/acsmacrolett.7b00642 (2017).

105 Bai, H., Polini, A., Delattre, B. & Tomsia, A. P. Thermoresponsive Composite Hydrogels with Aligned Macroporous Structure by Ice-Templated Assembly. *Chemistry of Materials* **25**, 4551-4556, doi:10.1021/cm4025827 (2013).

106 Gao, P., Nixon, P. R. & Skoug, J. W. Diffusion in HPMC gels. II. Prediction of drug release rates from hydrophilic matrix extended-release dosage forms. *Pharmaceutical research* **12**, 965-971 (1995).

107 Tananuvat, N. *et al.* Limbal stem cell and oral mucosal epithelial transplantation from ex vivo cultivation in LSCD-induced rabbits: histology and immunologic study of the transplant epithelial sheet. *International Ophthalmology* **37**, 1289-1298, doi:10.1007/s10792-016-0402-5 (2017).

108 Prabhasawat, P. *et al.* Long-term result of autologous cultivated oral mucosal epithelial transplantation for severe ocular surface disease. *Cell and Tissue Banking* **17**, 491-503, doi:10.1007/s10561-016-9575-4 (2016).

109 Jeong, J.-W. *et al.* Capacitive Epidermal Electronics for Electrically Safe, Long-Term Electrophysiological Measurements. *Advanced Healthcare Materials* **3**, 642-648, doi:https://doi.org/10.1002/adhm.201300334 (2014).

110 Rotenberg, M. Y. & Tian, B. Talking to cells: semiconductor nanomaterials at the cellular interface. *Advanced biosystems* **2**, 1700242 (2018).

111 Tian, B. *et al.* Three-dimensional, flexible nanoscale field-effect transistors as localized bioprobes. *Science* **329**, 830-834 (2010).

112 Fu, T.-M., Hong, G., Viveros, R. D., Zhou, T. & Lieber, C. M. Highly scalable multichannel mesh electronics for stable chronic brain electrophysiology. *Proceedings of the National Academy of Sciences* **114**, E10046-E10055 (2017).

113 Zhou, T. *et al.* Syringe-injectable mesh electronics integrate seamlessly with minimal chronic immune response in the brain. *Proceedings of the National Academy of Sciences* **114**, 5894-5899 (2017).

114 Cohen-Karni, T., Timko, B. P., Weiss, L. E. & Lieber, C. M. Flexible electrical recording from cells using nanowire transistor arrays. *Proceedings of the National Academy of Sciences* **106**, 7309-7313 (2009).

115 Kléber, A. G. & Rudy, Y. Basic mechanisms of cardiac impulse propagation and associated arrhythmias. *Physiological reviews* (2004).

116 Kim, S. J. *et al.* Multifunctional cell-culture platform for aligned cell sheet monitoring, transfer printing, and therapy. *ACS nano* **9**, 2677-2688 (2015).

117 Feiner, R., Fleischer, S., Shapira, A., Kalish, O. & Dvir, T. Multifunctional degradable electronic scaffolds for cardiac tissue engineering. *Journal of Controlled Release* **281**, 189-195 (2018).

118 Feiner, R. *et al.* Engineered hybrid cardiac patches with multifunctional electronics for online monitoring and regulation of tissue function. *Nature materials* **15**, 679-685 (2016).

119 Timko, B. P. *et al.* Electrical recording from hearts with flexible nanowire device arrays. *Nano letters* **9**, 914-918 (2009).

120 Duan, X. *et al.* Intracellular recordings of action potentials by an extracellular nanoscale field-effect transistor. *Nature nanotechnology* **7**, 174-179 (2012).

121 Ingebrandt, S., Yeung, C., Staab, W., Zetterer, T. & Offenhäusser, A. Backside contacted field effect transistor array for extracellular signal recording. *Biosensors and bioelectronics* **18**, 429-435 (2003).

122 Dai, X., Zhou, W., Gao, T., Liu, J. & Lieber, C. M. Three-dimensional mapping and regulation of action potential propagation in nanoelectronics-innervated tissues. *Nature nanotechnology* **11**, 776-782 (2016).

123 Bonk, S. M. *et al.* Design and characterization of a sensorized microfluidic cell-culture system with electro-thermal micro-pumps and sensors for cell adhesion, oxygen, and pH on a glass chip. *Biosensors* **5**, 513-536 (2015).

124 Lee, S.-M. *et al.* Real-time monitoring of 3D cell culture using a 3D capacitance biosensor. *Biosensors and Bioelectronics* **77**, 56-61 (2016).

125 Simon, K. A. *et al.* Polymer-based mesh as supports for multi-layered 3D cell culture and assays. *Biomaterials* **35**, 259-268 (2014).

126 Derda, R. *et al.* supported 3D cell culture for tissue-based bioassays. *Proceedings of the National Academy of Sciences* **106**, 18457-18462 (2009).

127 Lee, M. K., Rich, M. H., Baek, K., Lee, J. & Kong, H. Bioinspired tuning of hydrogel permeability-rigidity dependency for 3D cell culture. *Scientific reports* **5**, 1-7 (2015).

128 Lee, W. & Park, J. The design of a heterocellular 3D architecture and its application to monitoring the behavior of cancer cells in response to the spatial distribution of endothelial cells. *Advanced materials* **24**, 5339-5344 (2012).

129 Chiew, G. G. Y., Wei, N., Sultania, S., Lim, S. & Luo, K. Q. Bioengineered three-dimensional co-culture of cancer cells and endothelial cells: A model system for dual analysis of tumor growth and angiogenesis. *Biotechnology and bioengineering* **114**, 1865-1877 (2017).

130 Swaminathan, S., Ngo, O., Basehore, S. & Clyne, A. M. Vascular endothelial–breast epithelial cell coculture model created from 3D cell structures. *ACS Biomaterials Science & Engineering* **3**, 2999-3006 (2017).

131 Szot, C. S., Buchanan, C. F., Freeman, J. W. & Rylander, M. N. In vitro angiogenesis induced by tumor-endothelial cell co-culture in bilayered, collagen I hydrogel bioengineered tumors. *Tissue Engineering Part C: Methods* **19**, 864-874 (2013).

132 Patra, B. *et al.* Migration and vascular lumen formation of endothelial cells in cancer cell spheroids of various sizes. *Biomicrofluidics* **8**, 052109 (2014).

133 Pradhan, R., Rajput, S., Mandal, M., Mitra, A. & Das, S. Electric cell–substrate impedance sensing technique to monitor cellular behaviours of cancer cells. *RSC Advances* **4**, 9432-9438 (2014).

134 Hong, J., Kandasamy, K., Marimuthu, M., Choi, C. S. & Kim, S. Electrical cell-substrate impedance sensing as a non-invasive tool for cancer cell study. *Analyst* **136**, 237-245 (2011).

135 Szulcek, R., Bogaard, H. J. & van Nieuw Amerongen, G. P. Electric cell-substrate impedance sensing for the quantification of endothelial proliferation, barrier function, and motility. *Journal of visualized experiments: JoVE* (2014).

136 Kloß, D. *et al.* Microcavity array (MCA)-based biosensor chip for functional drug screening of 3D tissue models. *Biosensors and Bioelectronics* **23**, 1473-1480 (2008).

137 Eker, B., Meissner, R., Bertsch, A., Mehta, K. & Renaud, P. Label-free recognition of drug resistance via impedimetric screening of breast cancer cells. *PLoS One* **8**, e57423 (2013).

138 Wang, L., Wu, Y., Hu, T., Guo, B. & Ma, P. X. Electrospun conductive nanofibrous scaffolds for engineering cardiac tissue and 3D bioactuators. *Acta biomaterialia* **59**, 68-81 (2017).

139 O'brien, F. J. Biomaterials & scaffolds for tissue engineering. *Materials today* **14**, 88-95 (2011).

140 Lo, C.-M. *et al.* Monitoring of ovarian cancer cell invasion in real time with frequency-dependent impedance measurement. *American Journal of Physiology-Cell Physiology* **311**, C1040-C1047 (2016).

141 Zhu, P., Ning, Y., Yao, L., Chen, M. & Xu, C. The proliferation, apoptosis, invasion of endothelial-like epithelial ovarian cancer cells induced by hypoxia. *Journal of Experimental & Clinical Cancer Research* **29**, 1-8 (2010).

142 Walter-Yohrling, J., Pratt, B. M., Ledbetter, S. & Teicher, B. A. Myofibroblasts enable invasion of endothelial cells into three-dimensional tumor cell clusters: a novel in vitro tumor model. *Cancer chemotherapy and pharmacology* **52**, 263-269 (2003).

143 Hwang, S.-W. *et al.* A physically transient form of silicon electronics. *Science* **337**, 1640-1644 (2012).

144 Hwang, S.-W. *et al.* Biodegradable elastomers and silicon nanomembranes/nanoribbons for stretchable, transient electronics, and biosensors. *Nano letters* **15**, 2801-2808 (2015).

145 Hwang, S. W. *et al.* Materials and fabrication processes for transient and bioresorbable high-performance electronics. *Advanced Functional Materials* **23**, 4087-4093 (2013).

146 Kang, S.-K. *et al.* Bioresorbable silicon electronic sensors for the brain. *Nature* **530**, 71-76 (2016).

147 Xu, L. *et al.* Materials and fractal designs for 3D multifunctional integumentary membranes with capabilities in cardiac electrotherapy. *Advanced materials* **27**, 1731-1737 (2015).

148 Kim, D. H. & Rogers, J. A. Stretchable electronics: materials strategies and devices. *Advanced materials* **20**, 4887-4892 (2008).

149 Yang, Y. & Gao, W. Wearable and flexible electronics for continuous molecular monitoring. *Chemical Society Reviews* **48**, 1465-1491 (2019).